2020

Passive Scene Reconstruction in Non-line-of-sight Scenarios

Andre Beckus
University of Central Florida

PASSIVE SCENE RECONSTRUCTION IN NON-LINE-OF-SIGHT SCENARIOS

by

ANDRÉ BECKUS
B.S. in Computer Science, University of Central Florida, 2003
B.S. in Electrical Engineering, University of Central Florida, 2015
M.S. in Electrical Engineering, University of Central Florida, 2018

A dissertation submitted in partial fulfilment of the requirements
for the degree of Doctor of Philosophy
in the Department of Electrical and Computer Engineering
in the College of Engineering and Computer Science
at the University of Central Florida
Orlando, Florida

Summer Term
2020

Major Professor: George K. Atia

ABSTRACT

Locating and identifying hidden objects can prove critical in applications ranging from military reconnaissance to emergency rescue. Although non-line-of-sight (NLOS) reconstruction and imaging have received much attention recently, state-of-the-art methods often use coherent sources (lasers) or require control of the scene. This dissertation focuses on *passive* NLOS scene reconstruction using the light reflected off a diffusive wall. No control over the light illuminating the scene is assumed, and the method is compatible with the partially coherent fields ubiquitous in both indoor and outdoor environments. In order to counteract the detrimental effects of the wall, rather than measuring the 2-dimensional *intensity* of the reflected light, we exploit the full 4-dimensional *spatial coherence* function to reconstruct the scene. As a step towards the NLOS problem, we first consider the *line-of-sight* (LOS) problem. Numerical simulations using Fresnel propagation operators show that our forward model has good agreement with experimental results. We show that numerically back-propagating the measured coherence function enables a visual estimation of the objects' sizes and locations. To facilitate efficient, systematic and explicit detection of object parameters in the inverse problem, we propose a closed-form approximation of the propagated coherence function. Using this analytic solution we formulate a minimum residue optimization problem which is solved using a gradient descent algorithm. Then, for the NLOS problem, we derive an analytic model based on experimentally-verified scattering models. This model is used to study the information retained in the coherence function after the field interacts with the wall, and this insight is used to classify and estimate simple objects. Finally, we consider imaging in more complicated settings with larger objects. We formulate a multi-criteria convex optimization problem, which fuses the reflected field's intensity and spatial coherence information at different scales, along with an algorithm to efficiently solve the proposed problem.

Dedicated to my mother, father, and sister – my first teachers

ACKNOWLEDGMENTS

I would like to thank my advisor, Dr. George Atia, for his guidance and support. He provided the perfect balance of motivation, knowledge, critique, patience, and kindness.

I would like to thank the professors with whom I worked on UCF's DARPA REVEAL team, who provided countless hours of support, and without whom this dissertation would not be possible. These include: Dr. Alexandru Tamasan, Dr. Aristide Dogariu, and Dr. Ayman Abouraddy. Many thanks also go to the students, postdocs, and research scientists who I collaborated with on the project, and with whom I shared many happy and tiring times. Thank you to my lab-mates in the Digital Signal Processing lab for interesting discussions and sharing this experience with me. I am indebted to Davood Mardani for providing invaluable advice regarding efficient numerical calculation of the Fresnel operator. I am grateful also to Dr. Abhijit Mahalanobis and Dr. Wasfy Mikhael for agreeing to serve on my committee.

Thank you to my friends and family for their support and patience. They continued to check in with me, even when I became too focused on my work to reciprocate. Thank you to the many teachers and professors who selflessly helped me throughout my life to build the foundation on which this PhD rests. And thank you to my past coworkers who showed me how to get things done.

This work would not have been possible without the support of the Defense Advanced Research Projects Agency (DARPA), Defense Science Office under contract HR0011-16-C-0029, and the National Science Foundation CAREER Award under Grant CCF-1552497.

TABLE OF CONTENTS

LIST OF FIGURES

LIST OF TABLES

CHAPTER 1: INTRODUCTION

Identifying an object from indirect light can provide critical information in many practical applications, e.g., in defense, collision avoidance, or emergency situations. Here we assume partially coherent sources (e.g., fluorescent or LED light, as well as sunlight), which are outside the control of the observer. We refer to this problem as *Passive* NLOS imaging[1].

A motivating example for the passive NLOS problem is illustrated in Fig. 1.1: An object is hidden from view by the obstructing Wall 1, and a complex camera measures light reflected from Wall 2. There may also be a shadow (i.e., spatial variation in intensity pattern) on the wall, whose edge resolution decreases with the decrease of the field's spatial coherence; contrast the highly coherent case in Fig. 1.1(b) with the lower coherent case in Fig. 1.1(c). In addition, a second source floods the wall with light; see Fig. 1.1(d). While a lensed camera may still be able to image the shadow, the image quality will be degraded due to noise and quantization error. Depending on the scene and wall configuration, the shadow may be all but useless in detecting the hidden object, thus requiring an alternative modality for scene reconstruction.

[1]In this chapter, we partially use the material published in the Journal of the Optical Society of America A (JOSA A), 2017 [9], Optics Express, 2017 [2], Optics Letters, 2017 [1], Frontiers in Optics, 2017 [11], and IEEE Transactions on Image Processing, 2019 [6].

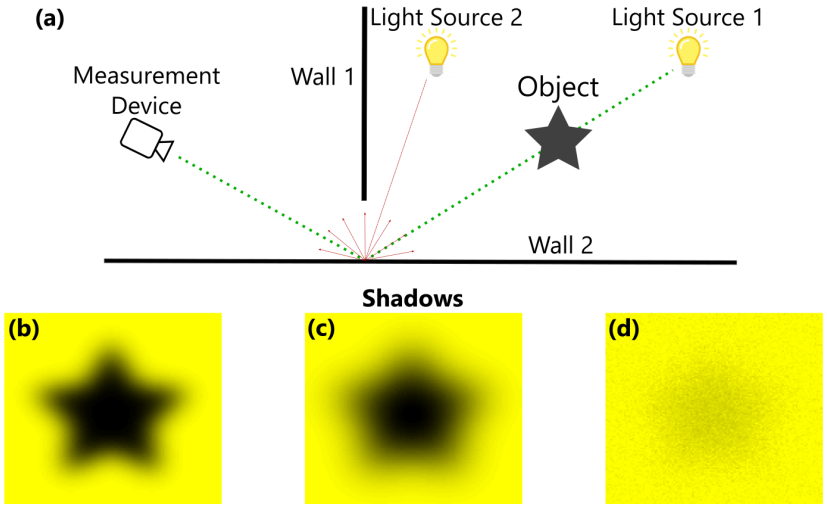

Figure 1.1: (a) Scenario considered in this paper. Bottom of figure shows examples of shadows in scenarios ranging from ideal on left to non-ideal on right. (b) Distinct shadow cast with highly coherent light. (c) Indistinct shadow due to less coherent light. (d) Faint and noisy shadow due to Light Source 2 being turned on. This shadow is generated by adding uniform ambient light and Gaussian noise to (b), and the pixels are then quantized to 16 bits.

Before delving into the specifics of our approach, we review existing NLOS techniques, both active and passive.

1.1 Non-line-of-sight Reconstruction

Although the study of NLOS problems has seen a large amount of activity recently, many state-of-the-art methods require active control of the illumination or scene. One common approach entails the use of controllable coherent sources (lasers). For example, the object may be directly illuminated by a laser [17, 18], or a temporally coherent light source [19, 20]. Other methods allow the scene to be illuminated remotely by bouncing laser pulses off the wall and then isolating the bal-

listic photons (direct carriers of information about the object) from the diffusely scattered photons which have lost the history of their interaction with the object. This is typically accomplished by capturing time-of-flight of the photons [21–25]. One exception is the laser-based method of [26], which relies solely on intensity images of the reflected laser light, albeit this method also requires movement of the object. Still, other methods that do not constrain the light source require that the scene be modified in some way, for example by requiring that a reference object [27] or point source [28] be used.

Existing approaches to the passive imaging problem have relied mostly on intensity-only measurements. In the absence of significant shadows, intensity measurements alone are insufficient for scene reconstruction, and so these methods must place additional constraints on the scene. The "accidental" pinhole camera [29] allows imaging, but requires that the obstructions take a very specific form such that a pinhole is present. The "corner" camera [30] exploits the edges of the obstructions themselves. However, this method only produces 1D (if one edge is present) or 2D (when two edges are present, e.g., with a doorway) positions of moving objects.

1.2 Spatial Coherence

As described in the previous section, NLOS approaches often constrain the scene or impose priors on the reconstruction. Alternatively, they expand the measurements to include an extra dimension (time) by requiring motion of the object. We consider here an alternative for increasing the dimensionality of the measurements: instead of measuring the 2D *intensity* profile, we use the 4D *spatial coherence function* (which subsumes the intensity profile).

The spatial coherence G of a quasi-monochromatic scalar field U at two points $\mathbf{r}_1, \mathbf{r}_2$ is defined as

an ensemble average over random field realizations

$$G(\mathbf{r}_1, \mathbf{r}_2) = \langle U(\mathbf{r}_1) U^*(\mathbf{r}_2) \rangle, \tag{1.1}$$

where $*$ denotes the complex conjugation, and $\langle \cdot \rangle$ is an ensemble average over field realizations (see [31]).

Spatial coherence has been used for the related problem of tomography in scattering media [32, 33]. A similar modality is that of phase-space measurements, which characterize the signal in both space and frequency domains [34]. These measurements have a close relation to the spatial coherence measurements used here [35]. These measurements have been used, for example, to determine the three-dimensional location of point sources embedded in volumetrically scattering biological samples [36].

The problem of detecting an object using spatial coherence measurements is characterized fundamentally by two spatial scales: the transverse extent of the scattered-field *intensity distribution* and the width of the *spatial coherence function* associated with the field. In a lensless configuration, diffractive spreading can render the extent of the former quite large and devoid of distinctive features. The width of the spatial coherence function, however, may be considerably smaller and retain sufficient information to identify a scattering object. Furthermore, even though the field is spread spatially over a large area, we need to sample only a limited spatial extent of the scattered field – on the order of the transverse coherence length of the field at the detection plane. Surprisingly, the spatial extent of the required measurement in some situations may be *smaller* than the physical size of the object itself, which could be located a large distance away from the detection plane.

Because the spatial extent of the intensity profile is much larger than the typical coherence width,

it is advantageous to work with "rotated" coordinates. Specifically, we work with the following coordinates: the midpoint $\mathbf{r} = (\mathbf{r}_1 + \mathbf{r}_2)/2$, and displacement $\boldsymbol{\rho} = \mathbf{r}_1 - \mathbf{r}_2$, yielding

$$G(\mathbf{r}, \boldsymbol{\rho}) = \langle U(\mathbf{r} + \boldsymbol{\rho}/2) U^*(\mathbf{r} - \boldsymbol{\rho}/2) \rangle. \tag{1.2}$$

We refer to $\mathbf{r}$ and $\boldsymbol{\rho}$ hereon as the *intensity* and *coherence* coordinates, respectively. The standard and transformed coordinates are illustrated in Fig. 1.2.

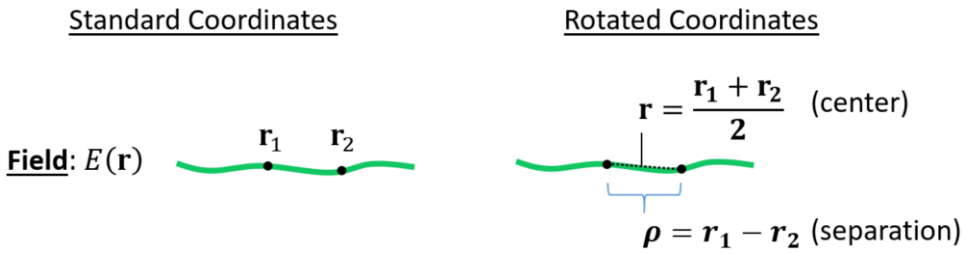

Figure 1.2: Diagram showing the standard and transformed coordinates used for the spatial coherence function.

The 2D intensity of the field I is subsumed by the 4D coherence function along one plane $I(\mathbf{r}) = G(\mathbf{r}, \mathbf{0})$. In this sense, the coherence function provides a complete description of a partially coherent field, whereas the intensity alone does not.

In Chapters 2 and 3, we consider 1D scenes in which the electric field depends only on one transverse spatial coordinate, i.e., we transform $U(\mathbf{r}) \rightarrow U(x)$. Therefore, the coherence function depends only on two transverse spatial coordinates x_1, x_2. In this case, the function $G(\mathbf{r}_1, \mathbf{r}_2)$ in (1.1) becomes

$$G(x_1, x_2) = \langle U(x_1) U^*(x_2) \rangle, \tag{1.3}$$

and we denote the rotated coordinates

$$y_1 = \frac{x_1 + x_2}{2}, \qquad y_2 = \frac{x_1 - x_2}{2}. \tag{1.4}$$

Then, the rotated coherence function of (1.2) becomes

$$G(y_1, y_2) = \langle U(x_1 + x_2)U^*(x_1 - x_2)\rangle. \tag{1.5}$$

Note that the scaling of the displacement found in y_2 is different from that found in $\boldsymbol{\rho}$ by a factor of two.

In the experiments, the degree of spatial coherence $g(\mathbf{r}, \boldsymbol{\rho})$ (also known as the spectral degree of coherence) is often used. The function $g(\mathbf{r}, \boldsymbol{\rho})$ is related to $G(\mathbf{r}, \boldsymbol{\rho})$ through a normalization with respect to the intensity,

$$g(\mathbf{r}, \boldsymbol{\rho}) = G(\mathbf{r}, \boldsymbol{\rho}) / \sqrt{I(\mathbf{r} + \frac{\boldsymbol{\rho}}{2}) I(\mathbf{r} - \frac{\boldsymbol{\rho}}{2})}. \tag{1.6}$$

For the 1D scene, the degree of spatial coherence associated with the function $G(y_1, y_2)$ defined in (1.2) is

$$g(y_1, y_2) = G(y_1, y_2) / \sqrt{I(y_1 + y_2) I(y_1 - y_2)}. \tag{1.7}$$

1.2.1 Measurements

The spatial coherence function can be obtained by various measurement strategies, e.g., through the use of double slits [2, 37–40], non-redundant arrays of apertures [41, 42], lateral-shearing Sagnac and reversed-wavefront Young interferometers [43–45], microlens arrays [46], and phase-space

methods [47–49].

In this work, we use measurements obtained from two different experimental devices. The first device is a wavefront shearing interferometer named the Dual-Phase Sagnac Interferometer (DuPSaI) [1]. The configuration of this measurement device is shown in Fig. 1.3.

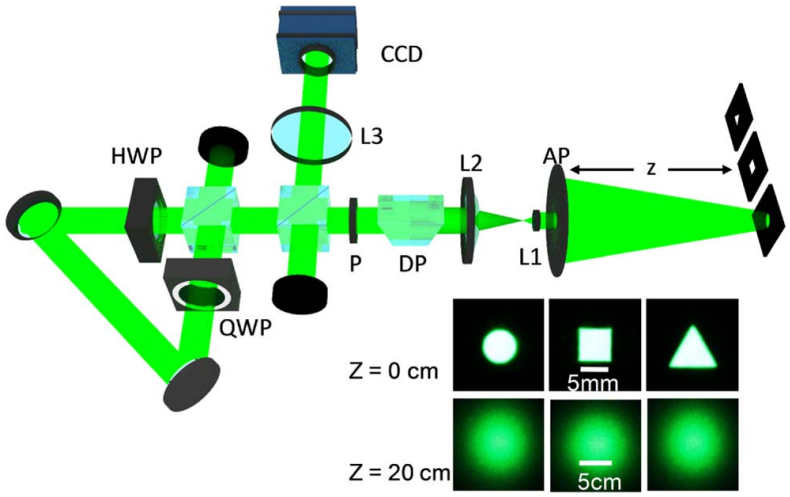

Figure 1.3: Schematic of the DuPSaI for measuring the SCF at the plane of the input AP. The inset shows the intensity distributions of differently shaped sources recorded in the source plane (top row) and at 20 cm distance (bottom row). (Figure from [1], p. 4930).

The second device makes use of dynamic double slits produced by a digital micromirror device (DMD) [2], as shown in Fig. 1.4.

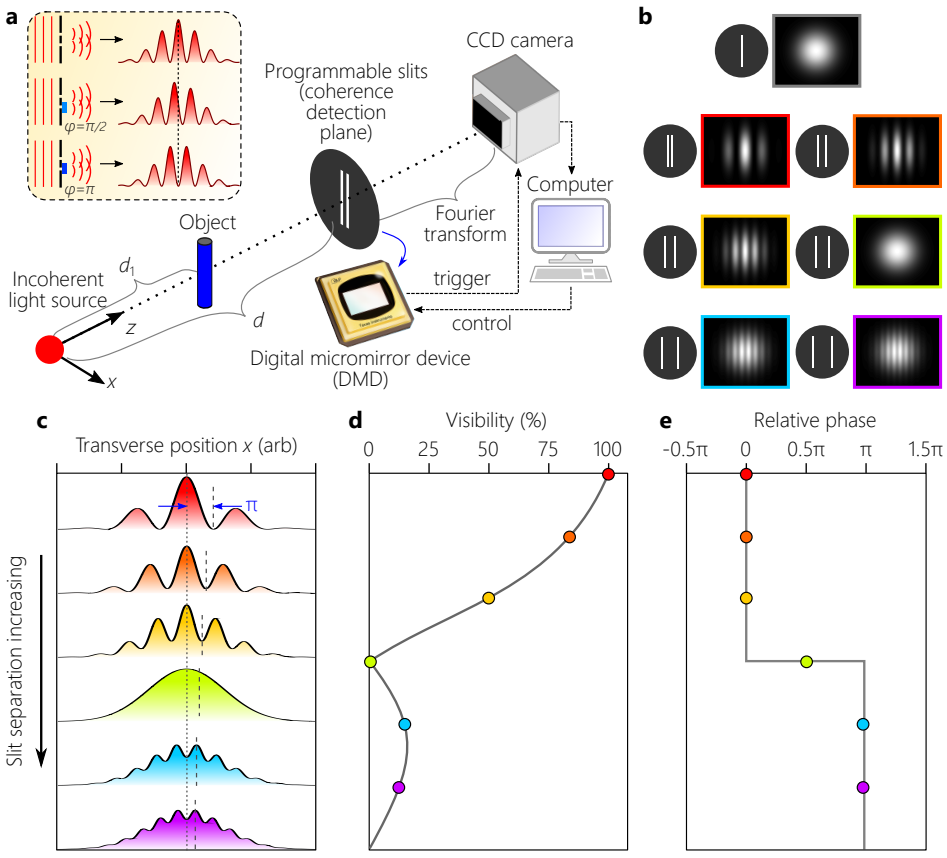

Figure 1.4: Complex-coherence measurements of incoherent light scattered from an object. (Figure from [2], p. 13091).

We will refer to this measurement setup as the double-slit DMD device. More details regarding signal processing in this device are provided in Appendix D.

1.3 Organization of the Dissertation and Summary of Contributions

We break our study into two main parts, both of which are critical to solving the full scene reconstruction problem. In the first part, we consider the problem of propagation to the wall, i.e., free

space propagation, and study the LOS inverse problem. Because the spatial coherence function is unscattered, it provides a complete description of the scene, making our study applicable to computational imaging problems as well [50]. In the second part, we examine the scattering effects of the wall on the propagated spatial coherence function, determine what useful information is retained in the "damaged" coherence function, and formulate an approach to extract this information.

Our approach is physics-driven in the sense that we use established physics-based models from the theory of light propagation and scattering [1, 2, 51]. Therefore, we further break each part of the study into two chapters: one chapter addresses the forward problem, including a detailed analysis of the physical models; the other chapter addresses the inverse problem. The organization of the chapters is shown in Fig. 1.5.

	Forward Problem	**Inverse Problem**
Part 1: Free space Propagation	Chapter 2	Chapter 3
Part 2: Wall Scattering	Chapter 4	Chapter 5
Future Directions	Chapter 6	

Figure 1.5: Dissertation organization

The contributions of each chapter are summarized below.

1. In Chapter 2, we first study a model for free space propagation of spatial coherence. Numerical calculations of the propagation operator are shown to match both 1D and 2D experimental measurements. These results show that the spatial coherence function at a distant detector retains artifacts from interaction with an object, thus suggesting feasibility of the inverse problem. In order to facilitate solution of the inverse problem, closed-form analytic solutions are derived for the spatial coherence propagation after interaction with an object.

2. In Chapter 3, we study the inverse problem for free space propagation. We consider two techniques for inverting the free space propagation. The first is a "brute-force" approach for recreating the evolution of the intensity profile using the inverse Fresnel transform. The second is a more efficient and systematic minimum residue optimization method using the closed-form approximations derived in Chapter 2.

3. In Chapter 4, we study the forward model for wall scattering using an experiment-based wall model. We examine what information is preserved after interaction with the wall in the spatial coherence function.

4. In Chapter 5, we first derive a method for characterizing shapes, and for determining the distance to a small, simple object. We then consider the problem of imaging larger objects. We also consider the case where the shadow on the wall does provide useful information, and provide a multi-modal fusion formulation for solving the inverse problem.

5. In Chapter 6, we consider future directions. This includes a discussion of the Wigner function and its advantages in computational imaging, and a consideration of deep learning techniques which may be applied to our scene reconstruction problem.

1.4 Notation

Vectors and matrices are denoted using bold-face lower-case and upper-case letters, respectively. Given a vector $\mathbf{a}$, its ℓ_p-norm is denoted by $\| \mathbf{a} \|_p$ and $a(i)$ is the i^{th} element. The diagonalization operator $\mathrm{Diag}(\mathbf{a})$ returns a matrix with the elements of $\mathbf{a}$ along the diagonal. The vectorization of an $M \times N$ matrix $\mathbf{A}$ is denoted $\mathrm{vec}\,\{\mathbf{A}\}$, with the result taking the form of an MN element vector. The unit vector with a one in the i^{th} entry is denoted $\mathbf{e}_i$. Matrices or vectors containing all ones or all zeros are denoted $\mathbf{1}$ and $\mathbf{0}$, respectively, where the dimensions will be clear from the context.

The Hadamard product $\odot$ returns the element-wise product of its arguments. A weighted norm is defined as $\|\mathbf{a}\|_{\mathbf{v}}^2 = \mathbf{a}^*(\mathrm{Diag}\,\mathbf{v})\mathbf{a}$.

The 2D Fourier transform of a function $f(x, y)$ is denoted $\mathcal{F}\{f(x, y)\}(\omega_x, \omega_y)$, where ω_x and ω_y are angular frequencies. The 2D Discrete Fourier Transform (DFT) of matrix $\mathbf{A}$ is expressed as $\mathbf{F}_1\mathbf{A}\mathbf{F}_2$, where $\mathbf{F}_1$ and $\mathbf{F}_2$ are the 1D DFTs along the columns and rows of $\mathbf{A}$, respectively. The notation $\star$ is used to indicate both the continuous and discrete forms of the two-dimensional convolution operator.

Let $\mathbb{R}\mathrm{e}[.]$ and $\mathbb{I}\mathrm{m}[.]$ denote the real and imaginary components of their complex argument, respectively.

CHAPTER 2: FORWARD PROBLEM FOR FREE SPACE PROPAGATION

2.1 Introduction

When incoherent or partially coherent light scatters off an obstructive object, the shadow formed in the vicinity of the object gradually blurs at larger distances until the scattered field ultimately exhibits a smooth distribution with only feeble local intensity variations[1]. An experimental demonstration is shown in Fig. 2.1 from [1].

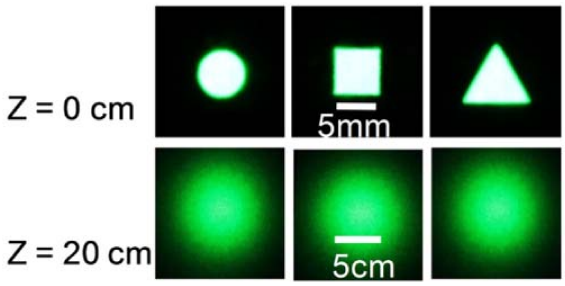

Figure 2.1: Zoomed inset from figure in [1], p. 735.

However, despite this blurring of the intensity function, the electric field still retains information about the object. In line-of-sight (LOS) applications, a lens may be used to "extract" this information to form an image of the object. However, in anticipation of the full NLOS problem, we assume here that a lens cannot be used; the wall destroys the information sufficiently that a lens cannot reconstruct the scene.

[1]In this chapter, we partially use the material published in the Journal of the Optical Society of America A (JOSA A), 2017 [9], Optics Express, 2017 [2], Optics Letters, 2017 [1], and Frontiers in Optics, 2017 [11].

In absence of a lens to form an image, it is difficult to reconstruct the scattering object from a measurement of the far-field intensity alone. Although image processing can help improve the quality of a recorded image by removing blur resulting from motion or poor focusing [52–54], it remains a notoriously difficult task to undo the blurring from diffractive spreading after free propagation. Although the transfer function for free propagation of incoherent light does *not* include zeros (for an infinitely sized detector), the decay of the transfer function with spatial frequency is nevertheless extremely sharp [55], which makes the inversion sensitive to noise. In other words, the remnant spatial variations in the lensless far-field intensity distribution are too small to allow for object reconstruction. Other approaches to reconstruct a scattering object make use of phase retrieval [56] with the measured intensity distributions in two planes [57], or the amplitude [58] or phase [59, 60] of the Fourier transform of the field – with the phase information typically yielding better reconstructions [61–63]. These approaches are usually more successful in object reconstruction when coherent light is used [64–67].

At the same time, it is well known that the spatial coherence function is an excellent encoder of information (such as location, spatial extent, etc.) about the source [68]: for the simple cases involving apertures we refer to Section 5.7 of [69], and for the quasi-homogeneous partially coherent sources to [70]. Here, we demonstrate that the spatial coherence function retains significant information regarding the field's interaction with more complex source configurations as well.

In this chapter, we first present a propagation model to describe the free space evolution of the spatial coherence conference. This model serves as the basis for the remainder of our work. We then present results using straight-forward numerical evaluation of the forward propagation operator, showing that the model has close agreement with experimental results for both 1D and 2D scenes.

We next turn to a more systematic study of the propagation operator. One aim for this study is towards improved computational efficiency. Anywhere but in very special cases, the free evolution

of coherence functions cannot be obtained analytically in closed form. Even if such a solution is found, once the field scatters off an object, further field evolution can only be evaluated numerically. For example, the generic Gauss-Schell model for a partially coherent field approximates the characteristics of the radiation produced by a wide range of optical sources. Furthermore, such a model admits a tractable analytical treatment of its free evolution [71, 72], or even for long-range propagation through turbid media as long as no size restrictions are involved [73, 74]. However, once the intensity profile is modified by passage through a finite aperture (see Section 5.7 of [69]), transmittance through a partially transparent medium, or scattering off an object, the subsequent evolution of the coherence function no longer resembles the initial Gauss-Schell model. Instead, calculation of the propagated coherence function is accomplished using a double diffraction integral [68], which incurs a high computational cost. We call the field produced by such a secondary source, the original coherence function modulated with an arbitrary amplitude profile, a 'generalized source'.

There exist techniques that can help reduce the computational complexity, such as accelerating the calculation of the Fresnel integrals through the use of the Fast Fourier Transform [75], avoiding full computation of the Fresnel integrals [76], or exploiting the coherent communication modes of the propagation kernel itself in which the field is expanded [77]. Another strategy involves carrying out a singular expansion of the source in terms of coherent modes to take advantage of the simpler coherent propagation integrals [76, 78], but the calculation of the modes is beam-specific [72,79–82] and the number of required modes increases with reduced field coherence [82]. An altogether different numerical strategy makes use of ray-tracing [83], which can outperform Fresnel integration by limiting the number of rays [84].

As an alternative, we obtained a closed-form expression for the spatial coherence function of partially coherent fields propagating from generalized sources in the Fresnel regime, which reduces the computational complexity and affords a favorable ground for the study of inverse problems.

We focus on a one-dimensional model in which the field is assumed to vary only along one transverse direction by a piecewise constant transmission function, but the concepts developed herein are naturally extendable to higher dimensions. Our closed-form solution characterizes the coherence from generalized sources in terms of a *conjugated Hilbert transform* [85,86], a modified form of the Hilbert transform in which a function is first modulated by a linear phase, transformed, and then modulated by a conjugated phase. Some mild restrictions must be satisfied for this approach to succeed; e.g., the transverse coherence width must be at least one order of magnitude larger than the wavelength, but narrower than features of the transmission function of the generalized source.

A distinguishing feature of our approach is that the parameters of the source appear explicitly in the closed-form expression of the generalized source. For this reason, the results presented herein set the stage for the inverse problem in which reconstruction of a generalized source is intended from coherence measurements.

2.2 Source Models

2.2.1 General Quasi-homogeneous Sources

For all light source models used in this work, we assume monochromatic radiation emitted by a Gaussian-correlated light source. Furthermore, we assume the quasi-homogeneous approximation with the spatial coherence function of the form

$$G_s\left(\mathbf{r},\boldsymbol{\rho}\right) = I_{\mathrm{in}}(\mathbf{r}) \exp\left(-\frac{\rho_x^2}{2\sigma^2}\right) \exp\left(-\frac{\rho_y^2}{2\sigma^2}\right), \tag{2.1}$$

where σ is termed the coherence width. In this approximation, the function is separable with regard to the "intensity" and "coherence" components [32,87]. where the intensity distribution $I(\mathbf{r})$

describes the corresponding shape of the mask, and σ is the standard deviation of the Gaussian-correlated source.

2.2.2 Gauss-Schell Model Sources

Underlying many of the results in Chapters 2 and 3 is a generic partially coherent field described by a Gauss-Schell model [87]. Our results herein fall in the regime wherein the beam width of the source is assumed to be much larger than the coherence width, thus warranting the quasi-homogeneous approximation and yielding a coherence function $G(y_1', y_2') = I(y_1')g(y_2')$; where I and g are separable intensity and coherence functions, respectively [32, 87]. Let $N^{\beta}(x) = \exp\{-x^2/2\beta^2\}$ denote the Gaussian of standard deviation β. Then, the coherence function of the Gauss-Schell model source (located at $z=0$) is

$$G^{-}(y_1', y_2') = A_{\mathrm{o}}\, N^{w_{\mathrm{o}}}(y_1')\, N^{\sigma_{\mathrm{o}}}(y_2'), \tag{2.2}$$

where A_{o} is an amplitude, w_{o} the width of the intensity profile, and σ_{o} the coherence width of this initial field (all denoted with the subscript 'o').

2.2.3 Generalized Source Model

We consider a Gauss-Schell beam (2.13) modulated by a piecewise constant complex transmission function, referred to as a *generalized source*. The source G^{-} is masked by a piecewise constant transmission function $t(x) \in \mathbb{C}$, $|t(x)| \leq 1$. Hence, the coherence function of the generalized source is

$$G(y_1', y_2') = G^{-}(y_1', y_2')\, t(y_1' + y_2')\, t^{*}(y_1' - y_2'). \tag{2.3}$$

An example of such a source is shown in Fig. 2.2(b) and (c) in both unrotated and rotated coordinates.

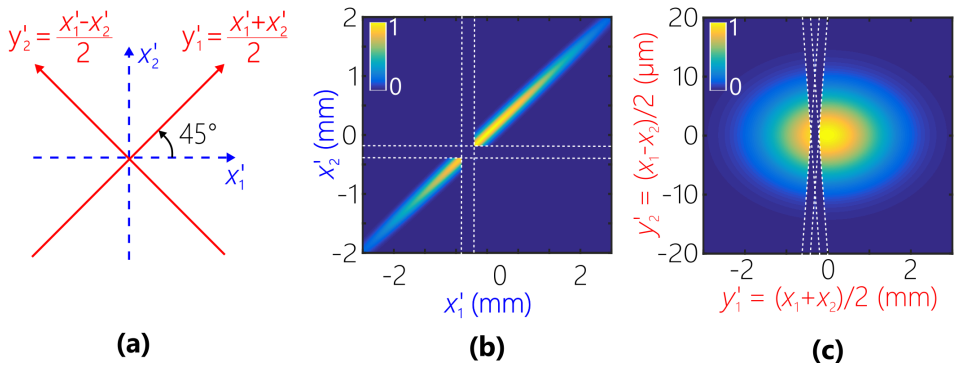

Figure 2.2: (a) Illustration of rotated coordinates. An example of a generalized source is shown in (b) unrotated coordinates and (c) rotated coordinates. For this example, the Gauss-Schell source parameters are $A = 1$, $w = 1$ mm, $\sigma = 50$ μm. The transmission function is such that $t(x)$=0 for $x \in [a_1, a_2)$, and $t(x)$=1 otherwise, where $a_1 = -0.4$ mm and $a_2 = -0.2$ mm. Dotted white lines indicate the regions affected by the transmission function.

2.3 Free Space Fresnel Propagation

We will use the propagation model shown in Fig. 2.3, which is illustrated for the special case where there is a single object.

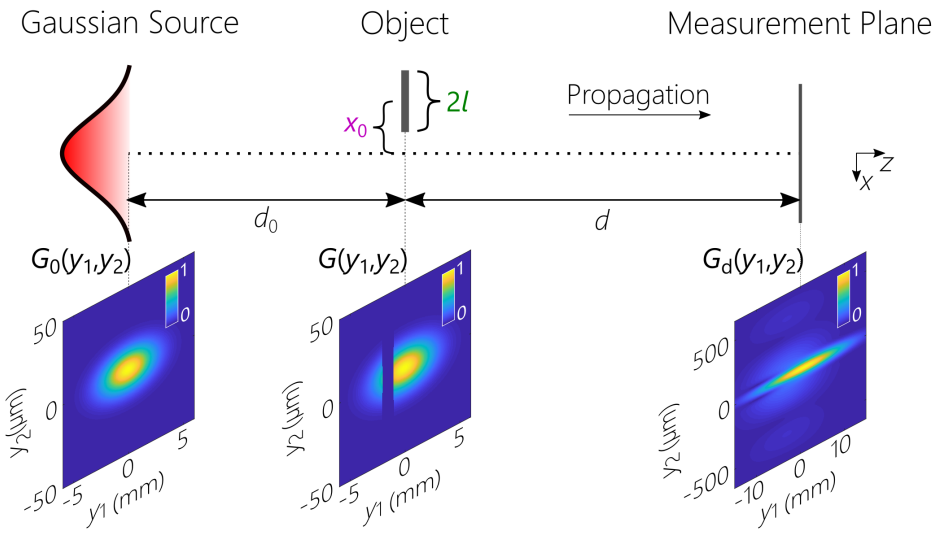

Figure 2.3: A single object scene with $x_0 = -1.5$ mm, $l = 0.5$ mm, $d_0 = 10$ cm, and $d = 100$ cm. The normalized magnitude of the coherence function is shown at the bottom of the diagram in three planes: in the plane of the Gaussian source, immediately after interacting with the object (i.e. at the secondary source), and at the measurement plane.

Given a planar source located at $z = 0$ with coherence function $G(x_1', x_2')$, after propagating a distance d in the Fresnel regime (where the normals to the wave front make small angles with the direction of propagation), the coherence function becomes

$$\iint G(x_1', x_2')\, h(x_1, x_1')\, h^*(x_2, x_2')\; dx_1'\, dx_2', \tag{2.4}$$

where the Fresnel propagator h is given by

$$h(x_1, x_1') = \frac{\exp(ikd)}{\sqrt{i\lambda d}} \exp\left\{ i \frac{k}{2d} (x_1 - x_1')^2 \right\}; \tag{2.5}$$

here λ is the wavelength and k is the wavenumber. The integration is over $\mathbb{R}^2$, i.e. the infinite plane

of the source.

Using the rotated coordinates described in (1.4), the Fresnel model of coherence propagation becomes

$$G_d(y_1, y_2) = \frac{1}{2\pi\ell^2} \iint_{\mathbb{R}^2} G(y_1', y_2')\, \mathcal{L}(y_1, y_1', y_2, y_2')\, dy_1'\, dy_2', \tag{2.6}$$

with $\ell = \sqrt{d/2k}$ and the kernel is

$$\mathcal{L}(y_1, y_1', y_2, y_2') = \exp\left\{ i(y_1 - y_1')(y_2 - y_2')/\ell^2 \right\}. \tag{2.7}$$

For a 2D scene, we have two transverse coordinates along the x, y axes, and the field propagates along the z axis. Suppose a planar source is located at $z = 0$ with coherence function $G(\mathbf{r}, \boldsymbol{\rho})$. The spatial coherence function in a plane at $z = d$ is calculated using the Fresnel integrals [88]

$$\begin{aligned} G_d\left(\mathbf{r}, \boldsymbol{\rho}\right) = & \frac{1}{(\lambda d)^2} \iint \iint \mathrm{d}r_x' \mathrm{d}r_y \mathrm{d}\rho_x' \mathrm{d}\rho_y' \\ & \times H\left(r_x, r_x', \rho_x, \rho_x'; d\right) H\left(r_y, r_y', \rho_y, \rho_y'; d\right) \\ & \times G\left(\mathbf{r}', \boldsymbol{\rho}'\right); \end{aligned} \tag{2.8}$$

where λ is the wavelength, $k = \frac{2\pi}{\lambda}$ is the wavenumber, and $H\left(x, x', \rho, \rho'; d\right) = \exp\left[\frac{ik}{d}\left(x + x'\right)\left(\rho - \rho'\right)\right]$ is the free space Green's function for the electric field.

While we use a single wavelength for simplicity, the propagation of broadband light can also be accomplished by propagating at multiple wavelengths and summing the results. This method would still preserve the linearity of the transforms.

2.4 Experimental Validation of 1D Model

The light source in the first set of experiments is an extended-area LED whose partial coherence is represented by a truncated Gauss-Schell model [89]. Whereas measurements of the coherence function of various unobstructed light sources are well-documented [37, 39, 40, 90], here we focus on the deviations in the measured coherence with respect to that of the source as introduced by an object lying in the field's path. We consider both *intercepting* (obstructing) objects placed in front of a light source to block part of the beam, as well as *reflecting* objects placed such that they reflect light toward the detector. In all cases, we compare the measurements to theoretical predictions obtained using Fresnel propagators.

2.4.1 Experimental Setup

The source is a spatially extended LED (Thorlabs, M625L3) with a peak wavelength of ≈ 633 nm and a FWHM-bandwidth of ≈ 18 nm that is spectrally filtered by a ≈ 1.3-nm-FWHM band-pass filter centered at 632.8 nm (Thorlabs, FL632.8-1). Measurements were collected by the double-slit DMD device [2].

We consider thin planar one-dimensional (1D) objects whether obstructive or reflective – with the other transverse dimension assumed uniform. Such an object is parameterized by three quantities: size, transverse position with respect to the optical axis, and longitudinal position with respect to the detection plane.

When individual pixels of the DMD are activated, they tilt approximately 12.5° away from the normal to the DMD plane, thus attenuating the measured coherence function (see [2] for more details). To compensate for this artifact of the measurement scheme, a premultiplier was introduced to the numerically calculated function $g(x_1 - x_2)$. Assuming a Gaussian spectral profile, this premuliplier

takes the form of an inverted Gaussian of 627-μm-FWHM. We found that reducing this value by 15% to 533 μm offers an excellent match between the theoretical predictions based on the model presented in the previous subsection and all the measurements. This discrepancy is attributed to the deviation of the actual spectral linewidth of the radiation from the presumed Gaussian form.

2.4.2 Numerical Simulations

The object is assumed to be thin and described by a real-valued transmittance function $t(x)$ – although this model readily accommodates a complex-valued transmittance. Both intercepting (obstructing) and reflecting objects are modeled – for simplicity – as indicator functions; that is, light at any point in the object plane either passes unobstructed, or is blocked completely. For an intercepting object, $t(x) = 1 - \mathrm{rect}\left(\frac{x-x_0}{w}\right)$, where x_0 and w are the object center position with respect to the optical axis and its width, respectively, and $\mathrm{rect}(x) = 1$ when $-0.5 \leq x \leq 0.5$ and is zero otherwise. The reflective object is assumed to be specular, and so is modeled as an aperture with transmission function $t(x) = \mathrm{rect}\left(\frac{x-x_0}{w}\right)$. Objects with transmittance of values other than 0 or 1 can also be accommodated within this framework. The object is thus identified by three parameters: its width w; its transverse position x_0; and its axial distance from the detection plane d_2 (for fixed total distance from source to detector d).

The field propagating from the source plane to the detection plane (a total distance of d) undergoes a mapping through a linear system represented by an impulse response function $h(x_1, x')$, where x_1 is a point in the detection plane and x' is a point in the source plane. In our experimental arrangement, this system consists of a succession of three linear sub-systems: (1) free space propagation a distance d_1 from the source plane x' to the object plane $\tilde{x}$; (2) transmission or reflection from an object located at the plane $\tilde{x}$; and (3) free space propagation a distance d_2 from the object plane $\tilde{x}$ to the detection plane x_1. Recall that free propagation a distance d in the Fresnel regime is

described by the impulse response function

$$h_{\mathrm{F}}(x_1, x'; d) = \frac{\exp(ikd)}{\sqrt{i\lambda d}} \exp\left\{ i\frac{k}{2d}(x_1 - x')^2 \right\}, \tag{2.9}$$

where $k = 2\pi/\lambda$ is the wavenumber [91].

The impulse response function $h(x_1, x')$ of the entire system from the source to detector is therefore given by

$$h(x_1, x') = \int d\tilde{x}\, h_{\mathrm{F}}(x_1, \tilde{x}; d_2)\; t(\tilde{x})\; h_{\mathrm{F}}(\tilde{x}, x'; d_1). \tag{2.10}$$

The coherence function at a pair of points x' and x'' in the *source* plane of $G_{\mathrm{s}}(x', x'')$ is mapped to a pair of points x_1 and x_2 in the *detection* plane of $G(x_1, x_2)$ via the transformation

$$G(x_1, x_2) = \iint dx' dx'' h(x_1, x')\; h^*(x_2, x'')\; G_{\mathrm{s}}(x', x''). \tag{2.11}$$

Using this forward model, the coherence at the detector plane can be evaluated once the source is known, which requires a reference measurement. Finally, the calculation results are integrated over the source spectral bandwidth (1 nm in these experiments) [68].

2.4.3 Source Characterization

We first characterize the light source model – in absence of any object – using an experimental reference measurement. To capture the characteristics of the partial coherence of the source, we make use of a Gauss-Schell model [89, 92, 93] in which a jointly Gaussian coherence function (along the x'+x'' and x'–x'' directions) has its intensity profile truncated. The intensity of the source is taken to be Gaussian but is spatially limited by a width equal to the size of the LED (≈ 2 mm). The Gauss-Schell model is parameterized by the beam width α, the spatial coherence width σ,

and aperture width L. The source is quasi-monochromatic modeled with a uniform spectral profile having a center wavelength $\lambda_0 = 633$ nm and bandwidth $\Delta\lambda = 1.3$ nm. Therefore, the full coherence function of the source is given by

$$G_{\mathrm{s}}(x', x''; \lambda) = \exp\left(-\frac{(x'+x'')^2}{2\alpha^2}\right) \exp\left(-\frac{(x'-x'')^2}{2\sigma^2}\right) \mathrm{rect}\left(\frac{x'}{L}\right) \mathrm{rect}\left(\frac{x''}{L}\right) \mathrm{rect}\left(\frac{\lambda-\lambda_0}{\Delta\lambda}\right). \tag{2.12}$$

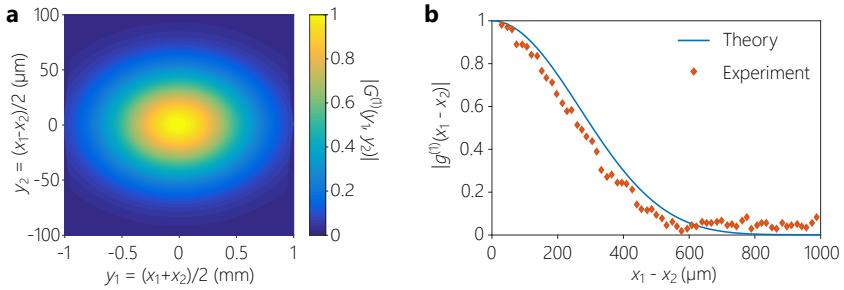

Figure 2.4: (a) The measured magnitude of the degree of spatial coherence $|g(x_1 - x_2)|$ (diamonds) at the detector plane in absence of an object (uninterrupted propagation from the source to the detector). The solid line is a theoretical fit. The measured and theoretical phase $\mathrm{Arg}\{g(x_1, x_2)\}$ is zero over this range [see Fig. 2.5(b)]. (b) A plot of the spatial coherence function magnitude of the source $G_{\mathrm{s}}(x', x'')$ based on Eq. 2.12 that makes use of the parameters extracted from the measurements in (a).

We plot in Fig. 2.4(a) the measured magnitude $|g(x_1 - x_2)|$. We fit the measurements to theoretical predictions based on propagating the source Gauss-Schell model in Eq. 2.12 to the detector plane unimpeded (no obstructing object) via Eq. 2.11 after setting $h(x_1, x) = h_{\mathrm{F}}(x_1, x; d)$ with $d = 125$ cm. From the fitting procedure, we estimate the remaining parameters α and σ of the source to be $\alpha = 1/\sqrt{2\ln 2}$ mm and $\sigma = 75/\sqrt{2\ln 2}$ μm, which yield a FWHM beam width of 1 mm and a FWHM coherence width of 75 μm. The model for the source coherence function utilizing these

parameters is given in Fig. 2.4(b). This reference measurement that enabled us to reconstruct the source coherence function $G_{\mathrm{s}}(x', x'')$ is used subsequently in Eq. 2.11 once an object is placed in the field's path.

2.4.4 Coherence Function due to Intercepting Objects

We first consider an intercepting object in the form of a thin metal wire of diameter $w = 0.5$ mm or 1 mm placed between the light source and the detector such that it partially blocks light from reaching the detector. We consider locating the object at different axial distances from the source ($d_1 = 0.5$, 24, and 72 cm) and at various positions along the transverse plane ($x_0 = 0$, ± 50, and ± 100 μm with respect to the optical axis). In each experiment two of these parameters were fixed while varying the third. Because of the small size of the object ($\leq$ 1 mm) placed in an incoherent field and the large distance to the detection plane ($\sim$ 1 m), the intensity distribution at the detection plane (DMD) does not display a clear shadow or directly indicate the existence of an object. Instead, a flat intensity profile is observed over the DMD ($\sim$ 1-mm width under consideration). It is apparent that measuring the two-point field correlations – encoded in $g(x_1 – x_2)$ – over this same spatial extent can help identify the object. Note that $g(x_1 - x_2) = g^*(x_2 - x_1)$, so we plot $g(x_1 - x_2)$ for $x_1 - x_2 \geq 0$ only.

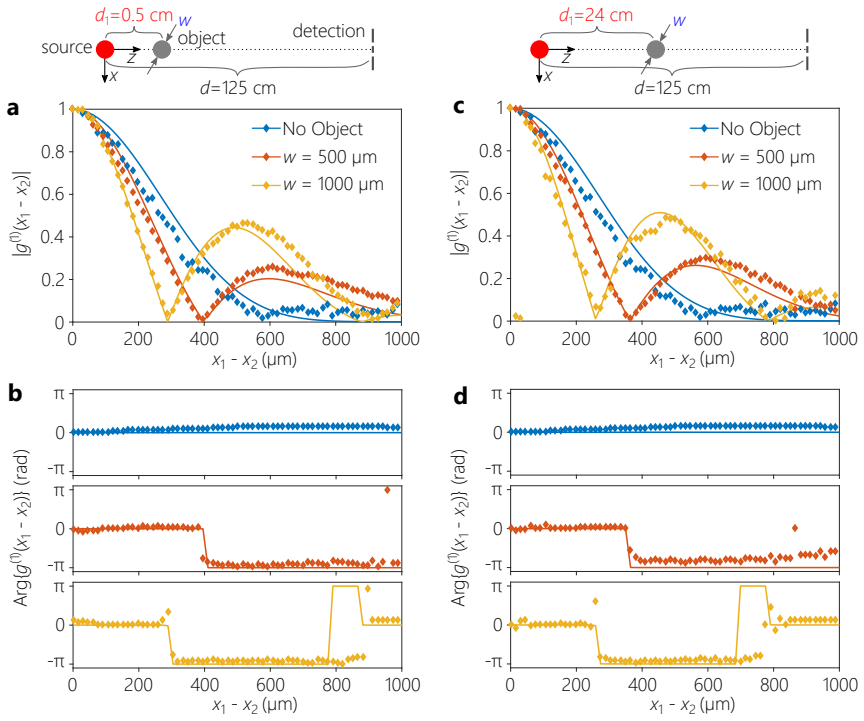

Figure 2.5: Impact of the object size w on the degree of spatial coherence $g(x_1 - x_2)$ when the object location (x_0, d_1) is held fixed for two source-to-object distances; (a,b) $d_1 = 0.5$ cm and (c,d) $d_1 = 24$ cm. (a) The measured magnitude of the degree of coherence $|g(x_1 - x_2)|$ in three cases: unimpeded propagation from the source to the detection plane (no object, $w \to 0$), $w = 0.5$ mm, and $w = 1$ mm. In all cases $x_0 = 0$, $d_1 = 0.5$ cm, and $d = 125$ cm. The schematic above the panel depicts the measurement geometry (the gray circle is the object). The data points are plotted as diamonds, and the solid lines are theoretical predictions based on Eqs. 2.10, 2.11, and 2.12. (b) The measured phases $\mathrm{Arg}\{g(x_1 - x_2)\}$ corresponding to the three cases plotted in (a). The diamonds are data points and the solid lines are theoretical predictions. (c,d) Same as (a,b) except that $d_1 = 24$ cm; that is, the object is placed farther away from the source and closer to the detection plane (the total distance from source to the DMD is held fixed at $d = 125$ cm).

2.4.4.1 Impact of the Object Size

We first examine the effect of the object size w – when its location (x_0, d_1) is fixed – on the coherence function $g(x_1 - x_2)$ in Fig. 2.5. The presence of the object reduces the width of the main lobe of $|g(x_1 - x_2)|$ and introduces a significant side lobe, features that did not exist in the source coherence function measured at the detection plane in absence of an object [Fig. 2.4(a)]. Increasing the object width increases the side-lobe peak amplitude and reduces the width of the lobes [Fig. 2.5(a)].

This can be understood by realizing that the obstructing object modulates the field intensity at the object plane $\tilde{x}$, which now represents a secondary source. In the far-field, the van Cittert-Zernike theorem indicates that the distribution of spatial coherence is related to the Fourier transform of this secondary source intensity distribution when the field is incoherent [91]. The general trends dictated by the van Cittert-Zernike therorem still apply when the field is partially coherent, as is our case here. The nulls of $|g(x_1 - x_2)|$ remain associated with abrupt jumps in phase by π [Fig. 2.5(b)]. Similar results are observed when the object approaches the detection plane [Figs. 2.5(c) and 2.5(d)], with the nulls in $|g(x_1 - x_2)|$ occurring at smaller values of $x_1 - x_2$.

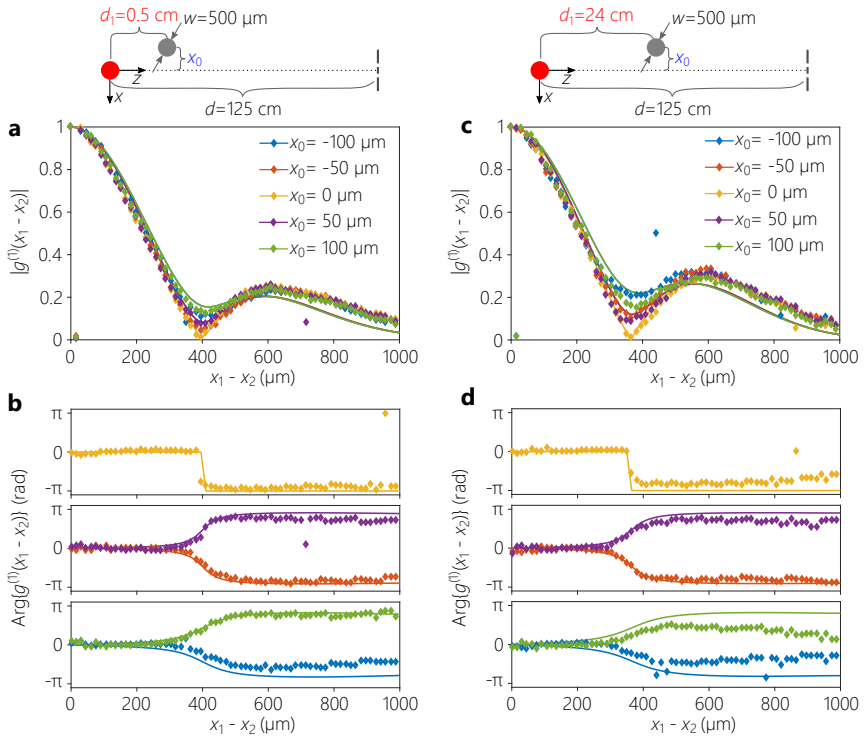

Figure 2.6: Change in the degree of spatial coherence as the object is displaced in the transverse plane with respect to the optical axis, indicated by the coordinate x_0. The experiments are repeated twice, corresponding to the left and right columns. Each experiment has a different source-to-object distance d_1. In the left column (a,b), $d_1 = 0.5$ cm, whereas in the left column (c,d) $d_1 = 24$ cm. In all cases, the object width is $w = 0.5$ mm and the total distance from source to the detection plane is $d = 125$ cm. (a) Measured coherence magnitude $|g(x_1 - x_2)|$ and (b) phase $\mathrm{Arg}\{g(x_1 - x_2)\}$ are shown for an object while varying x_0 from -100 μm to 100 μm. In this experiment, the object is placed at $d_1 = 0.5$ cm. (c,d) Same as (a,b) except that the object is placed at $d_1 = 24$ cm from the source.

2.4.4.2 *Impact of the Object Transverse Location*

Figure 2.6 shows the impact of changing the transverse position x_0 of an object of fixed size ($w = 0.5$ mm) moving in a plane at a fixed distance from the detector. When the object is located on the optical axis, a zero is observed in the coherence function $g(x_1 - x_2) = 0$ for some value of $x_1 - x_2$ set by the object size [Fig. 2.6(a)]. At this null, the phase $\mathrm{Arg}\{g(x_1 - x_2)\}$ undergoes an abrupt jump of π. As the object moves away from the optical axis, the coherence function does not reach zero at the first minimum. Additionally, in lieu of the abrupt π-phase jump, a gradual transition in phase takes place [Fig. 2.6(b)]. As the object moves further away from the optical axis, the drop in $|g(x_1 - x_2)|$ at the first minimum is further diminished and the associated phase change becomes even more gradual.

A measurement of $|g(x_1 - x_2)|$ alone results in an inherent ambiguity with respect to the *direction* of displacement of the object with respect to the optical axis. Therefore the measurements and theoretical predictions for $|g(x_1 - x_2)|$ coincide for displacements of $\pm x_0$. This ambiguity is lifted by observing the *phase* $\mathrm{Arg}\{g(x_1 - x_2)\}$. The gradual phase change at the first minimum of $|g(x_1 - x_2)|$ is in opposite directions for the positive and negative values of x_0, thus helping to identify the object location. Furthermore, both effects that result from a transverse displacement – lifting of the zeros of $g(x_1 - x_2)$ and gradual change in $\mathrm{Arg}\{g(x_1 - x_2)\}$ – are further enhanced as the object approaches the detection plane [Figs. 2.6(c) and 2.6(d)].

2.4.4.3 *Impact of the Object Longitudinal Location*

Finally, we show the effect of moving a $w = 0.5$-mm-wide object along the longitudinal axis z in Fig. 2.7. We hold the total distance between the source and detection plane d fixed and increase d_1. As the object approaches the detection plane (descreasing d_2) while remaining on the optical

axis ($x_0 = 0$), the nulls in $|g(x_1 - x_2)|$ move to smaller values $x_1 - x_2$. In other words, the effect of reducing d_2 for fixed w is similar to that of increasing w for fixed d_2. Indeed, from the van Cittert-Zernike theorem, we expect the width of the coherence function to be related to w/d_2; that is, the angle subtended by the object at the detection plane. Once again, although the van Cittert-Zernike theorem is usually applied to cases where the source is completely incoherent, it is still expected that the general features will apply to a partially coherent field.

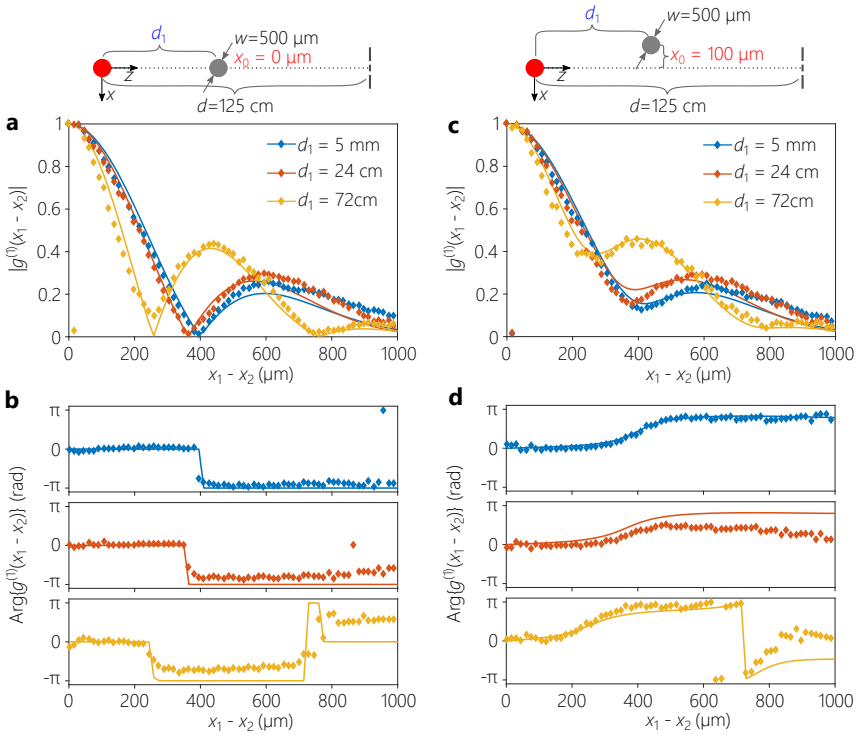

Figure 2.7: Change in the degree of spatial coherence with source-to-object axial distances d_1. The experiments are repeated twice, corresponding to the left and right columns. Each experiment has a different transverse displacements x_0 of the object. In the left column (a,b) we have $x_0 = 0$, whereas in the right column (c,d) $x_0 = 100$ μm. The object width is $w = 0.5$ mm and the total distance from source to the detection plane is $d = 1.25$ m. (a) Measured coherence magnitude $|g(x_1 - x_2)|$ and (b) phase $\mathrm{Arg}\{g(x_1 - x_2)\}$ are shown while varying d_1. In this experiment, the object was placed on the optical axis $x_0 = 0$. (c,d) Same as (a,b) except that the object is displaced from the optical axis to $x_0 = 100$ μm.

2.4.5 Coherence Function due to a Reflecting Object

We now consider reconfiguring the optical arrangement to accommodate the object in reflection mode. Only light reflecting from the object reaches the detection plane [Fig. 2.8]. We collect light that is scattered from the object. The reflective objects were rectangular sections of mirrors of varying widths w. Because light is obliquely incident on the object, the effective size is reduced by the cosine of the incidence angle (the angle between incident and reflected light is $\approx 16^{\circ}$). We expect that if the reflective object size is very large, then light from the source reaches the detection plane with little modification, so that the measured coherence function approaches that of the source [Fig. 2.4(a)]. *Reducing* the reflective object size, on the other hand, is expected to affect the measured coherence by increasing the width of the coherence function (which is in inverse proportion to the size of the secondary source).

The measurement results are presented in Fig. 2.8. The coherence function was measured while varying the width w of the reflective objects from 0.5 mm to 1 mm. The object is placed on the optical axis of the source and its axial distance from the source and detection plane are held fixed. The measured coherence function does not display nulls or a significant side lobe in contrast to the case of intercepting objects. Indeed, the measured $|g(x_1{-}x_2)|$ from the secondary source resembles that of the primary source except from the increased coherence width as the size of the object is reduced. The phase $\mathrm{Arg}\{g(x_1 - x_2)\}$ is flat throughout. We expect that reducing the size of the object further will ultimately introduce nulls in the coherence function and π-phase jumps in its phase distribution.

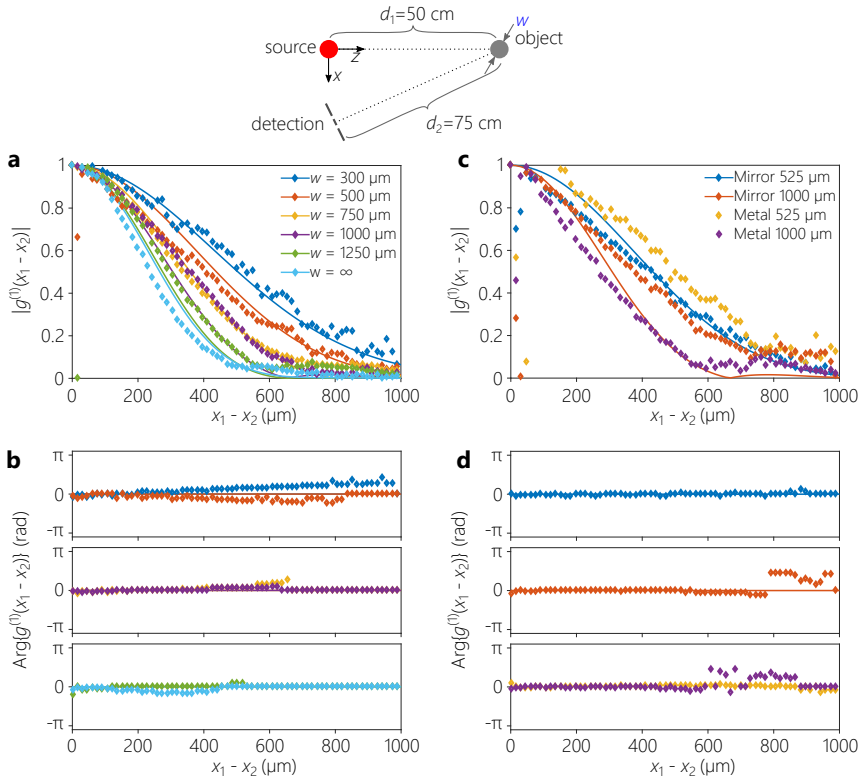

Figure 2.8: Comparison of the degree of spatial coherence for reflective objects of varying widths w. The distance from the source to the object is $d_1 = 65$ cm, and the total distance from source to DMD is $d = 1.45$ m. The objects are placed on the optical axis defines by the source $x_0 = 0$. (a) The coherence magnitude $|g(x_1 - x_2)|$ and (b) phase $\mathrm{Arg}\{g(x_1 - x_2)\}$ are shown while varying w. Experimental results are plotted with diamonds and theoretical predictions are solid lines. The infinite width case is equivalent to free space propagation. The phase $\mathrm{Arg}\{g(x_1 - x_2)\}$ is set to zero when $|g(x_1 - x_2)| \leq 0.05$ to avoid errors stemming from the low signal level.

2.5 Experimental Validation of 2D Model

Now we turn to 2-dimensional scenes with broad-bandwidth radiation emitted from a variety of shaped, equal-area sources. In this experiment, measurements were collected by the DuPSaI device [1]. The apertures were illuminated by a high-power LED with a peak wavelength of 525 nm and a bandwidth of 30 nm (Thorlabs, Solis-525C) and were placed at 1 m distance from the input aperture of the DuPSaI. For the numerical results, the aperture is treated as the source, and the extent of spatial coherence is set to $\ell_c = 4.1\,\mu$m in the plane of the source (full width at half-maximum). We use (2.8) to calculate the spatial coherence function in the detector plane, along the same shear direction x as in the experiment

We first examine the spatial coherence function of the optical fields radiated from two circular apertures, 6 and 5.5 mm in diameter, which differ by only 9% in size. The results are summarized in Fig. 2.9, where we plot the complex degree of coherence $g(\mathbf{r}, \boldsymbol{\rho})$ corresponding to different sources of radiation. The experimentally measured coherence function $G(\mathbf{r}, \mathbf{s})$ function is plotted using circle markers, and the numerical results are plotted with solid lines. The difference between the coherence properties of radiation emitted by sources with diameters of 6 and 5.5 mm is clearly visible, and the agreement between the measurements and these numerical estimations is remarkable. For instance, for the coherence functions in Fig. 2.9(a), the Pearson correlation coefficient takes values of 0.97 and 0.96 for the 6 and 5.5 mm circle apertures, respectively.

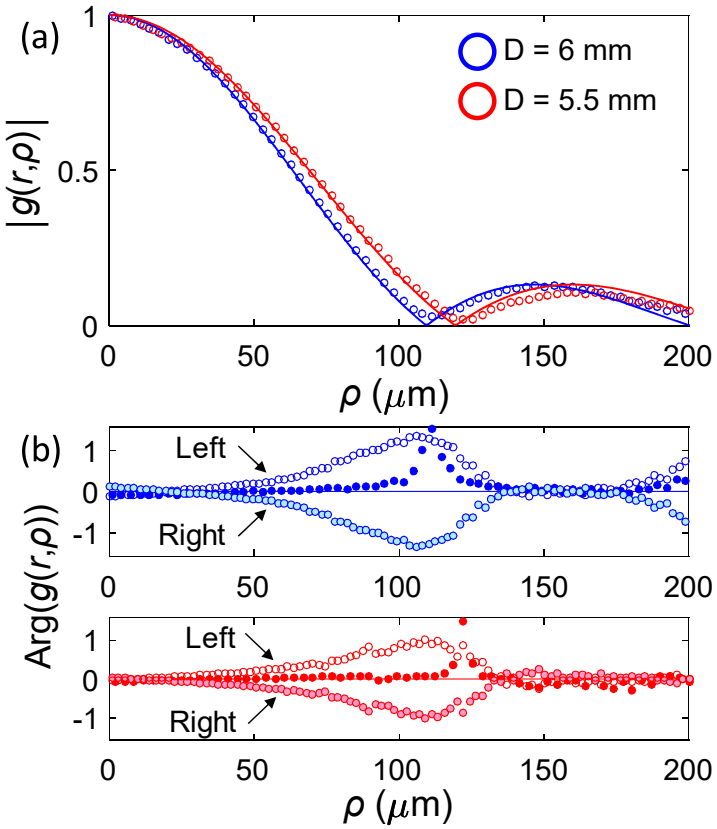

Figure 2.9: (a) Measured magnitude of CDC corresponding to different source diameter sizes (hollow circles), together with corresponding full Fresnel integral calculations (solid lines). (b) Corresponding CDC phases measured along the optical axis and 200 μm to the left and right of the optical axis.

In the next results, we illustrate the ability to discriminate between sources that differ only in their shapes. For this purpose, we constructed three different input apertures having different shapes (circle, square, and equilateral triangle), but the same area of $2.83 \times 10^{-5}\text{m}^2$ to emulate sources emitting the same amount of power within the same spectral range. As can be seen in Fig. 2.1, the shape information is already lost in the intensity distribution recorded at 20 cm away from the

source. However, quite different coherence functions are being detected at 100 cm from the source, as seen in Fig. 2.10. When compared with the numerical propagation, a good agreement is found for all shapes.

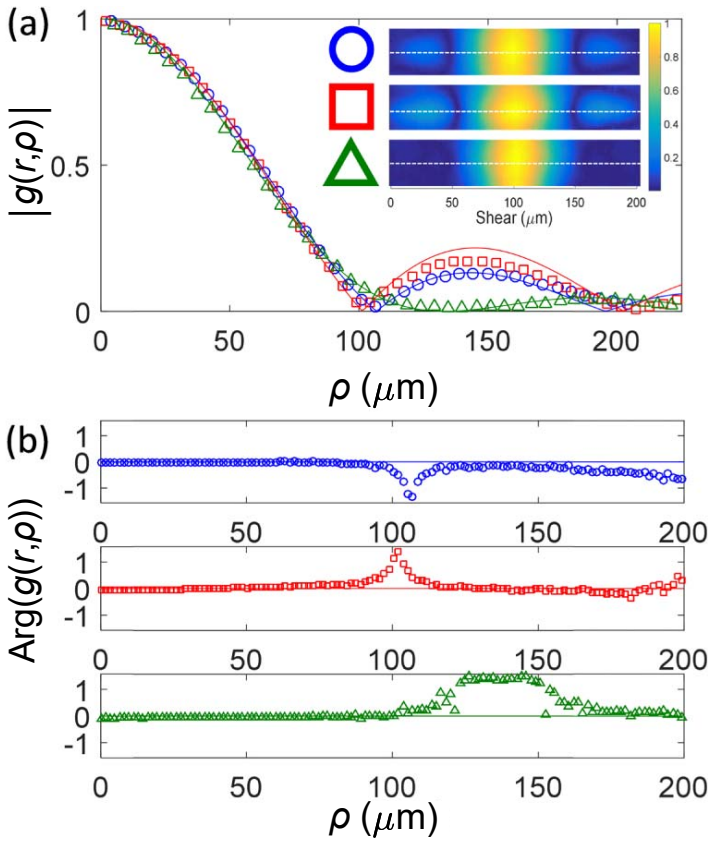

Figure 2.10: (a) Measured magnitude of CDC corresponding to different source shapes (marker lines), together with corresponding calculations using the Fresnel integral (solid lines). The inset is the experimental 2D coherence function, while the white dotted lines indicate the cross-sectional part plot in (a). (b) Corresponding CDC phases.

Finally, we will show how spatial coherence measurements can be used to discriminate between

different orientations of the source. In Fig. 2.11, we present the experimental results corresponding to the square aperture rotated by 45 deg and the equilateral triangle rotated by 90 deg.

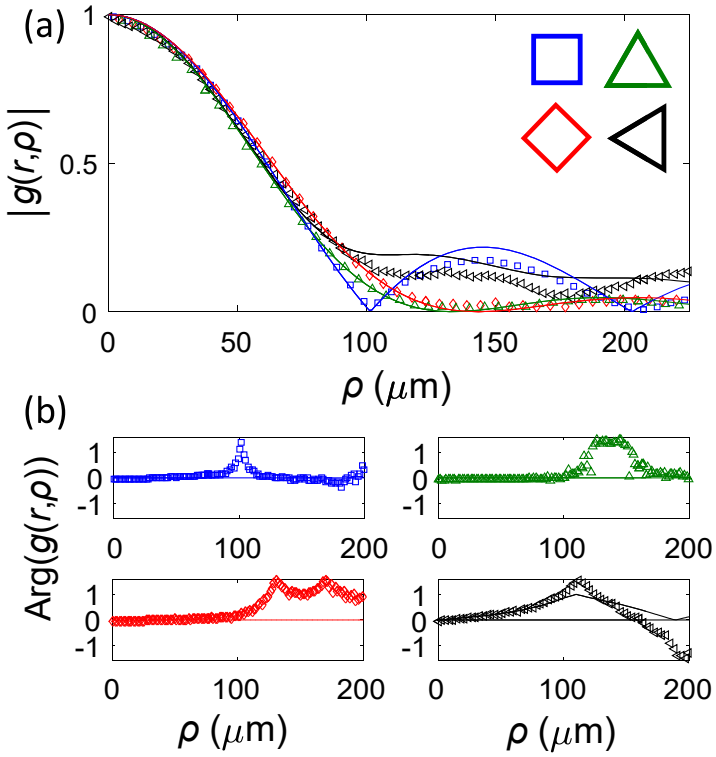

Figure 2.11: (a) Measured magnitude of CDC corresponding to different source shapes, as well as different orientations of the source, together with corresponding simulations using the full Fresnel integral. (b) Corresponding CDC phases.

2.6 Analytic Calculations of Propagated Fields

In Section 2.2.3 we formally defined generalized sources. We now consider how these sources can be used to efficiently calculate the propagation of the spatial coherence function through a scene.

We provide details on the validity conditions that must be satisfied for our approach to succeed, and present the main theorem. Examples of generalized sources and numerical results obtained using the main theorem are illustrated in Section 2.6.3.

Technical details such as the evaluation of the Fourier transform of a truncated Gaussian field and the proof of the main theorem are presented in Appendix A.We consider 1D scenes here, but the techniques are readily extendable to 2D scenes.

We first review the well-known propagation properties of Gauss-Schell (GS) model sources.

2.6.1 Free Space Propagation of Gauss-Schell Model Sources

A useful feature of the Gauss-Schell model is that its structure is propagation-invariant except for an overall phase. Indeed, after propagating a distance d_{o}, Eq. 2.2 takes the same form except for a phase factor,

$$G^{-}(y_1', y_2') = A\, \exp\{iy_1'y_2'/R^2\} N^w\left(y_1'\right) N^\sigma\left(y_2'\right), \tag{2.13}$$

where the modified Gauss-Schell parameters A, w, and σ, in addition to the new parameter R (the radius of curvature of the quadratic phase), are related to the original parameters A_{o}, w_{o}, and σ_{o} through

$$A = \frac{A_{\mathrm{o}}}{\sqrt{1+\xi_{\mathrm{o}}^2}}\,, \tag{2.14a}$$

$$R = \ell_{\mathrm{o}} \frac{\sqrt{1+\xi_{\mathrm{o}}^2}}{\xi_{\mathrm{o}}}\,, \tag{2.14b}$$

$$w = w_{\mathrm{o}}\sqrt{1+\xi_{\mathrm{o}}^2}\,, \tag{2.14c}$$

$$\sigma = \sigma_{\mathrm{o}}\sqrt{1+\xi_{\mathrm{o}}^2}\,, \tag{2.14d}$$

where $\ell_{\rm o} = \sqrt{d_{\rm o}/2k}$, $\xi_{\rm o}$ is a unitless quantity given by $\xi_{\rm o} = \frac{\ell_{\rm o}^2}{w_{\rm o}\sigma_{\rm o}} = \frac{d_{\rm o}}{z_{\rm GS}}$, and $z_{\rm GS} = 4\pi\frac{\sigma_{\rm o} w_{\rm o}}{\lambda}$ is an effective Rayleigh range for the Gauss-Schell model (see [71, 72] for an in-depth discussion of the free space propagation of a Gauss-Schell source).

We take the form in Eq. 2.13 to be the standard GS-model hereon, defined by four parameters (A, R, w, σ). Any additional propagation of the GS-field does not change its form. Propagation a distance d produces the same GS-model after transforming the parameters $(A, R, w, \sigma) \to (\tilde{A}, \tilde{R}, \tilde{w}, \tilde{\sigma})$, with

$$\tilde{A} = \frac{A}{(1+\delta)\sqrt{1+\xi^2}}, \tag{2.15a}$$

$$\tilde{R} = R\sqrt{\frac{(1+\delta)(1+\xi^2)}{1+(1+\frac{1}{\delta})\xi^2}}, \tag{2.15b}$$

$$\tilde{w} = w\,(1+\delta)\sqrt{1+\xi^2}, \tag{2.15c}$$

$$\tilde{\sigma} = \sigma\,(1+\delta)\sqrt{1+\xi^2}, \tag{2.15d}$$

where $\xi = \ell^2/\{w\sigma(1+\delta)\} = d/z_{\rm GS}$, $z_{\rm GS} = 4\pi\sigma w(1+\delta)/\lambda$ is a scaled Rayleigh range, $\ell = \sqrt{d/2k}$, and $\delta = \ell^2/R^2$ [71, 72]. In other words, after propagation in free space a distance d, the GS-field coherence becomes

$$\widetilde{G}_d(y_1, y_2) = \widetilde{A}\,\exp\left(iy_1y_2/\widetilde{R}^2\right) N^{\tilde{w}}\,(y_1)\,N^{\tilde{\sigma}}\,(y_2). \tag{2.16}$$

2.6.2 *Propagation of Fields Produced by a Generalized Source*

In this section, we give a closed-form formula for the propagated coherence function of generalized sources that satisfy the following condition on the intensity and coherence widths

$$w > 10^2\sigma > 10^3\lambda. \tag{2.17}$$

This relation requires that intensity slowly varies with regard to the coherence width, and the coherence slowly varies with respect to the wavelength. The transmission function t of the generalized source is segmented into piecewise constant intervals, where $t(x) = c_j$ for $x \in [a_j, a_{j+1})$, $j = 0, ..., N$, $-\infty = a_0 < a_1 < \cdots < a_N < a_{N+1} = \infty$, and N is arbitrarily fixed, where each c_j is a complex-valued constant, $j = 0, \ldots, N$. The theorem we prove below requires that the breakpoints and intervals satisfy the relations

$$\sum_{j=1}^{N} N^w \left(|a_j| - 3\sigma\right) < 4, \tag{2.18a}$$

$$\min_{j=2,\ldots,N} (a_j - a_{j-1}) > 3\sigma. \tag{2.18b}$$

These relations put a limit on the resolution and number of features present in the transmittance function. The first relation places a limit on the number of sections located close to the center of the field, while the second relation ensures that none of these sections is too small relative to the coherence width. While sufficient but not necessary, the constraints in (2.18) allow for a wide range of partially coherent sources of practical interest, as will be shown in the examples and numerical results below.

Before we state our main result, recall the definition of the Hilbert Transform of a square integrable

function f,

$$Hf(\omega) := \text{p.v.}\frac{1}{\pi}\int \frac{f(s)}{\omega - s}ds, \tag{2.19}$$

where the standard notation p.v. stands for principal value. For some real parameter u, we also define a conjugated Hilbert transform as

$$\begin{aligned} H^u f(\omega) &:= \exp(-i\omega u)\, H\left\{\exp(isu)\, f(s)\right\}(\omega) \\ &= \exp(-i\omega u)\, \text{p.v.}\frac{1}{\pi}\int \frac{\exp(isu)\, f(s)}{\omega - s}ds. \end{aligned} \tag{2.20}$$

We proceed to our main result given in (2.21), which provides an effective approximation of the coherence function at a given distance from the generalized source. The formula (2.21) characterizes the coherence function G_d in terms of the coherence of the GS-field propagated a distance d in free space and a multiplicative term – expressed in terms of weighted conjugated Hilbert transforms of a Gaussian – capturing the modification due to interaction with the transmission function. In obtaining our approximate formula, we consider the individual contributions of the different segments of the transmission function to the total coherence. This in turn yields an approximation to the coherence function based on Fourier transforms of truncated Gaussians giving rise to the conjugated Hilbert transform terms – a relationship which has not been previously shown.

The technical bounds on the error of our approximate formula are provided in the proof in Appendix A.

Theorem. *Let λ be the wavelength, w be the width of the beam intensity profile, and σ be the transverse coherence width. A generalized source as in* (2.3) *satisfying* Eqs. *(2.17,2.18) is situated*

at the plane $z=0$. At the detection plane $z=d$, the coherence $G_d(y_1, y_2)$ is well approximated by

$$\begin{aligned}\overline{G}_d(y_1, y_2) =& \widetilde{G}_d(y_1, y_2) \frac{i}{2N^{\eta\widetilde{\sigma}}(y_2)} \\ & \times \sum_{j=2}^{N} T_{j,j} \left[\left(H^{b_j(y_1)} - H^{b_{j-1}(y_1)} \right) N^{\widetilde{\sigma}/\eta} \right](y_2) \end{aligned} \tag{2.21}$$

where $\widetilde{G}_d(y_1, y_2)$ is the coherence of the free propagating GS-field in (2.16)*, $T_{j,j} = |t(x)|^2$ for $x \in [a_{j-1}, a_j)$, and*

$$\eta = \sqrt{1 + \frac{\sigma^2 \widetilde{\sigma}^2}{\ell^4}}, \tag{2.22a}$$

$$b_j(y_1) = \frac{1}{\eta^2 \ell^2} \left(a_j - \frac{y_1}{(1+\delta)(1+\xi^2)} \right). \tag{2.22b}$$

We note that (2.21) recovers a close approximation to (2.16) for the special case of uniform transmittance. The difference is due to the finite extent of the source. While (2.21) shows that the contribution of each segment of the transmission function as in (2.17) and (2.18) is essentially independent, note that we do not assume a priori independence in the contributions of the segments to the coherence.

As shown, information about the transmission function (the breakpoints a_j) is explicit in the parameters b_j of the conjugated Hilbert Transform in (2.22b) and the transmission coefficients $T_{j,j}$, wherefore the formula in (2.21) is valuable in the inverse problem of recovering the transmission function from coherence measurements.

2.6.3 *Examples of Generalized Sources*

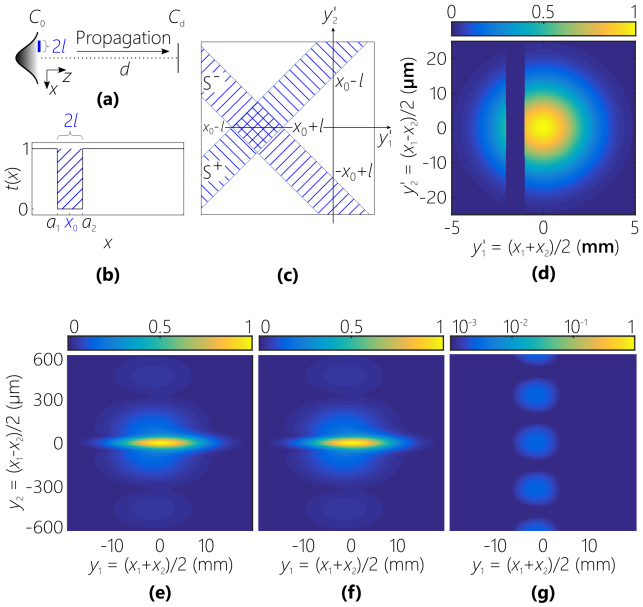

Figure 2.12: One object example with numerical results showing propagated coherence function in the plane at $z = 1$ m. (a) Diagram of the scenario. (b) Transmission function. (c) Transmission function to be applied in coherence space. The striped regions show the support of the inverted transmission function $1-t(y_1'+y_2')t^*(y_1'-y_2')$. (d) Modulus of source coherence function. (e) Modulus of coherence function obtained using numerical integration of propagation function (2.6). (f) Modulus of coherence function obtained using approximation (2.21) of the theorem. (g) Magnitude of error between complex coherences calculated by (2.6) and (2.21). All plots are normalized against the maximum value attained in (e) and (f). (g) is plotted on a logarithmic scale to accentuate the small error. It should be noted that the scale of the y_2' axis is much smaller than the scale of the y_1' axis, and so the "strips" mostly overlap in the plotted region. The parameters for the source Gaussian are $A = 1$, $w \approx 1.7$ mm (yielding an intensity FWHM of 4 mm), $\sigma \approx 8.5$ μm (yielding a coherence FWHM of 20 μm), and the source has no phase (i.e. in the limit as $R \to \infty$). The wavelength is $\lambda = 632$ nm. The parameters for the object are $x_0 = -1.5$ mm and $l = 0.5$ mm.

For clarity of exposition, we analyze first the case of an object comprising a single segment ($N = 2$) and then extend this to an example of an arbitrary generalized source. In this scenario, we assume that a Gauss-Schell model field exists at $z = 0$. The source is blocked by a single object centered along the transverse axis at $x = x_0$ with half-width l, and therefore its breakpoints are $a_1 = x_0 - l$ and $a_2 = x_0 + l$. The scenario is depicted in Fig. 2.12(a) and the transmission function is shown in Fig. 2.12(b). For this example, we consider the inversion of the transmission function in the coherence space $1 - t(y_1' + y_2')t^*(y_1' - y_2')$. The inverted transfer function is chosen so that the coherence function G is supported only on the union $S^+ \cup S^-$ of the "strips" shown in Fig. 2.12(c). As described in Appendix A, these strips directly admit the closed-form solution presented in (2.21). The source coherence function G for this example is plotted in 2.12(d). Fig. 2.12(e) shows the function obtained using numerical integration of (2.6), and Fig. 2.12(f) shows the approximated results obtained using (2.21). The error in Fig. 2.12(g), which is plotted on a logarithmic scale, demonstrates good agreement between the exact and approximate equations.

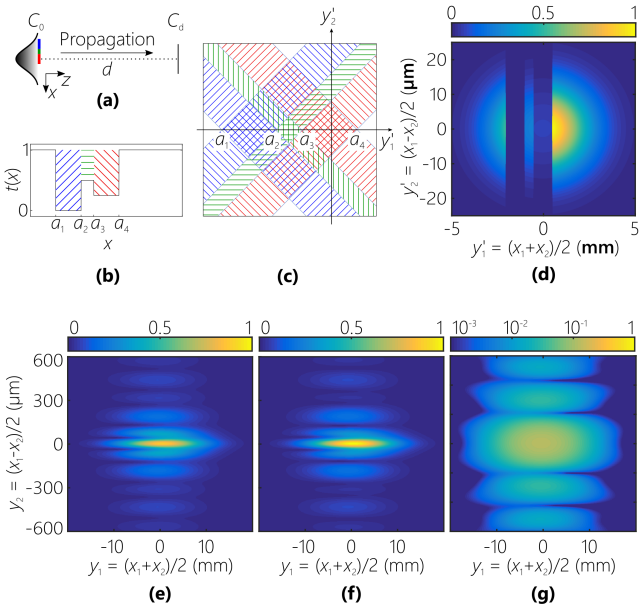

Figure 2.13: Generalized source example with numerical results showing propagated coherence function in the plane at $z = 1$ m. (a-g) are the same as in Fig. 2.12. As with the one object example, the source parameters are $A = 1$, $w \approx 1.7$ mm, $\sigma \approx 8.5$ μm, $\lambda = 632$ nm, and no phase. The breakpoints are at $a_1 = -2$ mm, $a_2 = -1$ mm, $a_3 = -0.5$ mm, and $a_4 = 0.5$ mm with transmissions $t((-\infty, a_1)) = 1$, $t([a_1, a_2)) = 0$, $t([a_2, a_3)) = 0.5$, $t([a_3, a_4)) = 0.25$, and $t([a_4, \infty)) = 1$.

The next example demonstrates how the one object case naturally extends to more complicated transmission functions. We will consider a similar scenario as for the previous example, except the transmission function has two additional sections (see Fig. 2.13(a) and (b)). Each piecewise constant section j of the transmission function influences two strip regions

$$S_j^{\pm} = \{(y_1', y_2') \in \mathbb{R}^2,\ a_{j-1} \leq y_1' \mp y_2' \leq a_j\}. \tag{2.23}$$

As can be seen in Fig. 2.13(c), the interaction between these strips gives rise to N^2 piecewise

constant sections in the coherence space transmittance. The theorem asserts that the only sections needed to form the approximation are those that fall on the y_1 axis. Because the transmission function for this example is inverted, the true propagated output G_d is given by

$$G_d(y_1, y_2) = G_d^-(y_1, y_2) - \overline{G}_d(y_1, y_2) \tag{2.24}$$

where G_d^- represents the propagated coherence of the unmasked Gaussian input function and $\overline{G}_d$ the propagated coherence function due to the inverted transmission function. We show the numerical results in Fig. 2.13(e-g).

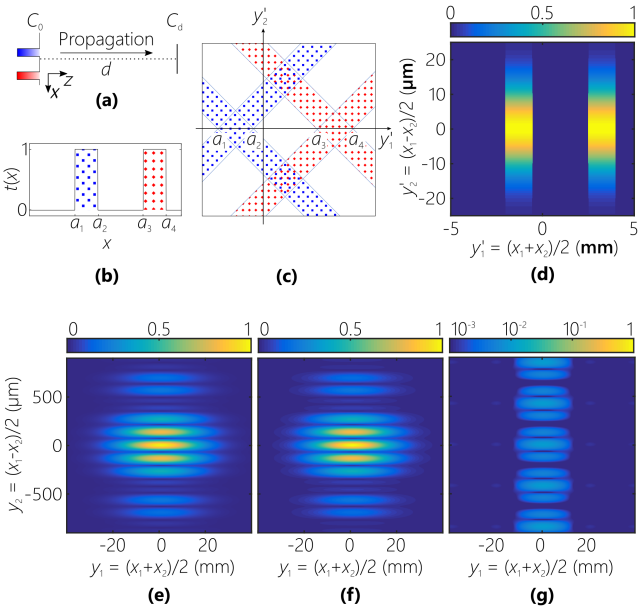

Figure 2.14: Uniform source example with numerical results showing propagated coherence function in the plane at $z = 2$ m. (a-g) are the same as in Fig. 2.12, except that (c) shows strips due to the non-inverted transmission function $t(y_1' + y_2')t^*(y_1' - y_2')$. The source parameters are $A = 1$, $w = 1$ m (thus approximating a uniform source), $\sigma \approx 8.5$ μm, $\lambda = 632$ nm, and no phase. The breakpoints are at $a_1 = -2$ mm, $a_2 = -0.5$ mm, $a_3 = 2.5$ mm, and $a_4 = 4$ mm with transmissions $t((-\infty, a_1)) = t([a_2, a_3)) = t([a_4, \infty)) = 0$, $t([a_1, a_2)) = t([a_3, a_4)) = 1$.

We present a final example demonstrating the approximation of a uniform source by a wide Gaussian (in this case $w = 1$ m). The source is shown in Fig. 2.14. Unlike the previous two examples, here in the coherence space we use the transmission function $t(y_1' + y_2')t^*(y_1' - y_2')$. The numerical simulation is shown in Fig. 2.14(e-g). The numerical integration and approximated results are in very good agreement with a maximum error of ≈ 0.001.

CHAPTER 3: INVERSE PROBLEM FOR FREE SPACE PROPAGATION

3.1 Introduction

In this chapter, we exploit the techniques developed in Chapter 2 to tackle the inverse problem in LOS scenarios[1]. For simplicity, we limit this study to the one-dimensional model containing fields with one transverse coordinate x (assuming all fields are uniform along the other coordinate). However, the techniques developed here are extendable to higher dimensions.

Despite an abundance of methods for measuring the coherence function, there are very few works that use this data to recover the source. For non-radiating sources, unique determination ideas appeared in [94, 95]. In the Fresnel regime, some Fourier-based inversion methods use the van Cittert-Zernike theorem to recover the intensity distribution across incoherent sources [91], and the more complicated case of partially coherent quasi-homogeneous sources [96–98]. Further algorithms use only the modulus of the Fourier transform [58,99], with various extensions (e.g., the use of apriori constraints [100] or coherent illumination [101]) which improve the reconstruction. However, the accuracy of these methods degrades with the increase in the coherence of the source. Other means of inversion are based on coherent modes [102] or Fresnelets [103].

The complex field amplitude $U(\mathbf{r})$ associated with a *coherent* monochromatic scalar optical field provides a complete representation; once the amplitude *and* phase of $U(\mathbf{r})$ are measured, the field can be computed in any other plane using the diffraction propagator [91]. Likewise, with spatially *incoherent* light, since the spatial coherence function provides a complete representation, determining the spatial coherence in one plane allows evaluating it at any other plane. Based on this

[1] In this chapter, we partially use the material published in Optics Letters, 2017 [8] and the Journal of the Optical Society of America A (JOSA A), 2018 [10].

insight, we use experimentally-obtained measurements of the coherence function of the optical field from an LED that is intercepted by a 'scene' comprising one or more obstacles, as reported in [8]. The partially coherent field evolves after the scene until intensity variations representative of the objects (shadows) are no longer discernible. The coherence function is measured by the double-slit experiment described in Fig. 1.4. We use the magnitude and phase of $G(x_1, x_2)$ experimentally obtained at the detection plane, and then back-propagate $G(x_1, x_2)$ towards the source to visually discover the scene and locate the scattering objects. As shown in Chapter 2, measuring G along the $x_2 = -x_1$ axis helps identify the transverse location and subtended angle (object width divided by its distance to the detection plane) of a single scattering object [2]. To identify the width and axial location separately, along with the transverse location, and – furthermore – to reconstruct a more complex scene, a measurement of the full coherence function becomes necessary.

While the above-mentioned inversion methods allow for the estimation of arbitrary intensity profiles, in practice, they all suffer from large sampling complexity. Specifically, in order to invert a Fourier or Fresnel transform, a large number of measurements is necessary to attain the required sampling rate. In the back-propagation approach (which requires the full coherence function), the source is traced back in an increasing sequence of distances away from the measurement plane; hence, the reconstruction requires identification of the correct axial distance. This information is typically unavailable or hard to obtain. Even if the distance is identified, all calculations at the intermediate locations would then be discarded, which adds an unnecessary computational expense.

For this reason, we next present an inversion method to reconstruct sources from coherence measurements, while avoiding the aforementioned pitfalls. We exploit the additional dimension in the coherence data to devise a global inversion method that applies local minimization to a family of residuals sharing a unique minimum, a task that would be difficult from intensity-only measurements. In Chapter 2, we studied the propagation of the spatial coherence of fields from *generalized sources* in the Fresnel regime. Such sources are modulations of the field produced by a Gauss-

Schell source by a piecewise constant transmission function, thus modeling the field's interaction with objects and apertures. We adopt this formulation due to the analytical tractability of its forward model and its applicability to many practical scenarios of interest. Our focus here is on the inverse problem in which we seek to determine both the transmission function and the distance to the generalized source from the measurement plane from sampled coherence measurements. Leveraging the closed-form approximations (which are explicit in the parameters of the transmission function) along with parametric modeling of the scene, we develop a gradient-descent-based approach to the inverse problem. The proposed algorithm yields accurate estimates of the parameters of the scene with low sampling complexity, i.e., only few measured samples of the coherence function suffice for the algorithm to converge to the actual parameters. While we focus on intercepting objects, which obstruct part of the light source, the method applies to more complex source structures as in (2.3) below. In particular, the complementarity in the Babinet principle for mutual intensity [104], directly allows the method to apply to secondary sources or apertures. An added benefit in using coherence data is the overdeterminancy of the problem which we exploit to develop a robust inversion method. We start with a simple model involving one source. The goal is to estimate its position, width, and distance from coherence measurements. Inversion using both numerically simulated, and experimental data are presented to demonstrate the algorithm's effectiveness. A second example considers two sources whether located in the same or in different transverse planes. In each example, it is assumed that the number of breakpoints of the transmission function is known. To avoid any inverse crime in the numerical experiments, the simulated data in the forward model is generated via a method (brute force numerical integration) different from the method used for the inversion (based on an analytic formula).

3.2 Inversion of the Fresnel Operator

3.2.1 Theory

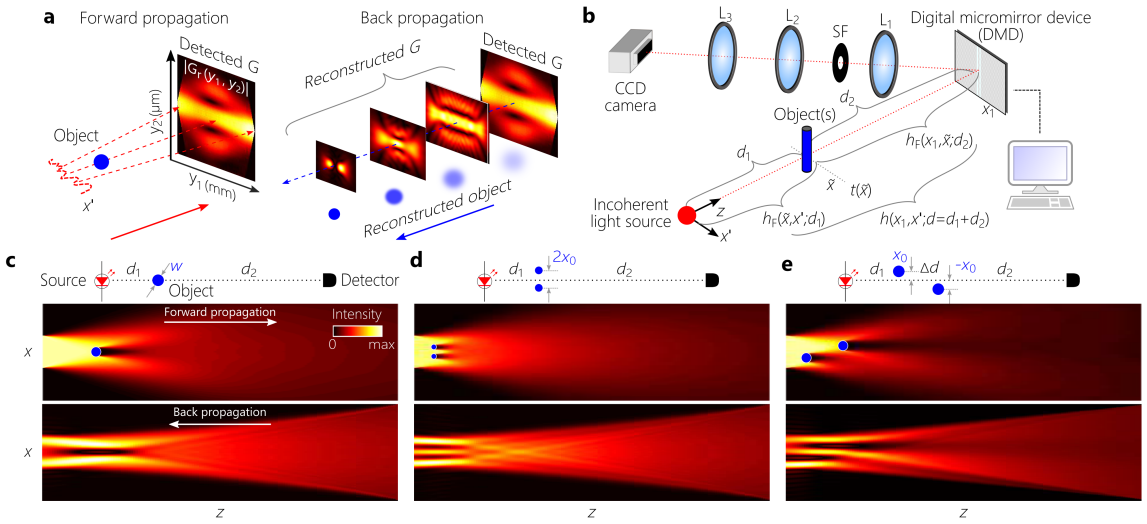

Figure 3.1: (a) Concept of lensless coherence imaging. The coherence function $G(x_1, x_2; d)$ after scattering from an object is measured at a plane $z = d$, and then back-propagated computationally to the object. (b) Schematic of the measurement setup where relay lenses (L_1=10 cm and L_2=20 cm) are followed by a third lens in a $2f$ configuration (L_3=20 cm). SF: spatial filter. (c) A 'scene' configuration comprising a single on-axis object with diameter $w = 0.5$ mm, and $d_1 = 22$ cm. The distance between the source and detector plane $d = d_1 + d_2 = 144$ cm is maintained throughout. In the forward direction, the object casts a shadow that washes out in the far-field. In the back-propagation direction, the object is replaced by an intensity dip that is symmetric with respect to the object location. (d) Configuration comprising two identical objects located in the same axial plane with $w = 0.25$ mm, $x_0 = 0.287$ mm, and $d_1 = 7$ cm. (e) Configuration comprising two identical objects located in two different axial planes separated by a distance $\Delta d = 15$ cm, with $w = 0.5$ mm, $x_0 = 0.375$ mm, and $d_1 = 7$ cm. (c)-(e) In all simulations, $0 \leq z \leq 144$ cm and the x-axis spans 6 mm.

We first review the forward propagation model, which has already been discussed in Chapter 2. Starting from a planar source having a coherence function $G(x', x''; z=0)$, the coherence function at points x_1 and x_2 in a plane at $z=d$ after traversing a linear system having an impulse response function $h(x_1, x')$ is

$$G(x_1, x_2; d) = \iint dx' dx'' h(x_1, x') h^*(x_2, x'') G(x', x''; 0). \tag{3.1}$$

Here, h need not be unitary, so that systems including obstructions can be described in this way. In our experiments, h comprises free space propagation and interaction with opaque objects; see Fig. 3.1. Propagation a distance z is represented with a Fresnel integral of kernel $h_{\mathrm{F}}(x_1, x'; z) \propto \exp\{i\frac{k}{2z}(x_1 - x')^2\}$ [91]. In one configuration, h comprises a sequence of free propagation a distance d_1 from the source, a thin opaque object represented by a transmittance $t(\tilde{x})$, followed by propagation a distance d_2 to the detection plane [Fig. 3.1(a,b)]. This cascade is represented by the impulse response function

$$h(x_1, x'; d = d_1 + d_2) = \int d\tilde{x}\ h_{\mathrm{F}}(x_1, \tilde{x}; d_2)\ t(\tilde{x})\ h_{\mathrm{F}}(\tilde{x}, x'; d_1), \tag{3.2}$$

and the coherence function at the detector is

$$G(x_1, x_2; d) = \iint d\tilde{x} d\tilde{\tilde{x}} h_{\mathrm{F}}(x_1, \tilde{x}; d_2) h_{\mathrm{F}}^*(x_2, \tilde{\tilde{x}}; d_2) t(\tilde{x}) t^*(\tilde{\tilde{x}}) G^-(\tilde{x}, \tilde{\tilde{x}}; d_1), \tag{3.3}$$

where $G^-(\tilde{x}, \tilde{\tilde{x}}; d_1)$ is the coherence function immediately before the object. We also define a coherence function immediately after the object $G^+(\tilde{x}, \tilde{\tilde{x}}; d_1) = t(\tilde{x}) t^*(\tilde{\tilde{x}}) G^-(\tilde{x}, \tilde{\tilde{x}}; d_1)$.

We now discuss the inversion of the previously described forward propagation operators. The specific form of the unitary operator for the Fresnel kernel $h_{\mathrm{F}}(x_1, x; z)$ [105] leads to the identity $h_{\mathrm{F}}^*(x, x_1; z) = h_{\mathrm{F}}(x, x_1; -z)$ and a composition rule $\int d\tilde{x} h_{\mathrm{F}}(x_1, \tilde{x}; d_2) h_{\mathrm{F}}(\tilde{x}, x; d_1) = h_{\mathrm{F}}(x_1, x; d_1 +$

d_2). By setting $h_{\rm F}(x_1, x; 0) = \delta(x_1 - x)$, $h^*_{\rm F}(x, x_1; z)$ becomes the inverse of $h_{\rm F}(x_1, x; z)$:

$$\int d\tilde{x} h_{\rm F}(x_1, \tilde{x}; z) h^*_{\rm F}(\tilde{x}, x_1; z) = \delta(x_1 - x). \tag{3.4}$$

Therefore, starting from the coherence function at the detector plane given in Eq. 3.3, we can *back-propagate* G computationally a distance z towards the object by applying the operator $h^*_{\rm F}(x, x_1; z) = h_{\rm F}(x, x_1; -z)$. When $z = d_2$, the back-propagated coherence function becomes $G^+(\tilde{x}, \tilde{\tilde{x}}; d_1)$ and the intensity $I^+(\tilde{x}; d_1) = |t(\tilde{x})|^2 I^-(\tilde{x}; d_1)$, where $I^-(\tilde{x}; d_1)$ is the intensity from the source immediately preceding the object.

The strategy is thus to use the measured complex coherence function and then carry out the back-propagation to reconstruct the scene.

3.2.2 Results

In the experiments, the coherence function $G_{\rm r}(y_1, y_2)$ is measured using the setup shown in Fig. 1.4. The experimental light source is as described in Section 2.4.1. The experiment was initially carried out in absence of objects (unobstructed propagation from the 'primary' source to the detector) to calibrate the measurement system. The distance between the source and detector $d = 1.44$ m is held fixed in all our experiments. We substitute the measured $G_{\rm r}(y_1, y_2; d)$ in the right-hand side of Eq. 3.1, replace $h(x_1, x)$ by $h^*_{\rm F}(x, x_1, -z)$, and set the back-propagation distance to $z = d$. A calibration phase is assessed that produces a maximum intensity profile at the source plane of the back-propagated signal. We can then proceed to reconstructing 'secondary' sources – the scattering objects using the experimentally measured coherence function.

We now describe the back propagation results based on experimental measurements from [8]. For each of the three scenarios, Fig. 3.1(c)-(e) show the configuration. These panels also show back-

propagation results using a coherence function which was numerically calculated at the detector plane using (2.6).

We first consider the case where an object (a metal wire of diameter $w = 0.5$ mm at $d_1 = 22$ cm from the source) obstructs the field [Fig. 3.1(c)]. Diffraction after the object smears out the shadow, as predicted by a forward-model calculation [Fig. 3.1(c)] and confirmed in the measured $|G_{\rm r}(y_1, 0; d)|$ [Fig. 3.2(a)]. By back-propagating the measured complex coherence function $G_{\rm r}(y_1, y_2; d)$ [Fig. 3.2(a,b)] and increasing the back-propagation distance z, we construct the coherence function $G_{\rm r}(y_1, y_2; z)$ at planes preceding the detection plane axially and gradually approaching the object, samples of which are shown in Fig. 3.2(d). From $G_{\rm r}(y_1, y_2; z)$ we can extract the evolution of the intensity distribution $I(y_1; z)$ along the propagation axis by setting $y_2 = 0$ at every plane [Fig. 3.2(d)]. Note the different scales along transverse (vertical) direction x (4 mm) and longitudinal (horizontal) direction z (1.44 m) in Fig. 3.2(c).

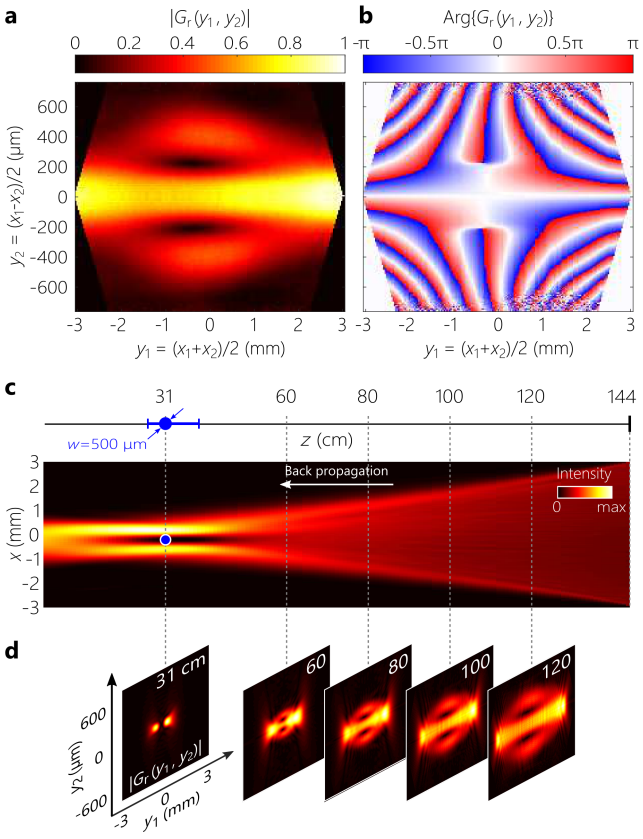

Figure 3.2: Back-propagation of the measured coherence function for the configuration in Fig. 3.1(c) comprising a single object. (a) Measured amplitude $|G_{\rm r}(y_1, y_2)|$ and (b) *wrapped* phase $\mathrm{Arg}\{G_{\rm r}(y_1, y_2)\}$ of the coherence function in the rotated coordinate system (y_1, y_2). The phase-wrapping has no effect on the back-propagation. (c) Back-propagated intensity $I(x; z)$ along z. The estimated object width is 380 μm by finding the half-way point between the dip minimum and peak magnitude of the intensity in the object plane. The axial error bar indicates where the magnitude remains within 5% of the minimum. (d) Back-propagated $G_{\rm r}(y_1, y_2; z)$ at selected distances from the source.

The back-propagation yields a localized 'shadow' of the object in the intensity profile that provides an estimate of the size and position (transverse and longitudinal) of the object [Fig. 3.2(c)]. For simplicity, we consider the 'focal plane' to be the plane in which the dip in the intensity profile

reaches its minimum. The error in estimating the location of the object from the detection plane is $\approx 7.4\%$. Note that the width of the intensity distribution decreases as we travel backwards and at the object plane is quite narrow; contrary to the extremely wide field produced from the LED. This is due to the finite size of the detection area: the source field far from the optical axis at the *object* plane does not contribute to the *detection* plane.

We next consider a scenario where two co-planar objects: two metal wires of equal diameters $w = 0.25$ mm separated by $2x_0 = 0.575$ mm and placed at a distance $d_1 = 7$ cm from the source [Fig. 3.3(a)]. The shadow cast by the two objects has mostly smeared out at the detector plane; see $|G_{\rm r}(y_1, 0; d)|$ in Fig. 3.3(a). The measured complex $G_{\rm r}(y_1, y_2; d)$ [Fig. 3.3(a,b)] is back-propagated [Fig. 3.3(d)], and we extract the evolution of the intensity $I(y_1; z)$ along the propagation axis as before [Fig. 3.3(c)]. The back-propagation yields two localized 'shadows' of the objects in the intensity profile from which we estimate the size and position of the two objects [Fig. 3.3(c)]. The error in estimating the location of the objects from the detection plane is $\approx 3.6\%$.

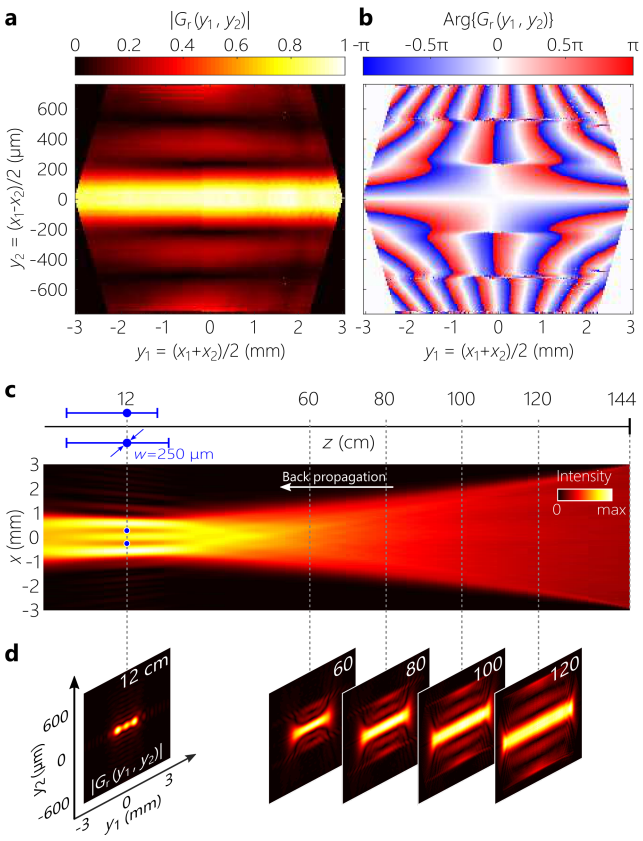

Figure 3.3: Same as in Fig. 3.2, except that the two-object scene in Fig. 3.1(d) is employed. The two identical objects have a diameter of 250 μm (smaller than that of the object in Fig. 3.2) and are placed in the same transverse plane. The object widths are estimated at ≈ 280 μm at $d_1 = 12$ cm located at $x_0 \approx -284$ and ≈ 253 μm.

Finally, we consider a scenario where two objects (metal wires of diameter $w = 0.5$ mm each) are located in *different* planes along the propagation axis. The first object is at a distance $d_1 = 7$ cm from the source and is displaced to a position $x_0 = 0.375$ mm from the optical axis, and the second object follows it at a further distance Δd along z and is displaced to a symmetrically opposite transverse position $-x_0$ [Fig. 3.1(e)]. Whereas the shadow cast by the first object (closest to the source) has mostly washed out, there is a remnant shadow from the second object (closest to the detection

plane); see $|G_{\mathrm{r}}(y_1, 0; d)|$ in Fig. 3.4(a). The measured complex $G_{\mathrm{r}}(y_1, y_2; d)$ [Fig. 3.4(a,b)] is back-propagated [Fig. 3.4(d)], and we extract the evolution of the intensity $I(y_1; z)$ along the propagation axis as before [Fig. 3.4(c)]. Over the course of the back-propagation, two localized 'shadows' emerge. First, a shadow of the object closest to the detection plane emerges at $d_1 = 40$ cm in the intensity profile. We do not observe a shadow of the second object at this plane. By continuing the back-propagation procedure, the first observed shadow starts to smear out while a second shadow associated with the object closest to the source emerges. From these calculations, we can estimate the size and locations of the two objects [Fig. 3.4(c)]. The errors in estimating the location of the objects from the detection plane are $\approx 14.8\%$ and $\approx -3.6\%$.

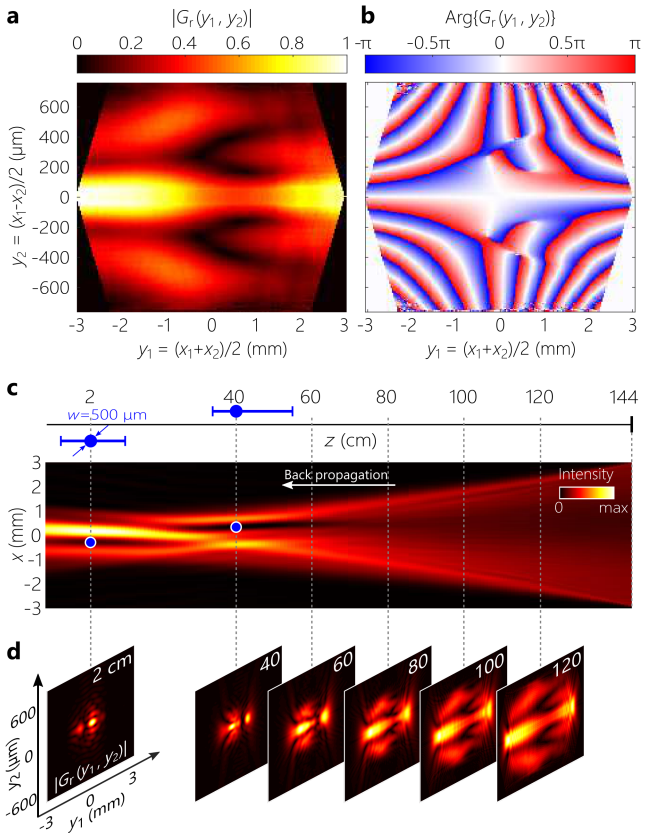

Figure 3.4: Same as in Fig. 3.2, except that the two-object scene in Fig. 3.1(e) is employed. The two identical objects have a diameter of 500 μm and are placed off the central axis in different axial planes. The object widths are estimated at ≈ 400 μm, $x_0 \approx -321$ μm for the object closest to the source and $x_0 \approx 309$ μm for the object closest to the detector.

We now discuss some of the limitations of this approach. The back-propagation is exact only if the detector is of infinite size. The finite detector size leads to imperfections in reconstructing the scene; e.g., a finite resolution for distinguishing objects located at neighboring transverse or longitudinal positions. The results in Fig. 3.2 identify a limitation of this approach, namely that the region immediately behind the object (which is occluded from the perspective of the detector) represents a 'null space' for the procedure: a small object placed in the immediate vicinity behind

the object will be difficult to observe. In general, when an object obstructs the light path, some information from the preceding planes is lost. For example, if two objects are placed in two different planes, the object closer to the detector will occlude the farther object. Increasing the size of the detection plane helps alleviate these limitations. Finally, strictly speaking, the back-propagation procedure described above does not necessitate knowledge of the source for a successful reconstruction of the scene. We carried out a reference measurement for calibration only. An accurate measurement of $G_{\mathrm{r}}(y_1, y_2)$ suffices for the back-propagation procedure.

3.3 Determining Object Parameters Using Generalized Sources

3.3.1 A Minimum Residual Approach to the Inverse Problem

Using a set of measured coherence samples, we seek to determine the breakpoints $\mathbf{a} = (a_1, \cdots, a_N)$ of a generalized source, as well as the distance d between the source and the measurement plane. For a Gauss-Schell source, truncation of the transmission function away from the mean (e.g., at $|y_1'| = 3w$) is insignificant to the approximation, allowing us to set $T_{1,1} = T_{N+1,N+1} = 0$.

For a trial vector $\mathbf{a} = (a_1, \cdots, a_N)$ and some $d > 0$, we consider the residual between the measured coherence G_d and the approximation $\overline{G}_d$ calculated using (2.21):

$$f(y_1, y_2; \mathbf{a}, d) = \overline{G}_d(y_1, y_2; \mathbf{a}, d) - G_d(y_1, y_2) \tag{3.5}$$

for each pair of measurements (y_1, y_2). More precisely, given the sample points (y_1^k, y_2^k), $k = 1, \ldots, M$, we introduce the objective function

$$F(\mathbf{a}, d) = \frac{1}{M} \sum_{k=1}^{M} |f(y_1^k, y_2^k; \mathbf{a}, d)|^2. \tag{3.6}$$

We consider the problem of minimizing F with respect to the parameters $\mathbf{a}, d$, using a gradient-descent algorithm [106]. The fixed-size steps are described by

$$\mathbf{a}^{(n+1)} = \mathbf{a}^{(n)} - \mu_{\mathbf{a}} \, \frac{\partial F}{\partial \mathbf{a}}, \tag{3.7}$$

$$d^{(n+1)} = d^{(n)} - \mu_d \, \frac{\partial F}{\partial d}, \tag{3.8}$$

where n is the gradient-descent iteration number. The derivation of the analytic gradients used by the algorithm are detailed in Appendix B. Of novelty here, when a local minimum has been found, i.e., when the partial derivatives $\frac{\partial F}{\partial \mathbf{a}}, \frac{\partial F}{\partial d}$ both fall below prescribed thresholds $\tau_{\mathbf{a}}, \tau_d$, the algorithm performs an additional check for a global minimum. This is accomplished by verifying that the residual is insignificant at *each sample point*, specifically

$$|f(y_1^k, y_2^k)| < \epsilon, \quad 1 \le k \le M. \tag{3.9}$$

As will be seen in Fig. 3.6(b) of the first example, a characteristic of the global minimizer is that the actual and estimated coherence functions closely match at all sample points, and thus the residual is small at each point. If condition (3.9) is not met, then the algorithm is randomly re-initialized with a starting point in the admissible domain.

The partial derivatives of F with respect to the breakpoints admit an analytic closed form as follows

$$\begin{aligned} \frac{\partial F}{\partial a_j} =& \sqrt{\frac{2}{\pi}} \frac{\widetilde{A}\widetilde{\sigma}}{\eta^3 \ell^2 M} \left(T_{j,j} - T_{j+1,j+1}\right) \\ & \times \sum_{k=1}^{M} \Big\{ \mathbb{R}\mathrm{e}\big[f(y_1^k, y_2^k)\big] \, \mathbb{R}\mathrm{e}\big[\Psi_j(y_1^k, y_2^k)\big] \\ & - \mathbb{I}\mathrm{m}\big[f(y_1^k, y_2^k)\big] \, \mathbb{I}\mathrm{m}\big[\Psi_j(y_1^k, y_2^k)\big] \Big\}, \end{aligned} \tag{3.10}$$

where

$$\Psi_j(y_1, y_2) = Z_j(y_1, y_2) \exp\left\{ iy_2 b_j(y_1) - iy_1 y_2 / \widetilde{R}^2 \right\}, \tag{3.11a}$$

$$Z_j(y_1, y_2) = N^{\widetilde{w}}(y_1) N^{\frac{\ell^2 \eta}{\sigma}}(y_2) N^{\eta/\widetilde{\sigma}}(b_j(y_1)); \tag{3.11b}$$

see Appendix B.

The derivative can also be calculated for measurements of the degree of spatial coherence $g_d(y_1, y_2) = G_d(y_1, y_2)/\sqrt{I_1 I_2}$, where $I_1 = G_d(y_1 + y_2, 0)$ and $I_2 = G_d(y_1 - y_2, 0)$ are the intensities at the first and second correlation points. The approximated degree of coherence is likewise defined as $\overline{g}_d(y_1, y_2) = \overline{G}_d(y_1, y_2)/\sqrt{\overline{I}_1 \overline{I}_2}$, where $\overline{I}_1, \overline{I}_2$ are the corresponding approximated intensities calculated using (2.21). We will denote the complex conjugate of $\overline{g}_d$ by $\overline{g}_d^*$. In this case, (3.10) still holds with transformations $f \to \widetilde{f}$ and $\Psi_j \to \widetilde{\Psi}_j$ where

$$\widetilde{f}(y_1, y_2; \mathbf{a}, d) = \overline{g}_d(y_1, y_2; \mathbf{a}, d) - g_d(y_1, y_2), \tag{3.12a}$$

$$\begin{aligned} \widetilde{\Psi}_j(y_1, y_2) = &\frac{1}{\sqrt{\overline{I}_1 \overline{I}_2}} \left\{ \Psi_j(y_1, y_2) - \overline{g}_d^*(y_1, y_2) \right. \\ &\left. \times \left[\overline{I}_1 Z_j(y_1 - y_2, 0) + \overline{I}_2 Z_j(y_1 + y_2, 0) \right] \right\}. \end{aligned} \tag{3.12b}$$

The derivative with respect to the distance is calculated by a finite difference.

3.3.2 Applications with Simulated Data

3.3.2.1 Single Object at Known Distance

Consider a Gauss-Schell source at $z = 0$ propagating a distance d_0 in free space, where it is blocked by a single object of width $2l$ centered along the transverse axis at the offset point $x = x_0$ as shown

in Fig. 3.5. The detector is located at a distance d from the object plane. In this first example we seek to estimate the parameters x_0 and l, assuming that the distances d_0 and d are known.

The parameters for the original Gaussian source (at $z = 0$) are amplitude $A = 1$, width $w \approx 1.7$ mm (yielding an intensity full width at half-maximum (FWHM) of 4 mm), and variance $\sigma \approx 8.5$ μm (yielding a coherence FWHM of 20 μm). Also we assume the source has no phase (i.e., in the limit as $R \to \infty$). The wavelength is $\lambda = 633$ nm.

In the forward model, the parameters $\tilde{A}$, $\tilde{R}$, $\tilde{w}$, and $\tilde{\sigma}$ in the plane of the object are calculated using the transformations in (2.15). The object is modeled using (2.3) with $N = 2$, and the breakpoints $a_1 = x_0 - l$, and $a_2 = x_0 + l$, and the coherence is propagated from the object plane to the detector plane using (2.6) to obtain the coherence measurements. In solving the inverse problem, the estimated coherence is calculated by (2.21).

The initial offset location parameter x_0 is set to uniformly span an admissible domain, whose bounds (± 7.1mm) are dependent on the width of the source Gaussian. The initial length l is assigned between 0 and 2 mm at random. The other parameters are fixed, $\mu_{\mathbf{a}} = 10^{-4}$, $\tau_{\mathbf{a}} = 10^{-2}$, and $\epsilon = 2 \times 10^{-3}$.

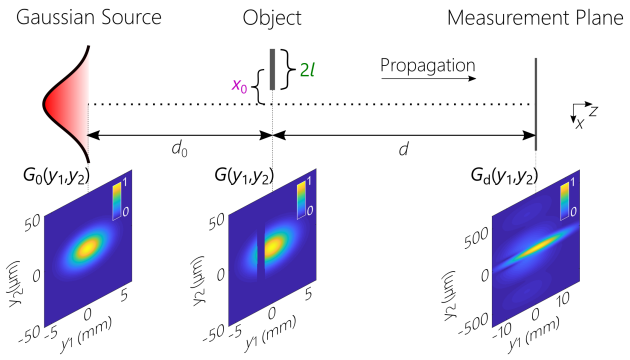

Figure 3.5: A single object scene with $x_0 = -1.5$ mm, $l = 0.5$ mm, $d_0 = 10$ cm, and $d = 100$ cm. The normalized magnitude of the coherence function is shown at the bottom of the diagram in three planes: in the plane of the Gaussian source, immediately after interacting with the object (i.e. at the secondary source), and at the measurement plane.

The results of one execution of the gradient-descent algorithm are shown in Fig. 3.6. The actual parameter values are $x_0 = -1.5$ mm, $l = 500$ μm, and $d = 1$ m. The modulus of the actual simulated coherence function is shown in Fig. 3.6(a), with the sample points marked. The measured coherence function at the 10 sample points is shown in Fig. 3.6(b) along with the final estimate [calculated using (2.21)]. The dynamics (with iterations) are displayed in Fig. 3.6(c). The parameter estimates are shown in the top two plots, with the actual value indicated by horizontal dashed lines. The maximum residue, defined as $\max\{f\} := \max_{y_2} f(0, y_2)$ is shown in the bottom plot with the threshold ϵ indicated by a horizontal dashed line. Vertical dotted lines indicate where a new initialization point is chosen and the algorithm restarted. This restart can be triggered when the partial derivatives fall below the threshold $\tau_{\mathbf{a}}$ while $\max\{f\} > \epsilon$, indicating that the local minimum is not a global minimum. The restart may also be triggered when the parameters leave the admissible domains. In the final iterations, it can be seen that the parameter estimates converge to the correct values and $\max\{f\}$ falls below the threshold. The small residue is evidenced by the

excellent agreement between the measured and estimated coherence functions in Fig. 3.6(b). The estimates are $x_0 = -1.504$ mm and $l = 497.2$ μm, which have an error of less than 1% (an error which could be made arbitrarily small by reducing the value of $\tau_{\mathbf{a}}$).

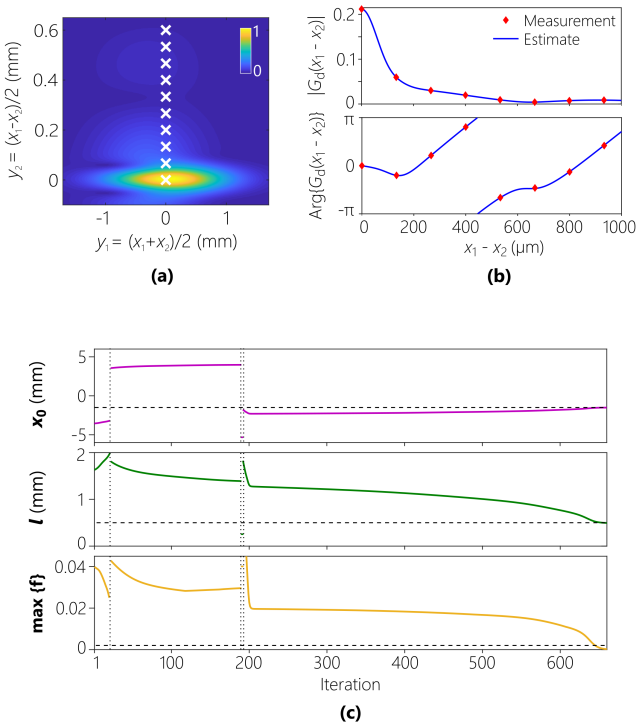

Figure 3.6: Reconstruction results for one object at known distance. (a) Normalized modulus of coherence function in the measurement plane with sample points marked. (b) Modulus and phase of coherence function at measurement plane. Both measured samples and final estimate are shown. (c) Path of the gradient descent algorithm. The top two plots show the estimates of the two parameters, with horizontal dashed lines indicating the actual value of the parameters. The bottom plot shows the maximum residual value among all sample points with the threshold ϵ indicated by a dashed line. A vertical dotted line indicates a restart of the algorithm with a new initialization.

3.3.2.2 *Single Object at Unknown Distance*

We now expand on the previous example by estimating a third parameter, the distance d between the object and measurement plane. The partial derivative of the residual F with respect to distance is calculated by a finite difference, with $\tau_d = 10^{-3}$. When a new initialization point is generated, the distance d is randomly assigned from an admissible domain between 0.5 m and 1.5 m. The results of the algorithm using simulated measurements are shown in Fig. 3.7.

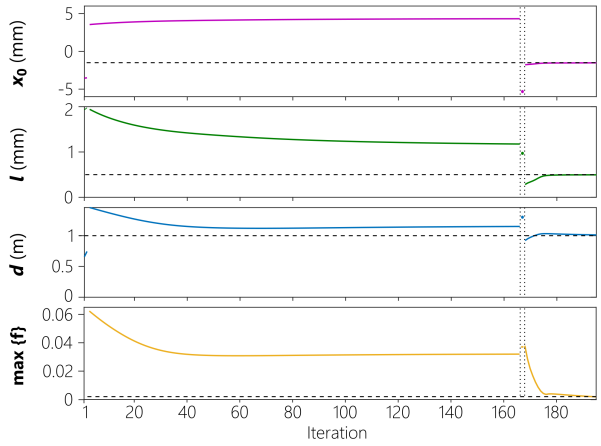

Figure 3.7: Gradient descent algorithm estimating three object parameters: x_0, l, and d. The configuration and sample points are the same as in Fig. 3.6. The plot labels are the same as those defined in Fig. 3.6(c), with an additional plot included for parameter d.

The actual parameters are the same as in the previous section, and the estimated values are $x_0 = -1.521$ mm, $l = 496.0$ μm, and $d = 1.013$ m. As with the two-parameter example, the estimate is close with a maximum parameter error of less than 1.5% (and could be reduced by using smaller gradient thresholds).

3.3.2.3 Two Intercepting Objects

We now demonstrate the ability of the algorithm to handle more complicated scenes with more parameters. Fig. 3.8 shows the results for a five-parameter estimation problem in which two objects are located in the same plane. The parameters are the center x_0^A and half-width l^A of the first object defined by breakpoints a_1 and a_2, the center and half-width parameters for the second object (x_0^B and l^B) defined by breakpoints a_3 and a_4, and the distance d between the object and measurement planes. The algorithm parameters $\mu_{\mathbf{a}}$, $\tau_{\mathbf{a}}$, ϵ, and τ_d are the same as in Sections 3.3.2.1 and 3.3.2.2, and we use the same approach as with the one object example, only with two additional breakpoints. The coherence function and sample points are shown in Fig. 3.8(b). The iterations are shown in Fig. 3.8(c).

The maximum error in parameter estimates is less than 1.2%; very small considering that only 10 sample points were used along the coherence axis.

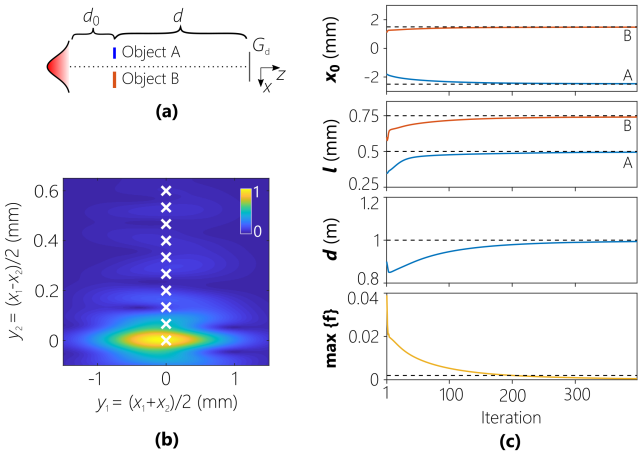

Figure 3.8: Example showing estimation of positions of two objects in the same axial plane. (a) Diagram of scenario. (b) Normalized modulus of coherence function in the measurement plane with sample points marked. (c) Path of the gradient descent algorithm. The top three plots show the estimates of the five parameters (blue lines correspond to Object A and orange lines to Object B), with dashed lines indicating the actual value of the parameters. The bottom plot shows the maximum residual value among all sample points with the threshold ϵ indicated by a dashed line. The Gaussian source parameters are the same as in the one object example. The object parameters are $x_0^A = -2.5$ mm, $l^A = 500$ μm for Object A, $x_0^B = 1.5$ mm and $l^B = 750$ μm for Object B. The two objects are located in the same plane, and the actual distances are $d_0 = 0.1$ m, $d = 1$ m. The final estimates are $x_0^A = -2.483$ mm, $l^A = 495.6$ μm, $x_0^B = 1.492$ mm, $l^B = 741.3$ μm, and $d = 0.944$ m.

While in the previous examples we have assumed the number of objects is known, it is also possible to use the algorithm when all we have is a crude upper bound on the number of objects. Additional breakpoints can be included in the transmission function, and the "missing" objects will be estimated as having zero width. To illustrate this point, we repeat the previous example of Fig. 3.8, but with Object B removed. The results are shown in Fig. 3.9. The parameters of Object

A are correctly estimated, whereas because the second assumed object is not actually present, the estimated width of Object B rapidly approaches zero.

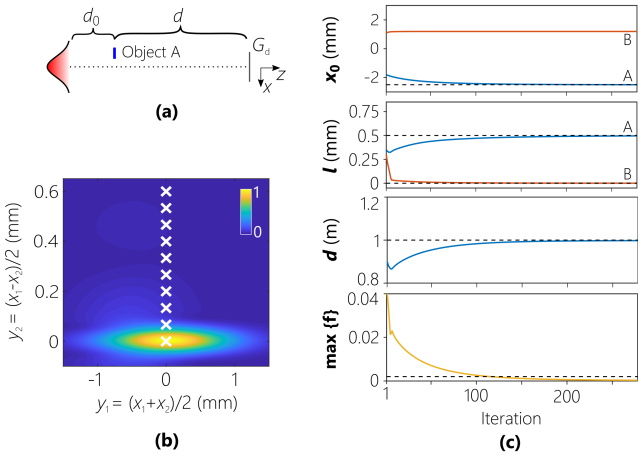

Figure 3.9: Example showing estimation of positions assuming two objects in the same axial plane when only one object is actually present. Panels (a)-(c), as well as the source parameters, are the same as in Fig. 3.8. The parameters for Object A are $x_0^A = -2.5$ mm, $l^A = 500$ μm, and Object B is absent from the scene. The actual distances are $d_0 = 0.1$ m, $d = 1$ m. The final estimates are $x_0^A = -2.494$ mm, $l^A = 495.5$ μm, $x_0^B = 1.198$ mm, $l^B = 0.45$ μm, and $d = 0.998$ m. Note that the estimate of $l^B \approx 0$, indicating no Object B is present (thus rendering the estimate of x_0^B irrelevant).

Fig. 3.10 shows the results diagram for a similar problem in which there are two objects, but this time located in two planes at different axial positions with respect to the source. Thus, the number of estimated parameters increases to six, with the distances to object A and B being designated d^A and d^B, respectively. While the scenarios may be similar, the implementation of multiple object planes is more complicated than that of a single plane, requiring multiple generalized sources located in different planes. In this case, the objects are sufficiently separated transversely that we can treat the resulting coherence function as the superposition of the individual coherence

functions [104], each source having the same form as in the one-object example. Specifically, the resulting coherence function $\breve{G}_d$ is calculated as

$$\breve{G}_d(y_1, y_2) = G^-(y_1, y_2) - \overline{G}_d^A(y_1, y_2) - \overline{G}_d^B(y_1, y_2), \tag{3.13}$$

where G^- is calculated from (2.2) with distance $d = d_0 + d^A$, and $\overline{G}_d^A$ and $\overline{G}_d^B$ are "inverted" coherences due to objects A and B, respectively. The inverted coherences are calculated using transmission function $1 - T_{j,j}$ in place of $T_{j,j}$ in (2.21). Due to the independence of the two generalized sources located at A and B, (3.10) can be applied to each without modification. As shown in Fig. 3.10(b), the number of sample points has been increased to include off-axis measurements, i.e. including points with $y_1 \neq 0$, to aid in estimation of the two distances.

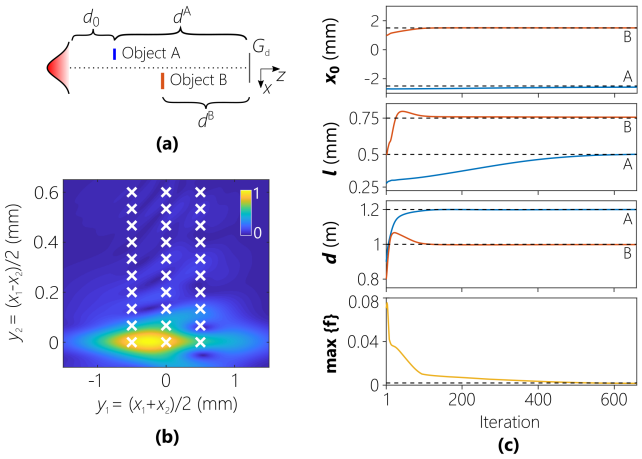

Figure 3.10: Example showing estimation of positions of two objects in different axial planes. Panels (a)-(c) are the same as in Fig. 3.8. The Gaussian source and object parameters are also the same as used in Fig. 3.8. The distances are $d_0 = 0.1$ m, $d^A = 1.2$ m, and $d^B = 1$ m. The final estimates are $x_0^A = -2.516$ mm, $l^A = 501.1$ μm, $x_0^B = 1.508$ mm, $l^B = 755.7$ μm, $d^A = 1.20$ m, and $d^B = 0.998$ m.

As with the five-parameter example, the maximum parameter estimate error is less than 1.2%.

3.3.3 Object Recovery from Experimental Data

In this section, we present results obtained by applying the algorithm to actual experimental measurements from [2]. The setup is diagrammed in Fig. 3.11(a). The source in the experimental setup is a Thorlabs M625L3 LED (with a peak wavelength of ≈ 633 nm and FWHM-bandwidth of ≈ 18 nm), with a band-pass filter centered at 632.8 nm and having a bandwidth of ≈ 1.3-nm FWHM. The object is a 500 μm wire placed at various transverse positions. The coherence is measured via double slit interferometry by a Digital Micromirror Device (TI DLP6500), a CCD camera (The ImagingSource, DFK 31BU03), and a set of three lenses (for magnification and to obtain a Fourier transform).

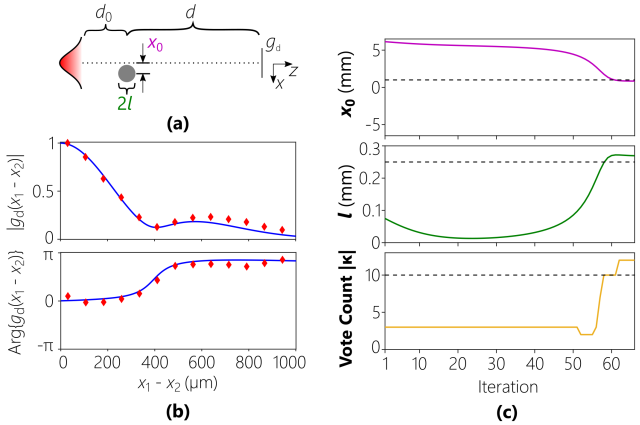

Figure 3.11: Results of gradient descent algorithm using experimental data. (a) Diagram of setup. (b) Modulus and phase of coherence function at measurement plane. Both measured samples and final estimate are shown. (c) Path of the gradient descent algorithm. The top two plots show the estimates of the two parameters, with dashed lines indicating the actual value of the parameters. The bottom plot shows the cardinality of the "vote" set $|\kappa|$ at each iteration, with the threshold p indicated by a dashed line.

The parameters used for the analytic model are as follows. The source parameters are $A = 1$, intensity FWHM of 1 mm, coherence FWHM of 75 μm, and no phase, and the wavelength $\lambda = 633$ nm. The actual object half-width is $l = 0.25$ mm, with varying center x_0, and the actual distances are $d_0 = 5$ mm, $d = 1.245$ m.

In order to accommodate noise and mismatches in the model, we relax the stopping condition to use a voting mechanism based on the set

$$\kappa = \left\{ k \;\middle|\; |f(y_1^k, y_2^k)| < \epsilon,\ 1 \le k \le M \right\}. \tag{3.14}$$

Specifically, rather than requiring that the residual be small for all samples, here the residual only

needs to be small for a subset of the samples. Additionally, to ensure that individual errors are not excessively large, an additional threshold is placed on F. Accordingly, we replace the condition in (3.9) with condition

$$|\kappa| \geq p \text{ and } F < \gamma \tag{3.15}$$

where set cardinality is denoted by $|\cdot|$. In this example, the algorithm parameters are set to $\mu_{\mathbf{a}} = 5 \times 10^{-7}$, $\tau_{\mathbf{a}} = 1$, $\epsilon = 0.15$, $p = 55$, and $\gamma = 1$.

The resulting estimates of the algorithm generated for several experimental setups are shown in Table 3.1. The final initialization value is also listed to demonstrate that the algorithm converges given diverse initialization conditions. To show the low sampling requirements of the proposed algorithm, only 13 of the measured data points are used for estimation. The detailed gradient descent results for $x_0 = 100$ μm are shown in Fig. 3.11. The measured and estimated coherences are shown in Fig. 3.11(a). The errors are due to noise in the measurements and inaccurate assumptions in modeling the source as a Gauss-Schell source. The gradient descent dynamics are shown in Fig. 3.11(b). Rather than showing all initializations, as was done in Section 3.3.2.1, only the final initialization is shown (i.e., the successful initialization which converges to the global minimum). As seen in the bottom plot of Fig. 3.11(b), only when the parameters approach the actual values does the residue become small, and we have $|\kappa| \geq p$.

Table 3.1: Experimental results. For each parameter, the actual value, initial starting point, and final estimate are shown.

Center x_0 (μm)			Width $2l$ (μm)		
Actual	Initial	Est.	**Actual**	Initial	Est.
-100	-409.2	-114.7	**500**	137.6	479.7
-50	-409.2	-36.1	**500**	137.6	555.9
0	409.2	5.6	**500**	299.7	610.3
50	-306.9	57.3	**500**	58.4	583.7
100	613.9	84.5	**500**	75.0	540.7

Note that while the hypotheses in (2.18) are satisfied in Section 3.3.2, these conditions are merely sufficient for (2.21) to hold. This is demonstrated here, in Section 3.3.3, where the experimental parameters violate the first inequality of (2.17), yet the approximation is still dependable and allows for successful inversion.

3.3.4 Ill-posedness of Inversion When Using Intensity Measurements Only

With the tools developed in this chapter, we can now return to a comparison of intensity measurements versus coherence measuerments in lensless LOS situations. The coherence measurements bring in an additional dimension to the data, which allows for devising a global inversion method. More precisely, the local method of steepest descent is applied to a family of residuals, all of which have a common unique minimizer. This idea is stressed in the example in Fig. 3.12, where the residuals are calculated for a family of functions (parameterized along the vertical axes), by using the sample points along the horizontal axis. The global minimum is the unique point at which

all these functions are zero.

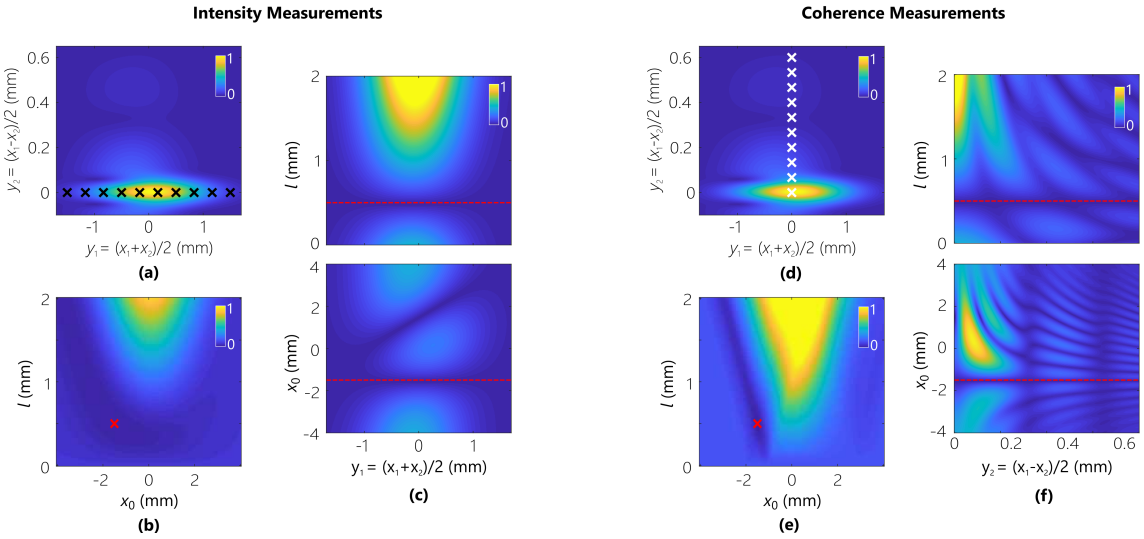

Figure 3.12: Comparison of intensity and coherence measurements. The modulus of the simulated coherence function is shown in (a) and (d) with intensity sample points indicated by black "x" marks and coherence sample points indicated indicated by white "x" marks. The corresponding residual maps $F(x_0, l)$ for the two scenarios are shown in (b) and (e). For comparison purposes, the functions are normalized against $\frac{1}{M}\sum_{k=1}^{M}|G_d(y_1^k, y_2^k)|^2$, and plotted on the same scale. As can be seen in this example, the residual map for intensity measurements exhibits a larger area of minima than that of the coherence measurements. This may lead to more ambiguity in the reconstruction, although results will vary depending on physical factors such as the signal-to-noise ratio of the measurements. (c) and (e) show the residual f plot as a function of the sample point (along the horizontal) and parameter (vertical). Each plot shows variation with regard to one parameter while the other is fixed at the correct value, and all plots use the same scale. The actual parameter values are indicated in red. The parameters are the same as used in Fig. 3.6.

CHAPTER 4: FORWARD PROBLEM FOR THE SCATTERING SURFACE

4.1 Introduction

In this chapter[1], we consider the forward model of the scattering wall. Our model is based on recent studies, which differentiate two fundamental types of scattering: volume scattering and surface scattering [3, 51].

Some inversion techniques counteract volume scattering by using wavefront shaping coupled with knowledge of the transfer matrix of the scatterer [107]. For example, light can be focused through the scatterer to form a point [108] or an image [109, 110].

The problem of concern here assumes surface scattering is stronger than volumetric scattering. This setting occurs with a wall at large angles of incidence. In this case, the coherence function tends to be transmitted with less disruption along the axis perpendicular to the scattering plane [51]. In ideal cases, this may allow images to be formed from the reflection with a normal lensed camera (recent work even suggests this phenomenon accounts for mirages previously attributed to air temperature differentials [111]). Here, we consider the less ideal case, where a useful image cannot be formed using a regular camera, but information is still retained in the spatial coherence of the reflected light. To best capture the surface-scattered light, it is assumed that the angle between the source and wall is equal to the angle between the imaging device and the wall.

[1] In this chapter, we partially use the material published in Imaging and Applied Optics, 2018 [14], and IEEE Transactions on Image Processing, 2019 [6].

4.2 Forward Propagation to the Wall

In this section, we review the physical model for forward propagation described in Chapter 2. Additional details regarding the models, including experimental verification, can be found in [51].

Suppose that we have a quasi-homogeneous source as described in Section 2.2, with

$$G(\mathbf{r}, \boldsymbol{\rho}) = I(\mathbf{r}) \exp\left(-\frac{\| \boldsymbol{\rho} \|_2^2}{2\sigma^2}\right), \tag{4.1}$$

where $I(\mathbf{r})$ is the 2D intensity in the source plane, and σ is the coherence width.

Recall that under the Fresnel approximation, since the impulse response function for the electric field in free space is

$$h(\mathbf{r}) = i\frac{\exp(-ikd)}{\lambda d} \exp\left[-\frac{ik\| \mathbf{r} \|_2^2}{2d}\right], \tag{4.2}$$

then, the propagation is given by

$$\begin{aligned} G_d(\mathbf{r}_1, \mathbf{r}_2) &= \frac{1}{(\lambda d)^2} \iint_{\mathbb{R}^2 \times \mathbb{R}^2} d^2\mathbf{r}_1' \, d^2\mathbf{r}_2' \, G(\mathbf{r}_1', \mathbf{r}_2') \\ &\quad \times h(\mathbf{r}_1' - \mathbf{r}_1) \, h^*(\mathbf{r}_2' - \mathbf{r}_2) \\ &= \frac{1}{(\lambda d)^2} \iint_{\mathbb{R}^2 \times \mathbb{R}^2} d^2\mathbf{r}_1' \, d^2\mathbf{r}_2' \, G(\mathbf{r}_1', \mathbf{r}_2') \\ &\quad \times \exp\left[\frac{ik}{d}\left(\| \mathbf{r}_1 - \mathbf{r}_1' \|_2^2 - \| \mathbf{r}_2 - \mathbf{r}_2' \|_2^2\right)\right]. \end{aligned} \tag{4.3}$$

Applying the "rotation" described in Section 1.2, the coherence of the light after propagating distance d is

$$G_d(\mathbf{r}, \boldsymbol{\rho}) = \frac{1}{(\lambda d)^2} \iint_{\mathbb{R}^2 \times \mathbb{R}^2} d^2\mathbf{r}' \, d^2\boldsymbol{\rho}' \, G(\mathbf{r}', \boldsymbol{\rho}') \exp\left[\frac{ik}{d}(\mathbf{r} - \mathbf{r}') \cdot (\boldsymbol{\rho} - \boldsymbol{\rho}')\right]. \tag{4.4}$$

After substituting (4.1) into (4.4), and rearranging the integrals, we have

$$G_d(\mathbf{r},\boldsymbol{\rho}) = \frac{\exp\left(\frac{ik}{d}\mathbf{r}\cdot\boldsymbol{\rho}\right)}{(\lambda d)^2}\int_{\mathbb{R}^2} d^2\mathbf{r}'\,\exp\left(-\frac{ik}{d}\boldsymbol{\rho}\cdot\mathbf{r}'\right) I(\mathbf{r}') \\ \times\int_{\mathbb{R}^2} d^2\boldsymbol{\rho}'\,\exp\left(-\frac{ik}{d}(\mathbf{r}-\mathbf{r}')\cdot\boldsymbol{\rho}'\right)\exp\left(-\frac{\|\,\boldsymbol{\rho}'\,\|_2^2}{2\sigma^2}\right). \tag{4.5}$$

Evaluating the inner integral yields the linear transformation

$$G_d(\mathbf{r},\boldsymbol{\rho}) = C(\mathbf{r},\boldsymbol{\rho})\,\mathcal{F}\left\{H(\mathbf{r}-\mathbf{r}')I(\mathbf{r}')\right\}(k\boldsymbol{\rho}/d) \tag{4.6}$$

where

$$C(\mathbf{r},\boldsymbol{\rho}) = \frac{2\pi\sigma^2}{\lambda^2 d^2}\exp\left(\frac{ik}{d}\mathbf{r}\cdot\boldsymbol{\rho}\right), \tag{4.7}$$

$$H(\mathbf{r}) = \exp\left(-\frac{\sigma^2 k^2\|\,\mathbf{r}\,\|_2^2}{2d^2}\right), \tag{4.8}$$

λ is the wavelength, $k = 2\pi/\lambda$ is the wave number, and the Fourier transform is 2D with regard to the x and y components of $\mathbf{r}'$. The variable $\mathbf{r}'$ indicates spatial position in the object plane, whereas $\mathbf{r}$ indicates spatial position along the wall.

4.3 Wall Model

4.3.1 Specific Intensity

Because the wall scattering process will be described using a ray-based model, we need a link between coherence and the angular spread of the light (in this context referred to as specific intensity).

This link is provided by the relation [3, 112]

$$\hat{I}_d(\mathbf{r}, \mathbf{u}_\perp) = \left(\frac{k}{2\pi}\right)^2 |u_z| \int_{\mathbb{R}^2} d^2\boldsymbol{\rho}\, G_d(\mathbf{r}, \mathbf{u}) \exp(-ik\boldsymbol{\rho}\mathbf{u}_\perp). \tag{4.9}$$

where u_z is the z component of unit length vector $\mathbf{u} = (\mathbf{u}_\perp, u_z)$.

4.3.2 Understanding the Wall Model by Invoking Monte Carlo Simulations

In order to better understand the wall model, we perform numerical simulations using free space propagation to the wall, and then invoke the Monte Carlo simulator developed in [3]. A diagram of the end-to-end simulation is shown in Fig. 4.1.

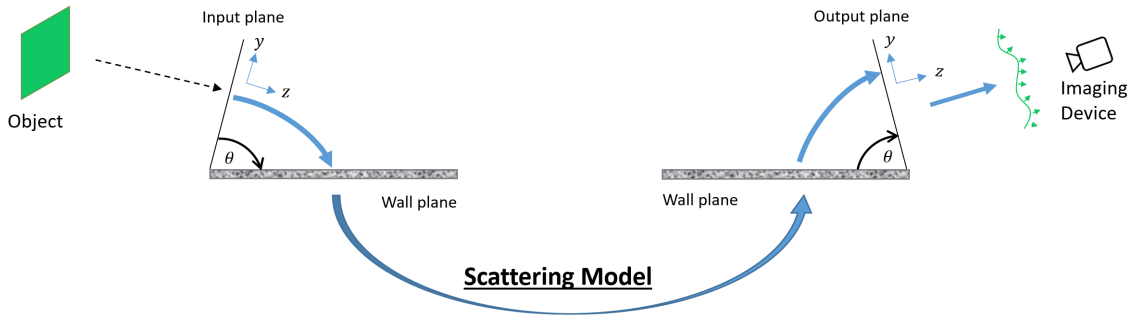

Figure 4.1: Full NLOS model including wall scattering.

A more detailed description of this process follows.

After the initial free space propagation, at the wall interface, we transform the coherence function to specific intensity and then perform a rotation (by angle θ) into the wall plane using the

transformation

$$\begin{bmatrix} \hat{u}_y \\ \hat{u}_z \\ \hat{u}_x \end{bmatrix} = \begin{bmatrix} 1 & 0 & 0 \\ 0 & \cos\theta & -\sin\theta \\ 0 & \sin\theta & \cos\theta \end{bmatrix} \begin{bmatrix} u_y \\ u_z \\ u_x \end{bmatrix}. \tag{4.10}$$

This rotation is illustrated in Fig. 4.2(a).

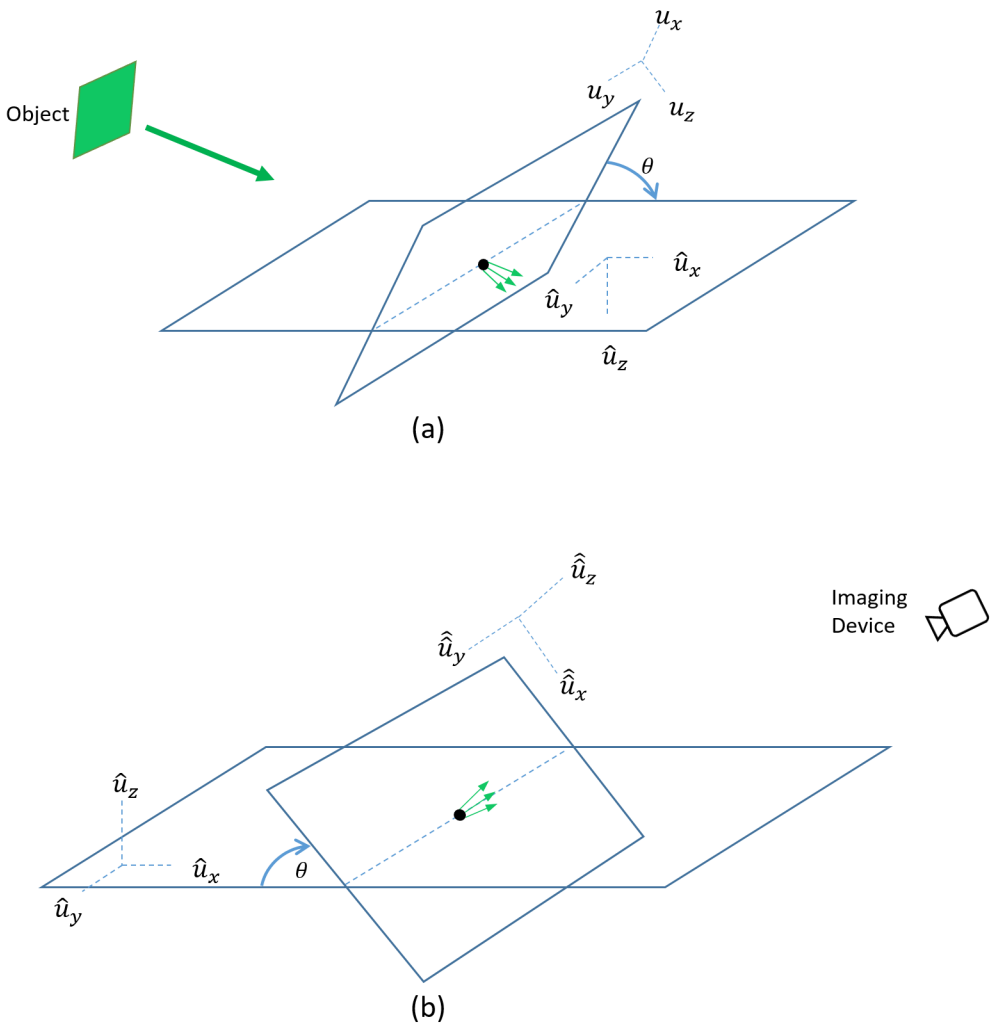

Figure 4.2: Rotations in the forward model at the wall interface.

For the purposes of studying the wall model, we only consider the coherence function at a single fixed center point $\mathbf{r}$. We note that we could equivalently convert the spatial coherence function to specific intensity at the source, and then perform the propagation to point $\mathbf{r}$ using phase-space methods [34]. See the Supplementary material of [51] for an example.

The specific intensity results after the rotation are fed into the Monte Carlo simulator to obtain the specific intensity reflected from the wall due to surface scattering. The resultant specific intensity is rotated into the output plane using the relation

$$\begin{bmatrix} \hat{\hat{u}}_y \\ \hat{\hat{u}}_z \\ \hat{\hat{u}}_x \end{bmatrix} = \begin{bmatrix} 1 & 0 & 0 \\ 0 & \cos\theta & \sin\theta \\ 0 & -\sin\theta & \cos\theta \end{bmatrix} \begin{bmatrix} \hat{u}_y \\ \hat{u}_z \\ \hat{u}_x \end{bmatrix} \tag{4.11}$$

and converted back into a spatial coherence function using the inverse of (4.9). The rotation to the output plane is illustrated in Fig. 4.2(b).

We make two assumptions regarding measurement of the scattered field. First, we assume that the spatial coherence function is imaged at the wall through a suitable measurement device. Second, we assume that the surface scattering can be isolated from the volume scattering during measurement by suitably restricting the field of view, as described in [51].

The results of the complete procedure are shown in Fig. 4.3 for $\theta = 80°$, and for square and circle mask shapes. These mask shapes are the same as those found in Section 2.5, and represent reflective objects. Results for other angles are shown in Fig. 4.4.

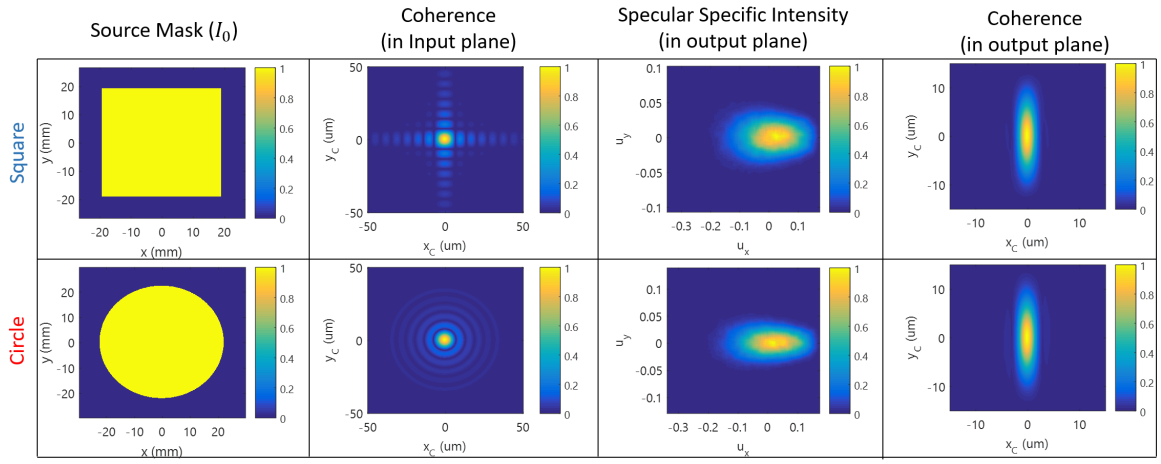

Figure 4.3: Results of forward scattering procedure using Monte Carlo simulations.

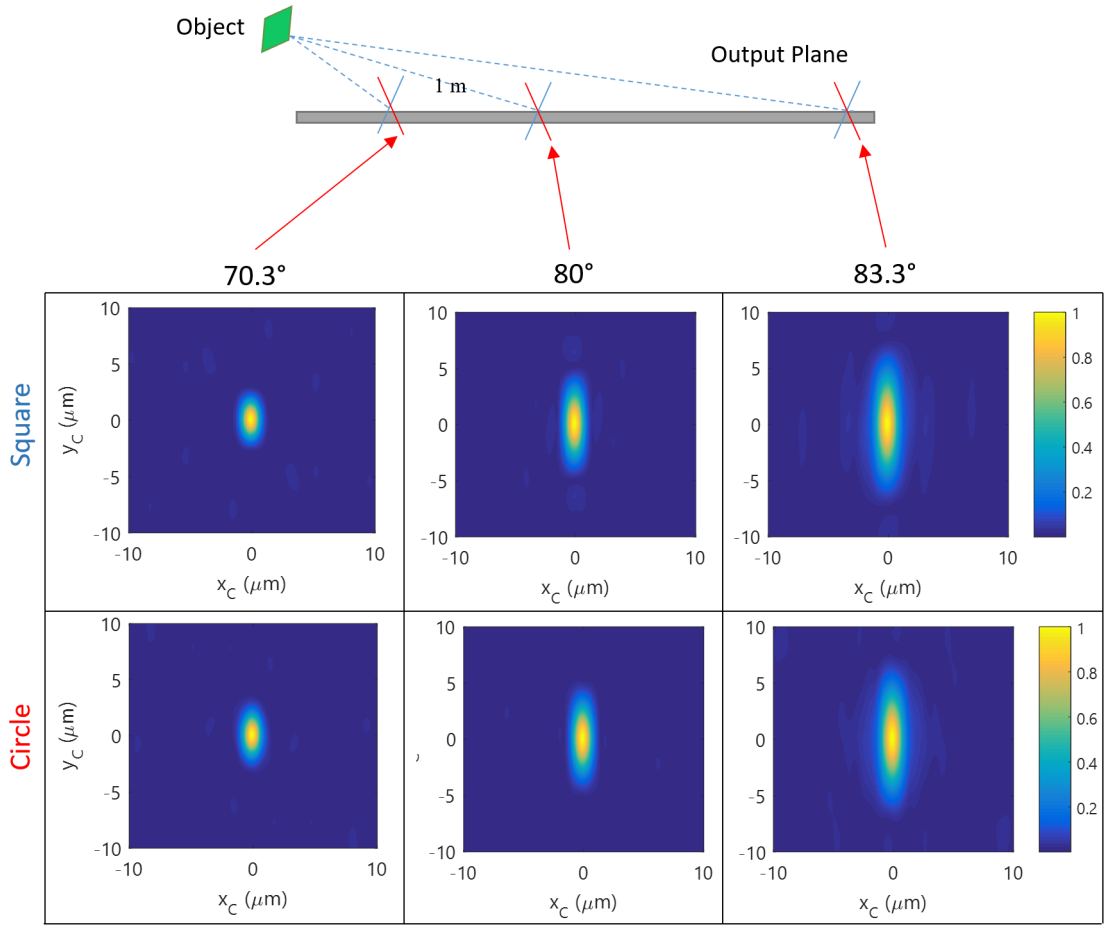

Figure 4.4: Examples of reflection at different angles θ in (4.10) and (4.11). The output of the wall is calculated using the Monte Carlo software described in [3].

While the Monte Carlo simulations help to understand surface scattering at the wall, we wish to have an analytic model for efficient solution of the inverse problem. The wall model can be simplified as shown in Fig. 4.5. Our original model is shown in Fig. 4.5(a). By "unfolding" the scene, we arrive at Fig. 4.5(b). The supplementary material of [51] explains that the model can be simplified as shown in Fig. 4.5(c), where the wall is represented by a Gaussian "apodizing" term. This term comes from the assumption that the surface scattering reflects any incoming ray

according to a Gaussian probability distribution [51].

4.4 Model

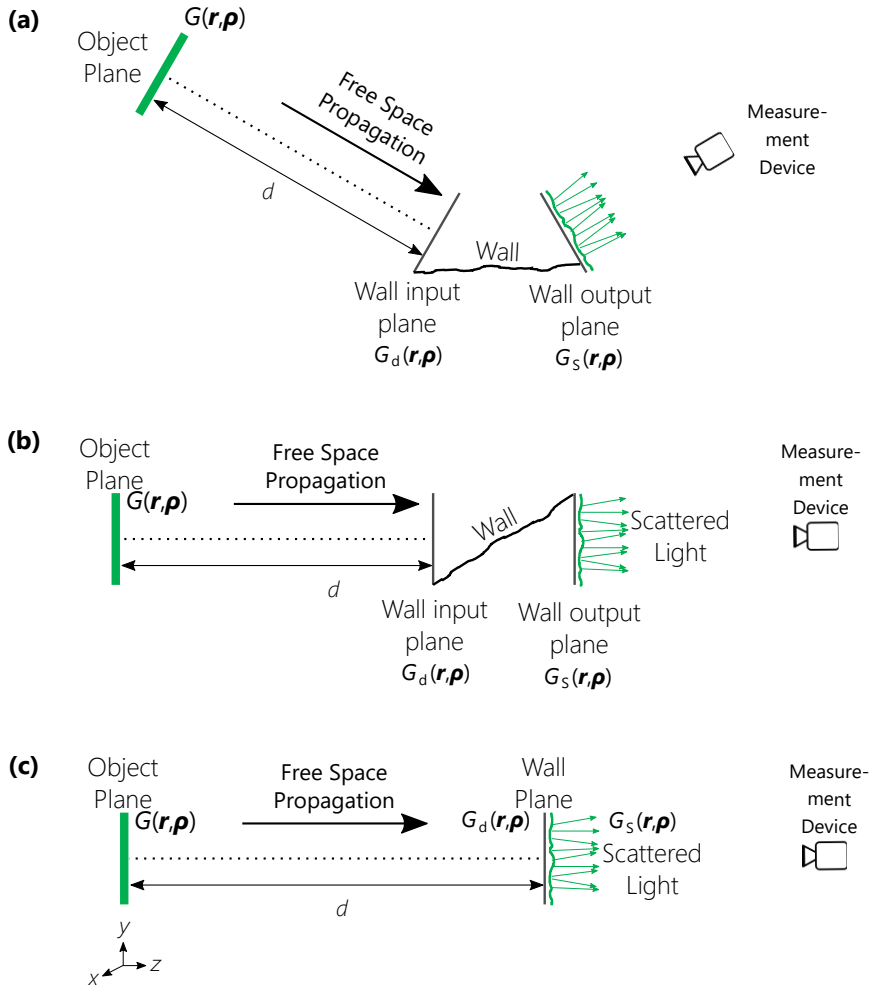

Figure 4.5: Unfolded scene

4.4.1 Analytic Model

We represent the transfer function of the wall as a Bidirectional Reflectance Distribution Function (BRDF) [113]

$$h(\mathbf{r}, \boldsymbol{\theta} - \boldsymbol{\theta}') = \exp\left(-\frac{(\theta_x - \theta'_x)^2}{2w_x^2} - \frac{(\theta_y - \theta'_y)^2}{2w_y^2}\right). \tag{4.12}$$

Here, $\boldsymbol{\theta} = (\theta_x, \theta_y)$ is the angle between the surface normal and the incident vector along the x and y axes, while $\boldsymbol{\theta}'$ is the reflected angle defined in a similar way.

For the interaction with the wall, the angular spread of photons can be assumed to be governed by a Gaussian function [3, 36]. The standard deviation of the angular spread along the x and y axes is $\mathbf{w} = (w_x, w_y)$. The geometry of the scene is such that the angles of incidence and reflection are fairly close, which results in a specular reflection due to surface scattering. Due to the paraxial nature of the incident waves, coupled with the narrow spread of the specular reflection [114], we can use the approximation

$$G_S(\mathbf{r}, \boldsymbol{\rho}) \approx S(\boldsymbol{\rho}) G_d(\mathbf{r}, \boldsymbol{\rho}) \tag{4.13}$$

where

$$S(\boldsymbol{\rho}) = w_x^2 w_y^2 \exp\left(-\frac{w_x^2 \rho_x^2}{2} - \frac{w_y^2 \rho_y^2}{2}\right), \tag{4.14}$$

and the intensity of the scattered field

$$I_S(\mathbf{r}) = \frac{2\pi\sigma^2}{\lambda^2 d^2} H(\mathbf{r}) \star I(\mathbf{r}), \tag{4.15}$$

where $\star$ is the 2D convolution operator.

Given that $\boldsymbol{\theta} - \boldsymbol{\theta}'$ is small due to the paraxial approximation and narrow spread of the specular reflection [114], then $\mathbf{u}_\perp - \mathbf{u}'_\perp \approx \boldsymbol{\theta} - \boldsymbol{\theta}'$ and we can can calculate the scattered *specific intensity* using the convolution

$$\hat{I}_S(\mathbf{r}, \mathbf{u}_\perp) \approx \int_{\mathbb{R}^2} d^2\mathbf{u}'_\perp \hat{I}_d(\mathbf{r}, \mathbf{u}'_\perp)\hat{h}(\mathbf{r}, \mathbf{u}_\perp - \mathbf{u}'_\perp) \tag{4.16}$$

Calculating the scattered *coherence* from (4.16) using the inverse of (4.9) yields (4.13). Substituting $\boldsymbol{\rho} = \mathbf{0}$ in (4.13) gives

$$I_d(\mathbf{r}) = \frac{2\pi\sigma^2}{\lambda^2 d^2} \int_{\mathbb{R}^2} d^2\mathbf{r}'\, I(\mathbf{r}') \exp\left(-\frac{\sigma^2 k^2 \| \mathbf{r} - \mathbf{r}' \|_2^2}{2d^2}\right), \tag{4.17}$$

and hence (4.15).

By using the Monte Carlo results, we fit the parameters of the analytic Gaussian apodizing factor for the 80 degree incident angle. Results are shown in Fig. 4.6.

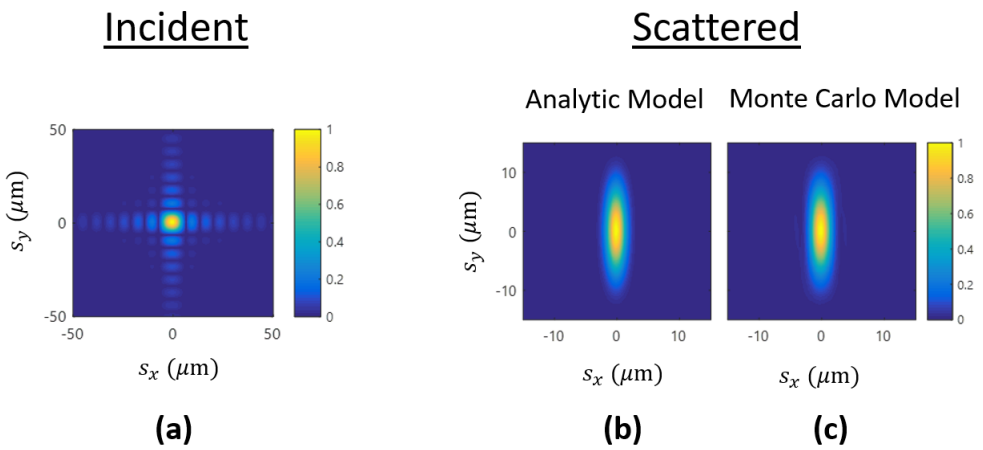

Figure 4.6: Monte Carlo simulation versus wall analytic model

We performed this same procedure for both a circle and a square shape of varying widths. As

shown in Fig. 4.7, both the coherence width and the zero crossings at the output vary as the shapes change size, suggesting that the inverse problem is well-posed. Experimental examples showing the retention of information in the spatial coherence function after scattering can be found in [51].

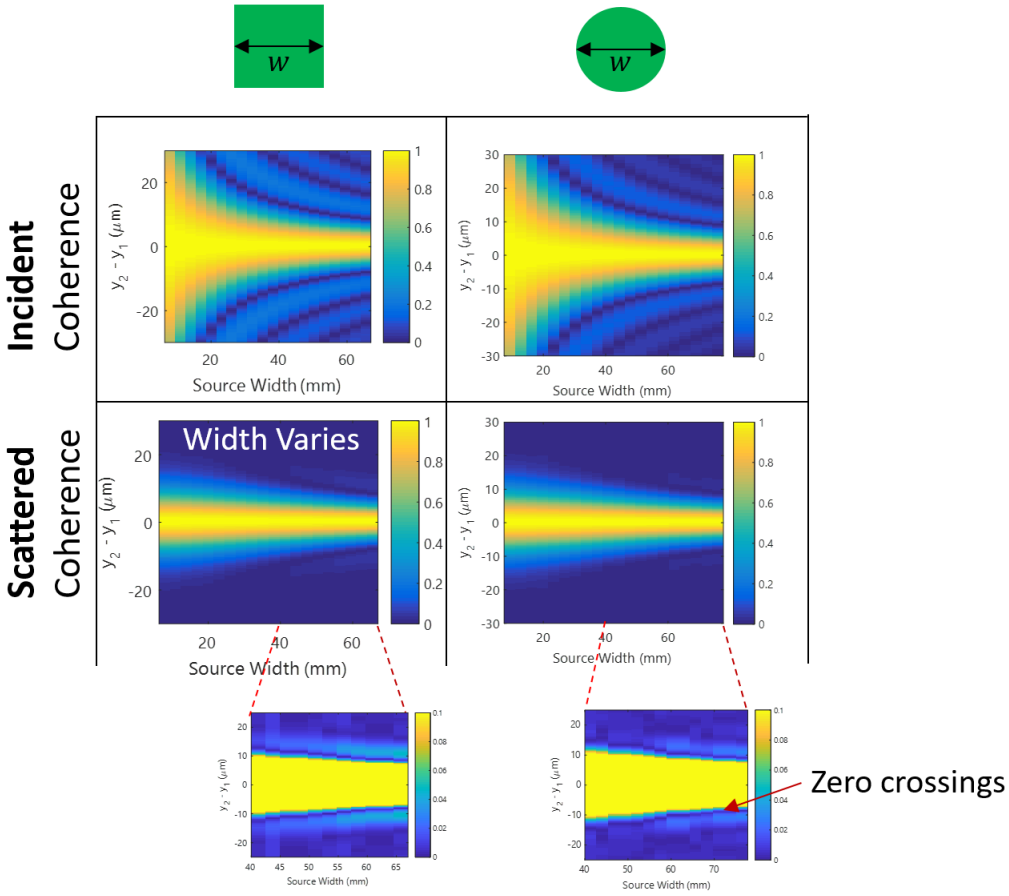

Figure 4.7: What information is retained in the scattered coherence function

CHAPTER 5: INVERSE PROBLEM FOR THE SCATTERING SURFACE

5.1 Introduction

In this chapter[1], we study two problems: the characterization of a small, simple object obscured by the wall, and the imaging of a larger object.

The shape classification and characterization problem exploits variations in the coherence width and zero crossings of the reflected spatial coherence function, as described in Chapter 4. Using the analytic wall model, we develop an optimization problem which explicitly characterizes the width of the object. We provide a means for classifying these simple shapes, and show that distance can also be incorporated into the optimization problem.

The imaging method demonstrates the ability to reconstruct discernible 2D projections of large obscured objects in NLOS settings. The approach works with targets in which the projection on the z-axis is much smaller compared to the (optical) distance d to the detector (a requirement which is met in many practical situations), thus reducing the problem to that of reconstructing a 2D image; see the illustration in Fig. 5.4(a). The proposed imaging method is based on a multi-modal data fusion. We formulate and study a convex optimization problem, and propose an algorithm for solving it based on the Alternating Direction Method of Multipliers (ADMM) [115]. The optimization problem incorporates regularization for sparsity, and reconstructs the image in a suitable transformed basis in which the source image is assumed to have a sparse representation.

In contrast with some existing fusion approaches, which merge multiple *images* in a spatial or wavelet domain [116–118], our method reconstructs a single image by fusing multiple *measure-*

[1]In this chapter, we partially use the material published in Imaging and Applied Optics, 2018 [14], and IEEE Transactions on Image Processing, 2019 [6].

ment types at different spatial scales while exploiting their respective propagation models. In spirit, our approach to fusion relates to that of [119], where a convex optimization problem is devised to pansharpen medical images.

We provide a means of assessing the null space of the model, and a weighting scheme and decision framework by which individual samples of a measurement may be excluded.

The simulated results demonstrate the concept of NLOS imaging using spatial coherence. We further give examples of fusion, and show how the null space of the measurement transformations can be analyzed.

5.2 Shape Classification

We consider a 50.3 mm square shape. The measured coherence function at the output of the wall is calculated using the forward model with the Monte Carlo simulator of [3] (we use this simulator in the forward model to avoid an inverse crime). By using the analytic wall model, we calculate the measured coherence function for "candidate" squares and circles. The two candidate circles are shown in Fig. 5.1(b). One has a similar coherence function (in terms of residual) but has a very different zero crossing, as shown in Fig. 5.1(a). The other circle candidate has a close match in the zero crossing, but a large residual (not shown). For these reasons, we can disqualify both candidates. On the other hand, the square has a close match in terms of both residual and zero crossing, suggesting (correctly) that this is the actual source shape.

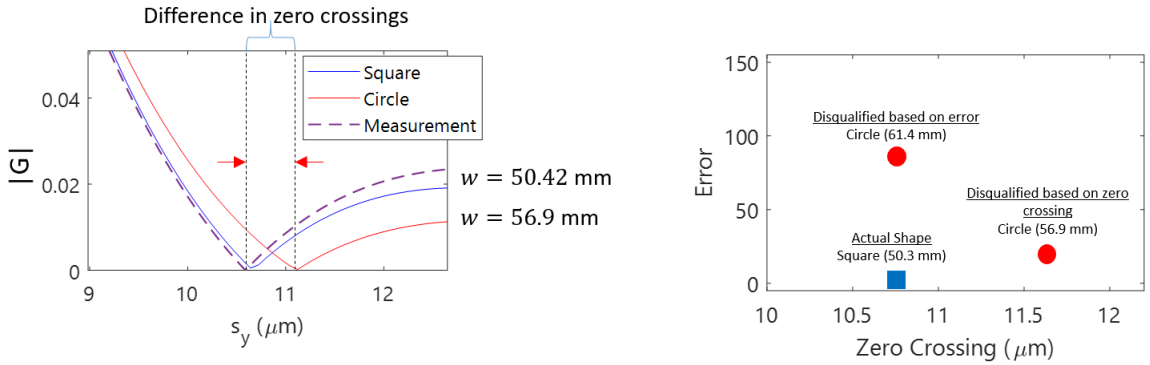

Figure 5.1: An approach for classifying a shape as as circle or a square and determining the shape width.

5.2.1 Optimization Problem

The first problem seeks to estimate the size of a source given its shape. The example here considers a square-shaped source, of which we seek to estimate the width. Simulated measurements were obtained by means of forward propagation followed by scattering using Monte Carlo simulations; both operations have been previously found to match experimental results [1, 3].

Given the measured coherence function G, the inversion is accomplished by minimizing the residual $\left\|\overline{G}(\mathbf{p}) - G\right\|_2^2$ with respect to the object parameter vector $\mathbf{p}$, where $\overline{G}(\mathbf{p})$ is the theoretical reflected coherence for the given source parameters. A Levenberg-Marquardt least squares fitting algorithm is used to perform the minimization. Measurements of coherence along one direction suffices. As described earlier, upon reflection at grazing angles, the coherence is better preserved in the off-plane direction (y-axis) than in the in-plane direction (x-axis) [120]. This motivates our choice of using coherence data only along the y-axis.

An example optimization is shown for a square shape in Fig. 5.2 (a). In this case, we have a

single width parameter w, i.e., we have $\mathbf{p} = w$. The estimation of the width was successful with convergence after six iterations.

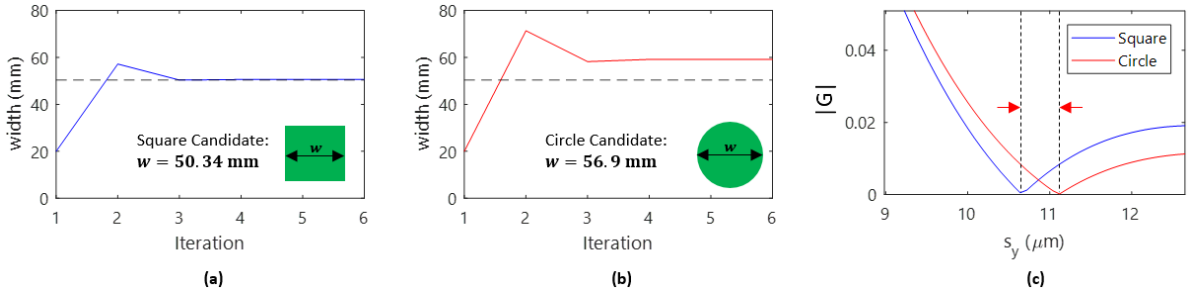

Figure 5.2: (a) Estimation of square width w. (b) Estimation of circle diameter w using same measurements as in (a). (c) Comparison of zero crossings of square and circle coherence functions.

Beyond estimating the object parameters, we are also able to solve the shape classification problem by using the first zero crossing. The same measurements G are used as in the previous example, but the new goal is to also classify the shape as either a square or a circle. To this end, we run the minimization problem for a circular object. The results indicates that a circle of width 56.9 mm minimizes the residual. The correct shape is discriminated by using the zero crossing along one axis, as shown in Fig. 5.2(c). This allows the shape to be successfully classified.

The physical scattering model indicates that the phase of the coherence function is maintained after scattering. This allows distance to be determined as well. An example is shown in Fig. 5.3, where in addition to the width, we also include distance in the parameter vector.

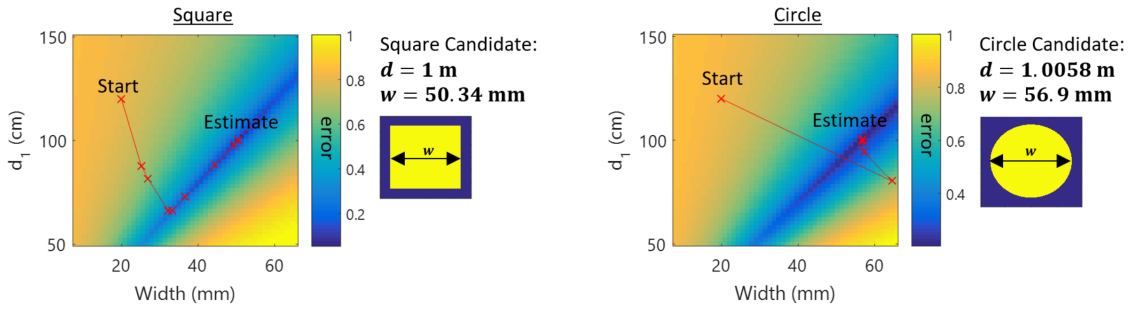

Figure 5.3: Extended estimation problem including distance.

The scenario is the same as that in Fig. 5.2. The square is placed at a distance of 1 m. For both the square and the circle candidates, the estimates of the width are the same as in Fig. 5.2, and the distance estimate is very close to the correct value. As before, we can decide which is the correct shape by comparing the zero crossings.

5.3 Non-line-of-sight Image Reconstruction

In this section, we turn to the problem of reconstructing the opacity profile of a large object. This 2D profile is represented in discretized form by matrix $\mathbf{G}$, which has vectorized form $\mathbf{g} = \text{vec}\{\mathbf{G}\}$. Matrix $\mathbf{G}$ is formed by sampling the opacity profile on a uniform grid over the finite support of the profile. First, we consider reconstruction using intensity-only measurements in the presence of ambient light from secondary sources. Then, leveraging the physical model for spatial coherence introduced in Section 4.2, we develop the reconstruction framework using coherence measurements. Finally, we define the complete problem in which we fuse information from both modalities and exploit the natural sparsity of the object's profile.

5.3.1 Intensity Measurements

The intensity pattern on the wall may be measured using a variety of readily available devices. For example, if intensity variations are strong enough, a simple Charge-Coupled Device (CCD) camera with a suitable lens may be used. At the other extreme, a device such as an Electron Multiplying CCD (EMCCD) can distinguish minute intensity variations, due to the camera's high single photon sensitivity.

We define the intensity measurement matrix $\mathbf{\Phi}^I$, which samples the scattered intensity function $I_S(\mathbf{r})$ in (4.15) at the wall. Hence, in discretized form

$$\mathbf{\Phi}^I \mathbf{g} = \frac{2\pi\sigma^2}{\lambda^2 d^2} \operatorname{vec}\{\mathbf{H} \star (\mathbf{1} - \mathbf{G})\} \tag{5.1}$$

where $\mathbf{H}$ is the discretized Gaussian kernel $H(\mathbf{r}')$ defined in (4.8). Because $\mathbf{G}$ is an opacity profile, the intensity in the object plane takes the form $\mathbf{1} - \mathbf{G}$, where the $\mathbf{1}$ term represents the light incident on the object immediately prior to obstruction.

In the experiments, we implement (5.1) using a linear convolution, i.e., elements outside the boundaries of the domain of $\mathbf{r}'$ are set to zero. This operation is performed through the use of convolution matrices such that the grids of $\mathbf{r}$ and $\mathbf{r}'$ may be different. If the grids are the same, we could also use the Fast Fourier Transform (FFT) to perform a fast circular convolution.

Therefore, to recover an estimation of the object profile $\mathbf{g}$ from intensity measurements (see Section 5.3.5 for a discussion of the null space), we formulate the convex program

$$\min_{\mathbf{g},\alpha} \left\| \mathbf{\Phi}^I \mathbf{g} + \alpha \mathbf{a} - \mathbf{y}^I \right\|_2^2, \tag{5.2}$$

where $\mathbf{y}^I$ is the measurement vector. This formulation includes a free coefficient α along with an

associated vector $\mathbf{a}$ modeling the ambient light. Specifically, vector $\mathbf{a}$ captures the spatial intensity distribution of the ambient light on the wall and the coefficient α represents its magnitude. Here, we set $\mathbf{a} = \mathbf{1}$, i.e., the ambient light blankets the wall with constant intensity.

While this problem may be successful if a clear shadow is discernible, two major factors limit its effectiveness. First, the shadow will be faint if there is significant ambient light present. Although the shadow can be measured with sensitive cameras, the Signal-to-Noise Ratio (SNR) falls as the amount of ambient light increases. Second, if the coherence of the light sources is low, the edges of the shadow will be indistinct due to diffraction, making the reconstruction ill-posed; this effect can be seen as a manifestation of the convolution in (4.15).

5.3.2 Coherence Measurements

To address the aforementioned limitations of the intensity-based approach, we develop a framework for reconstruction from coherence measurements next.

As described in the introduction, an increasing number of techniques have been developed for capturing coherence information. An example of practical measurements matching the requirements of our approach can be found in [51], which makes use of a Dual Phase Sagnac Interferometer (DuPSaI).

Because $\boldsymbol{\rho}$ appears in the argument to the Fourier transform of (4.6), a natural way to measure the coherence function $G_d(\mathbf{r}, \boldsymbol{\rho})$ is along the ρ_x and ρ_y axes with $\mathbf{r}$ fixed, i.e. measure a 2D slice of the 4D coherence function. We will refer to a set of measurements along this slice as a coherence sample. An example plot of such a coherence sample is shown in Fig. 5.4(b), with a detail zoom shown in (c). Here, $\mathbf{r} = (-0.4 \text{ m}, -0.4 \text{ m})$ is fixed, and the plot is over $\boldsymbol{\rho}$. The simulation parameters are $\lambda = 525$ μm and $\sigma = 2.5$ μm. Fig. 5.4(d) shows the results of wall scattering with

parameters $\mathbf{w} = (1\ \mu\text{m}, 6\ \mu\text{m})$.

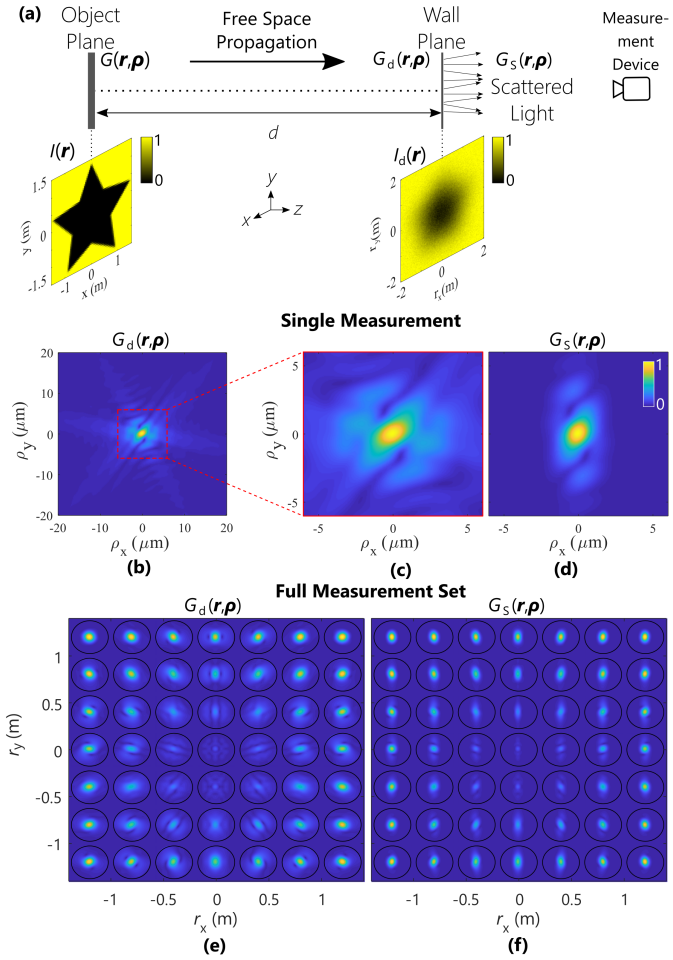

Figure 5.4: Details of spatial coherence model. All coherence plots show the magnitude of the coherence function. (a) Diagram of coherence model, including plots of the intensities in the object plane and wall plane. (b) Coherence of incident light in wall plane with (c) detail zoom. Plots are for spatial point $\mathbf{r} = (-0.4\ \text{m}, -0.4\ \text{m})$. (d) Coherence scattered from wall. (e) Set of incident coherences plotted on a 7×7 grid. Each plot is centered at the corresponding spatial point $\mathbf{r}$. The radius of each plot is $5.5\ \mu$m. The coherence measurements are shown in the style of light field plots as found for example in [4] and [5]. (f) Scattered coherences as in (d).

To achieve spatial diversity, a full reconstruction will typically require a collection of 2D coherence samples, each centered at a different $\mathbf{r}$. An example collection of 49 samples is given in Fig. 5.4(e) showing the coherence incident to the wall, with the $\mathbf{r}$ falling onto a 7×7 grid. The corresponding scattered coherence functions are shown in Fig. 5.4(f).

We remark that while the 2D intensity function constitutes a slice of the 4D coherence function, cameras used to measure intensity differ from devices used to measure coherence, therefore they are commonly considered as different modalities.

We define the coherence measurement matrix $\mathbf{\Phi}_{\mathbf{r}}^{C}$, which samples the scattered coherence function along the ρ_x and ρ_y axes at a fixed $\mathbf{r}$. Obtaining a discretized form of the function in (4.13), we can write

$$\mathbf{\Phi}_{\mathbf{r}}^{C}\mathbf{g} = \operatorname{vec}\left\{\mathbf{S} \odot \mathbf{C}_{\mathbf{r}} \odot \left(\mathbf{F}_1 \left[\mathbf{H}_{\mathbf{r}} \odot (\mathbf{1} - \mathbf{G})\right] \mathbf{F}_2\right)\right\}. \tag{5.3}$$

Matrix $\mathbf{S}$ is the discretized form of the function $S(\boldsymbol{\rho})$ defined in (4.14), which represents the scattering effects of the wall. Matrix $\mathbf{C}_{\mathbf{r}}$ is the discretized form of the function $C(\mathbf{r}, \boldsymbol{\rho})$ defined in (4.7), which is one component of the free space propagation operator. Both $\mathbf{S}$ and $\mathbf{C}_{\mathbf{r}}$ are discretized along the ρ_x and ρ_y axes using the same set of points as $\mathbf{\Phi}_{\mathbf{r}}^{C}$, with $\mathbf{C}_{\mathbf{r}}$ using the same fixed $\mathbf{r}$ position as $\mathbf{\Phi}_{\mathbf{r}}^{C}$. The other component of the free space propagation operator is matrix $\mathbf{H}_{\mathbf{r}}$, which discretizes the function H defined in (4.8). Specifically, this matrix contains samples of $H(\mathbf{r} - \mathbf{r}')$, with $\mathbf{r}$ fixed, and $\mathbf{r}'$ falling on the same discrete grid as $\mathbf{G}$.

Calculation using the measurement matrix (5.3) admits a tractable form, requiring only element-wise products and Fourier transforms, which may be implemented using the FFT.

The measurement vector corresponding to the coherence sample at $\mathbf{\Phi}_{\mathbf{r}}^{C}$ is labeled $\mathbf{y}_{\mathbf{r}}^{C}$. We define the set $\mathcal{R}$ containing the values of $\mathbf{r}$ at which the full collection of coherence samples are made. To

perform the reconstruction using coherence measurements, we consider the least squares formulation,

$$\min_{\mathbf{g}} \sum_{\mathbf{r}\in\mathcal{R}} \| \, \mathbf{\Phi}_{\mathbf{r}}^{C}\mathbf{g} - \mathbf{y}_{\mathbf{r}}^{C} \, \|_2^2. \tag{5.4}$$

A major factor influencing the quality of the coherence measurements are the geometry and characteristics of the wall which determine the amount of scattering. Because these factors may vary depending on spatial position along the wall, the different sets of measurements $\mathbf{y}_{\mathbf{r}}^{C}$ within the collection may vary in their quality, or some may be unusable. We will explore such a scenario in Section 5.4.2.

Given the geometry of the scene, the ambient light that reaches the detector will necessarily result from diffuse scattering (i.e., specularly reflected ambient light from secondary sources will not reach the detector due to unequal angles of incidence and reflection). Because there is a Fourier transform relationship between scattered photon angle and coherence (see Section 4.3.1 for more details), the large angle diffuse spread in the ambient light introduces a narrow peak in the coherence function at $\boldsymbol{\rho} = \mathbf{0}$ [3, 121]. Recalling the relationship between intensity and coherence $I(\mathbf{r}) = G(\mathbf{r}, \mathbf{0})$, we can see that the peak exactly coincides with the intensity measurements. Therefore, the ambient light tends to dominate the intensity measurements and obscure the shadow. On the other hand, this diffusely scattered ambient light has little effect on the coherence function away from $\boldsymbol{\rho} = \mathbf{0}$, where the specular component of reflection (containing information about the object) dominates. For this reason, spatial coherence coordinates for which $\| \, \boldsymbol{\rho} \, \|_2 < p$ are excluded. We remark that unlike (5.2), this exclusion obviates the need for an ambient term for the coherence measurements in the formulation of (5.4).

5.3.3 Fusion Framework

As mentioned in the previous sections, it is possible that one or another modality may be of a lower quality, and therefore it is advantageous to use both intensity and coherence modalities in the same reconstruction.

Additionally, the profile $\mathbf{g}$ is likely to admit a sparse representation $\mathbf{x}$ in a particular basis $\mathbf{\Psi}$. Here, we use the two-dimensional Discrete Cosine Transform (DCT) as the sparsifying basis $\mathbf{\Psi}$ (in which it is well established that natural images possess a sparse representation [122]), however, another basis such as a wavelet basis could also be used. As such, the object profile can be expressed as $\mathbf{g} = \mathbf{\Psi x}$. We then include $\| \mathbf{x} \|_1$ as a regularization term to promote sparsity in the reconstruction, where the ℓ_1-norm is a convex relaxation of the ℓ_0-norm [123].

To fuse information from both modalities and exploit the sparsity of the opacity profile in $\mathbf{\Psi}$, we can readily formulate the convex program

$$\begin{aligned} \min_{\mathbf{x},\alpha} \kappa \| \mathbf{x} \|_1 + \left\| \mathbf{\Phi}^I \mathbf{\Psi x} + \alpha \mathbf{a} - \mathbf{y}^I \right\|_2^2 \\ + \mu \sum_{\mathbf{r} \in \mathcal{R}} \left\| \mathbf{\Phi}_{\mathbf{r}}^C \mathbf{\Psi x} - \mathbf{y}_{\mathbf{r}}^C \right\|_2^2, \end{aligned} \tag{5.5}$$

where κ and μ are used to balance the objectives.

5.3.4 Algorithm

To solve (5.5), we propose an iterative algorithm based on the ADMM approach first introduced in [115]. This algorithm performs a dual ascent using the Augmented Lagrangian [124], which can

be written as

$$L_\beta(\mathbf{x}, \alpha, \mathbf{z}, \mathbf{y}) = \kappa \| \mathbf{z} \|_1 + \left\| \mathbf{\Phi}^I \mathbf{\Psi} \mathbf{x} + \alpha \mathbf{a} - \mathbf{y}^I \right\|_2^2 + \mu \sum_{\mathbf{r} \in \mathcal{R}} \left\| \mathbf{\Phi}_{\mathbf{r}}^C \mathbf{\Psi} \mathbf{x} - \mathbf{y}_{\mathbf{r}}^C \right\|_2^2 + \mathbb{R}\mathrm{e}[\mathbf{y}^*(\mathbf{x} - \mathbf{z})] + \frac{\beta}{2} \| \mathbf{x} - \mathbf{z} \|_2^2$$

where $\mathbf{y}$ is the Lagrange multiplier. We solve the minimization using the following updates at each step k:

$$\mathbf{x}^{k+1}, \alpha^{k+1} = \arg\min_{\mathbf{x}, \alpha} L_\beta \left(\mathbf{x}, \alpha, \mathbf{z}^k, \mathbf{y}^k \right), \tag{5.6}$$

$$\mathbf{z}^{k+1} = \arg\min_{\mathbf{z}} L_\beta \left(\mathbf{x}^{k+1}, \alpha^{k+1}, \mathbf{z}, \mathbf{y}^k \right), \tag{5.7}$$

$$\mathbf{y}^{k+1} = \mathbf{y}^k - \beta(\mathbf{z} - \mathbf{x}), \tag{5.8}$$

where the initial values $\mathbf{x}^0, \alpha^0, \mathbf{z}^0, \mathbf{y}^0$ are zero. The stopping criteria consist of thresholds placed on the residuals [115]. Specifically, the algorithm stops if the norm of the primal residual $\left\| \mathbf{x}^k - \mathbf{z}^k \right\|_2 < \epsilon^{\text{pri}}$ and the norm of the dual residual $\left\| \beta(\mathbf{x}^{k+1} - \mathbf{x}^k) \right\|_2 < \epsilon^{\text{dual}}$. Here, $\epsilon^{\text{pri}} = 0.5$ and $\epsilon^{\text{dual}} = 10^{-6}$.

Details regarding the calculation of the $\mathbf{x}$ and $\mathbf{z}$ update steps are given in Appendix C.

5.3.5 Mapping of Null Space

Due to various factors in the propagation and scattering process, the measurement matrices $\mathbf{\Phi}^I$ and $\mathbf{\Phi}_{\mathbf{r}}^C$ will typically possess a null space. We use the general notation $\mathbf{\Phi}_i$ to refer to the i^{th} measurement matrix, which may take the form of $\mathbf{\Phi}^I$ or $\mathbf{\Phi}_{\mathbf{r}}^C$, depending on the enumeration order of the matrices.

We can characterize the null space associated with measurement i as follows. The degree of co-

herence between the j^{th} element of the object profile $\mathbf{g}_j$ and the measurement can be quantified by $\tau_i(j) = \| \mathbf{\Phi}_i \mathbf{e}_j \|_2$. If $\tau_i(j)$ is close to zero, i.e. the SNR is very small, the element is considered to be in the null space of the measurement.

Similarly, we can look at the degree of coherence in the sparse domain using a similar operator $\widehat{\tau}_i(j) = \| \mathbf{\Phi}_i \mathbf{\Psi} \mathbf{e}_j \|_2$. The null space map may be especially useful when an explicit model is not known, for example in data-driven approaches.

5.3.6 Sample Weighting

It may improve the results if we can exclude certain measurements from the reconstruction rather than give equal weight to all measurements in the samples. To this end, we can substitute a weighted norm $\| \cdot \|_v$ in place of any of the Euclidean norms $\| \cdot \|_2$ in (5.5).

If the noise is known, the sample weight vector for the i^{th} measurement can be constructed using the decision metric

$$v_i(j) = \left(\frac{1}{n_i} \quad \underset{0}{\overset{1}{\gtrless}} \quad \frac{\eta}{N-1} \sum_{\substack{k=1 \\ k \neq i}}^{N} \frac{\| \mathbf{\Phi}_k \mathbf{\Phi}_i^* \mathbf{e}_j \|_2}{n_k} \right), \tag{5.9}$$

where j is the sample number, n_i is the noise level present in measurement i, and η is a calibration constant. This is a metric similar to the Transform Point Spread Function found in [125]. For a given measurement sample, this metric finds other samples which are coherent with the same image pixels. A given sample will be included in the optimization if it has a higher SNR than the other measurements.

5.3.7 Extensions

Here, we comment on possible extensions to the framework.

We are not constrained to problems in which the object is blocking light, but can also work in reflective scenarios. This can be accomplished by redefining $\mathbf{G}$ as the reflectivity rather than opacity of the object, and making the simple substitution $\mathbf{1} - \mathbf{G} \to \mathbf{G}$ in (5.1) and (5.3).

The problem (5.5) includes a single weight μ associated with the measurements. We may instead associate a weight coefficient with each measurement matrix in (5.5). These could be adjusted along a continuum to control the impact of particular samples. If the magnitudes of measurements are significantly different, these weights can maintain balance, e.g., by setting $\mu_i = 1/\| \mathbf{y}_i \|_2^2$. If there is Gaussian noise in the measurements with known magnitude, the Bayesian Compressive Sensing methodology can be used [126].

Another possible extension to the optimization problem is to incorporate an auto-scaling coefficient, e.g., to handle cases when the magnitude of measurements from different modalities are not calibrated to the same scale. To this end, we can add a scaling coefficient $\mathbf{B}$ to some of the measurements by making the substitution $\mathbf{y}_i \to \mathbf{B}\mathbf{y}_i$, and updating $\mathbf{B}$ in step (5.6). With this modification, the problem (5.5) remains convex.

5.4 Numerical Results

We now present examples demonstrating the proposed method laid out in Section 5.3 and making use of optimization problem (5.5). In all examples, the opacity profile of the actual object is as shown in Fig. 5.5(a) with corresponding DCT in (b).

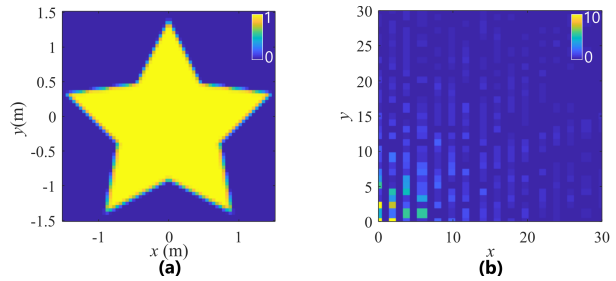

Figure 5.5: (a) Actual opacity used at object plane in forward model for all results. (b) Corresponding DCT. The color range for the DCT plot is restricted to $[0, 10]$ to highlight components with smaller magnitudes.

For simulated measurements, the source intensity function $I(\mathbf{r})$ used in the forward model is as shown in the diagram of Fig. 5.4(a) (left side), with the function extended by ones to $x, y \in (\pm 6 \text{ m})$, thus representing an opaque star object surrounded by a plane of light. The extension of the function is required to properly model the significant spreading of the light after being emitted from the physical light sources and before being obstructed by the object.

Additive-white-Gaussian-noise (AWGN) with standard deviation (SD) n_I is added to the intensity samples, and complex AWGN with SD n_C is added to the coherence samples.

The following parameters are used in all results: $\lambda = 525$ μm, $d = 6$ m, $p = 1$ μm, $\beta = 5 \times 10^{-3}$, and $\mu = 1$. The intensity image of the wall has resolution 101×101 pixels with domain $r_x, r_y \in [\pm 2 \text{ m}]$. Unless otherwise specified, the coherence measurements have resolution 51×51 pixels (with the domain of $\boldsymbol{\rho}$ varying depending on the example). A constant value of 100 is added to all intensity measurements to model ambient light; this offset will be absorbed by the coefficient α in (5.5).

5.4.1 Non-line-of-sight Imaging

We first demonstrate the potential of spatial coherence measurements to enable passive NLOS imaging when no shadow information is available. Two reconstructions are included, each with wall scattering parameters set at opposite extremes.

In this example, coherence measurements are made on the same spatial grid as shown in Fig. 5.4(f). The simulation parameters are $\sigma = 5$ μm, $n_C = 10^{-3}$, $\kappa = 0$, and the coherence measurements are over domain $\rho_x, \rho_y \in [\pm 15$ μm].

Fig. 5.6(a) and (b) shows the reconstructed image and DCT for a wall with relatively little scattering, where the scattering parameters are set to $\mathbf{w} = (3$ μm$, 18$ μm$)$.

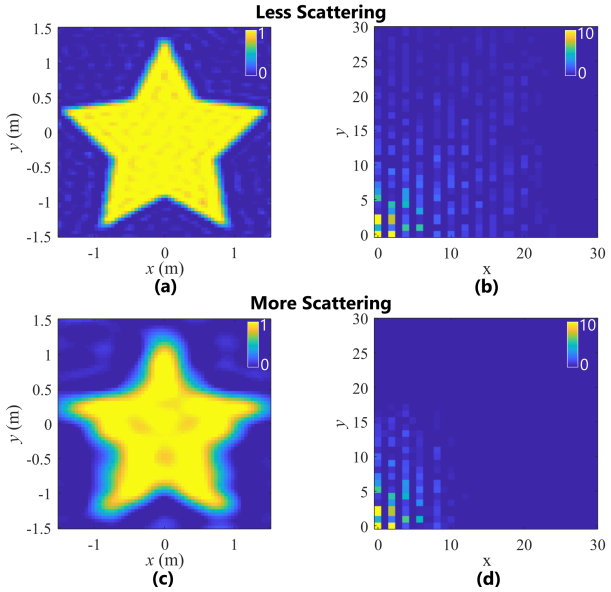

Figure 5.6: Results of NLOS object reconstruction using coherence only. The top half shows the reconstructed (a) image and (b) DCT for a wall that has relatively little scattering with $\mathbf{w} = (3\ \mu\text{m}, 18\ \mu\text{m})$. (c) and (d) show the corresponding plots for a wall with more scattering where $\mathbf{w} = (0.25\ \mu\text{m}, 1.5\ \mu\text{m})$. Pixels in the reconstructed images with value > 1 are set to one and values < 0 are set to zero

For comparison purposes, pixels in the reconstructed images with value > 1 are set to one and values < 0 are set to zero, a practice which will be used for the remainder of this section.

Fig. 5.6(c) and (d) show the results for a wall that introduces more scattering with parameters $\mathbf{w} = (0.25\ \mu\text{m}, 1.5\ \mu\text{m})$. The DCTs clearly show that the scattering of the wall acts as a low-pass filter, with increased scattering leading to more filtering.

5.4.2 *Fusion of Intensity and Coherence Measurements*

As demonstrated in the next example, by fusing intensity and coherence measurements, a better reconstruction can be made as compared to using either modality alone.

The simulation parameters used in this example are $\sigma = 2.5\ \mu$m, $n_I = 5 \times 10^{-2}$, $n_C = 10^{-2}$, $\mathbf{w} = (2\ \mu\text{m}, 6\ \mu\text{m})$, $\kappa = 10^{-3}$, and $\rho_x, \rho_y \in [\pm 10\ \mu\text{m}]$.

First, Fig. 5.7(a) shows an intensity sample. Note that the color range of the intensity plot has been constrained to a narrow range to clearly show the shadow. The light is not coherent enough to reveal the edges of the star. Fig. 5.7(b) shows the reconstructions results when only this sample is used.

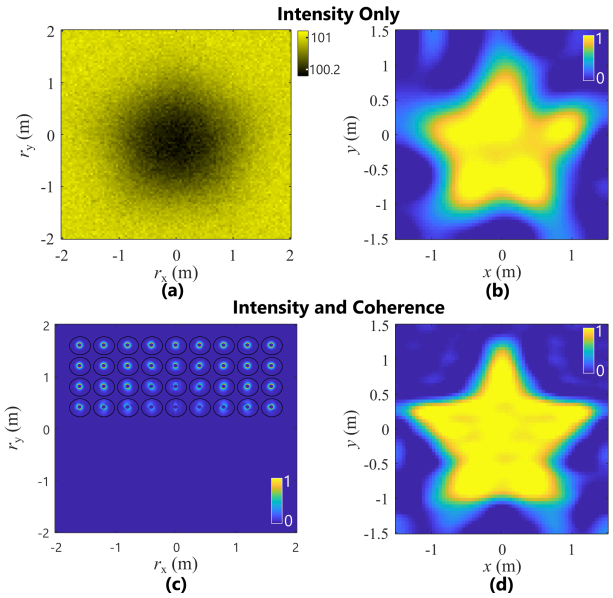

Figure 5.7: Fusion results. (a) Shows an intensity sample, and (b) shows the reconstruction using this sample alone. (c) Shows an additional measurement of scattered coherence, each sample having plot radius $5.2\ \mu$m. The measurements only cover part of the wall. (d) Shows the reconstruction when both the intensity and coherence measurements are used.

Next, the coherence samples shown in Fig. 5.7(c) are also included in the reconstruction to augment the intensity measurements. Fig. 5.7(d) shows the improved results. In the top half of the reconstruction, the coherence measurements contain more information about the high frequency components of the object profile and therefore dominate the reconstruction providing sharper edges. However, because these coherence measurements only cover the top half of the wall, the intensity contains more information about the bottom half of the object, albeit only at lower frequencies thus resulting in less definition.

We will now provide some insight into the improvements which have been made based on Section 5.3.5.

First, the spatial limitation inherent in coherence measurements is demonstrated. This limitation comes from the multiplication by the Gaussian term $H(\mathbf{r})$ in (4.6). In the following discussion, we denote the index of the intensity sample as $\mathcal{I}$, and the index set of coherence samples as $\mathcal{C}$. In Fig. 5.8(a), we show $\boldsymbol{\tau}_i$ for a single coherence sample located at $\mathbf{r} = (0, 0.8\text{ m})$.

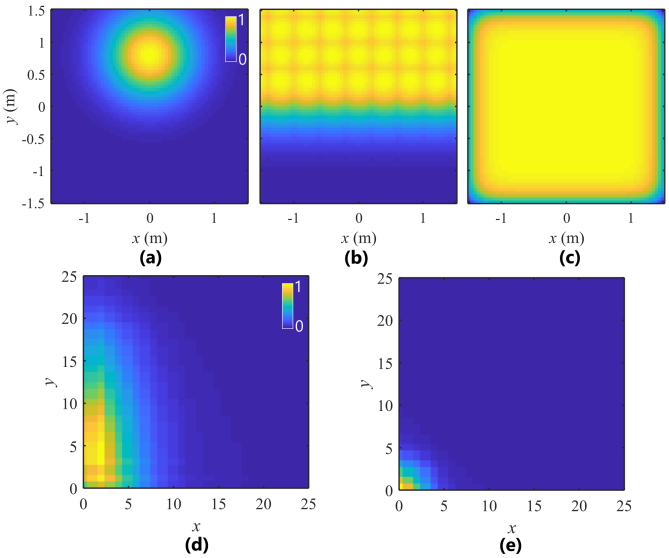

Figure 5.8: Null spaces for measurements (small values indicate an element is in the null space). Null spaces in image basis of (a) single coherence sample, (b) all coherence samples, and (c) intensity sample. Null space in DCT basis of (d) all coherence samples and (e) intensity sample. All color scales are normalized to their respective maximum values.

Fig. 5.8(b) shows $\max_{i \in \mathcal{C}} \boldsymbol{\tau}_i$, which returns a vector containing the most coherent coherence measurements with each pixel. This is the combined effect of all coherence samples, clearly demonstrating that more samples allow more spatial coverage. In contrast, Fig. 5.8(c) shows $\max_{i \in (\mathcal{I} \cup \mathcal{C})} \boldsymbol{\tau}_i$, demonstrating that when all coherence measurements are used together with intensity measurements, virtually the entire object profile is covered.

We can perform a similar analysis in the sparse DCT domain. Fig. 5.8(d) shows $\max_{i \in \mathcal{C}} \widehat{\boldsymbol{\tau}}_i$, which is the combined effect of the coherence samples in the sparse basis, and Fig. 5.8(e) shows $\widehat{\boldsymbol{\tau}}_{\mathcal{I}}$, which is the effect of the intensity measurements in the sparse basis. It can be seen that the coherence measurements have a stronger correlation with the high frequency components, explaining why the top half of Fig. 5.7(b) has improved edges over the bottom half. The low pass filtering in

the intensity measurements comes from the convolution in (4.15) due to diffraction, whereas the filtering in the coherence measurements comes from wall scattering.

5.4.3 Improved Fusion Using Sample Weighting

In some cases, simply adding new measurements is insufficient. Because of noise levels, while certain parts of the reconstruction will improve, other parts will degrade. In these cases being able to exclude individual measurements as described in Section 5.3.6 may resolve the issue. We now provide such an example.

The simulation parameters used in this example are $\sigma = 5$ μm, $n_I = 0.25$, $n_C = 10^{-4}$, $\mathbf{w} = (1\ \mu\text{m}, 6\ \mu\text{m})$, $\boldsymbol{\rho}_x, \boldsymbol{\rho}_y \in [\pm 15\ \mu\text{m}]$, and $\eta = 0.25$. For Fig. 5.9(b), $\kappa = 0$ and for Fig. 5.9(d) and (f), $\kappa = 1.5 \times 10^{-2}$.

Coherence measurements and the associated reconstruction are shown in Fig. 5.9(a) and (b) respectively. In these panels we do not use regularization, since the measurements lack noise.

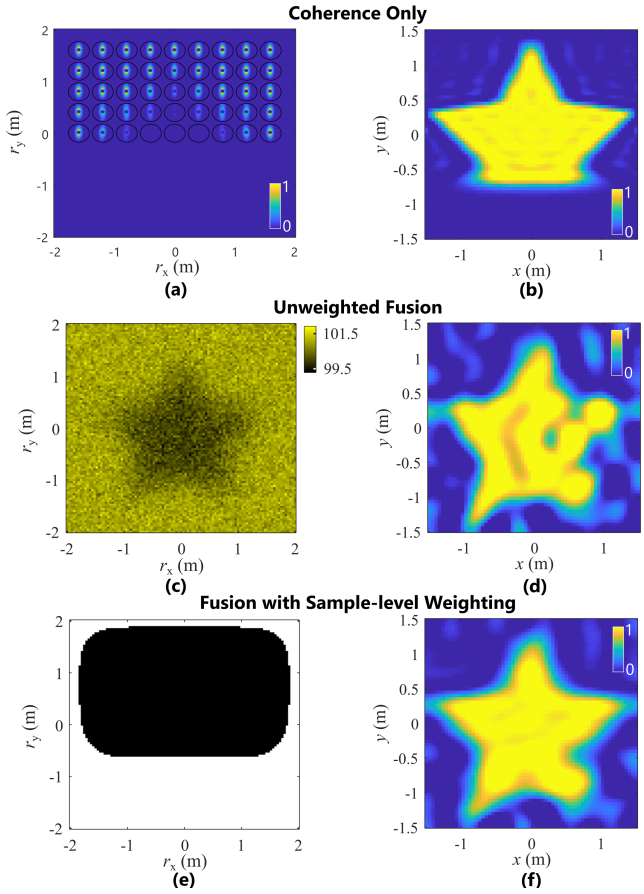

Figure 5.9: Example of sample weighting. (a) shows a set of coherence samples, each with plot radius 5.4 μm, and (b) the corresponding reconstruction. As in the example of Fig. 5.7, the coherence measurements only provide a reconstruction of the top half of the image. (c) An intensity sample, which is fused with the coherence samples to create reconstruction (d). Due to noise in the intensity measurements, the quality of the reconstruction is poorer. (e) The sample weights for the intensity measurement as calculated using (5.9). White regions indicate intensity samples which are included in the reconstruction, i.e. measurements j for which $\mathbf{v}_{\mathcal{I}}(j) = 1$, and black regions indicate exclusions, i.e. for which $\mathbf{v}_{\mathcal{I}}(j) = 0$. (f) Reconstruction from the same intensity and coherence samples, but using the weights shown in (e).

If the intensity sample shown in Fig. 5.9(c) is also used in addition to the coherence measurements, the results in Fig. 5.9(d) are obtained. Here, sparsity regularization is used due to noise in the intensity measurements. Although the bottom half of the object is now visible in the reconstruction, the top half has degraded due to the intensity noise.

To resolve this problem, we calculate sample weights for the intensity measurement using (5.9). The results are shown in Fig. 5.9(e) with black representing zeros (excluded intensity samples) and white representing ones (included samples).

The result of the reconstruction using these weights is shown in Fig. 5.9(f), where the top half can be seen to improve. Note that because we are regularizing in the frequency domain, noise which is *spatially* isolated to a particular section of the image will be coupled to other noise-free regions, and thus the top half is not ideal as possible. Using a wavelet basis may eliminate this issue.

5.4.4 Sparsity

Fig. 5.5(b) confirms that the DCT of this object profile is approximately sparse (disregarding the small high frequency components). At the same time, noise in the measurements tends to introduce relatively large high frequency components into the reconstruction. Therefore, one use for the sparsity regularizer in (5.5) is to serve as a de-noising tool.

In Fig. 5.10(a) we show the result of a reconstruction using noisy coherence measurements where no regularization is used, i.e. $\kappa = 0$. As shown in Fig. 5.10(b), the noise appears mostly in the high frequency components of the DCT.

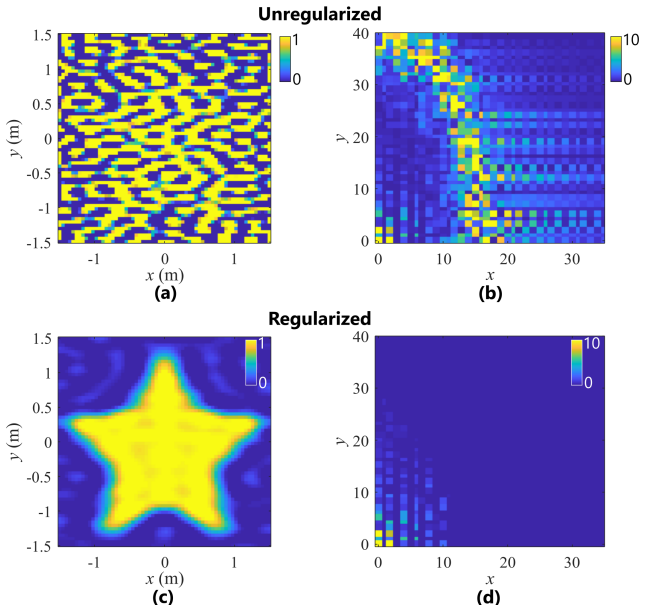

Figure 5.10: Demonstration of ℓ_1 norm regularization for noise reduction. In this example, only coherence measurements are used. (a) and (c) shows the reconstructed object profiles. (b) and (d) shows the corresponding DCTs.

Fig. 5.10(c) and (d) show the improved results when sparsity is enforced using $\kappa = 5 \times 10^{-4}$.

The coherence measurements are at the same spatial locations as shown in Fig. 5.4(f). The simulation parameters are $\sigma = 5$ μm, $n_C = 10^{-2}$, $\mathbf{w} = (1\ \mu\text{m}, 6\ \mu\text{m})$ and $\rho_x, \rho_y \in [\pm 15\ \mu\text{m}]$ with a resolution of 25×25.

In Table 5.1, we repeat this experiment using the same parameters, except varying the noise levels and κ values. Ten trials are performed at each setting, and the average and SD of the resulting Mean Square Error (MSE) are shown.

Likewise, Table 5.2 shows the results using only intensity measurements (and no coherence measurements). Here, the coherence level used for the forward model is $\sigma = 2.5$ μm (to reduce the

distinctness of the shadow).

For each noise level (column), the minimum error is bolded. We can see in both tables that a larger noise level requires a larger value of κ to achieve minimal MSE. The errors in the bottom row are roughly equal for all noise levels: beyond a certain threshold of κ, the estimates only contain low frequency components and are nearly identical.

Table 5.1: MSE of coherence-only measurements (average and standard deviation)

κ	Noise (n_C)			
	0	0.01	0.05	0.1
0	$\mathbf{0.008}$	5.334 ± 1.111	126 ± 19	621 ± 76
0.0005	0.014	$\mathbf{0.015 \pm 0.001}$	0.59 ± 0.08	9.35 ± 2.23
0.005	0.020	0.020 ± 0.000	$\mathbf{0.03 \pm 0.00}$	0.12 ± 0.02
0.05	0.041	0.041 ± 0.000	0.04 ± 0.00	$\mathbf{0.04 \pm 0.00}$
0.5	0.140	0.140 ± 0.000	0.14 ± 0.00	0.14 ± 0.00

Table 5.2: MSE of intensity-only measurements (average and standard deviation)

κ	Noise (n_I)			
	0	0.1	0.5	1
0	$\mathbf{0.04}$	0.09 ± 0.02	0.742 ± 0.223	3.019 ± 1.817
0.05	0.06	$\mathbf{0.07 \pm 0.00}$	0.138 ± 0.032	1.146 ± 0.532
0.10	0.08	0.08 ± 0.00	0.089 ± 0.014	0.402 ± 0.227
0.50	0.09	0.09 ± 0.00	$\mathbf{0.088 \pm 0.003}$	0.097 ± 0.009
1.00	0.09	0.09 ± 0.00	0.091 ± 0.003	$\mathbf{0.096 \pm 0.006}$
5.00	0.12	0.12 ± 0.00	0.115 ± 0.002	0.123 ± 0.009

5.5 Possible Extensions to the Imaging Approach

In our work, we assume the optical distance to be known. In [51], a technique is provided for determining the optical distance using the phase of the measurements at different spatial positions along the wall, information which is readily available in the measurements we use here. This estimation could be performed as a preprocessing step, prior to running our algorithm. The estimation of depth in the presence of scatterers has also been studied previously [36, 127], and those results may help here as well.

In our problem, we reconstruct a planar object profile. An extension of this work would be to consider three-dimensional objects, for example as was done in [128] and [129].

CHAPTER 6: FUTURE DIRECTIONS

6.1 Phase-Space Optics: The Wigner Function

In this dissertation, we have primarily represented the optical field via its spatial coherence function. As an alternative, we could represent the field by a phase-space function, which simultaneously describes both the space and angular spectrum of the light [34, 36]. One popular choice of phase-space function found in computational imaging is the light-field function, which is defined over a vector field of light rays. However, this function is restricted to the domain of geometric optics.

For wave fields, the analogous phase-space function is the Wigner distribution function $W(\mathbf{r}, \boldsymbol{\nu})$, where $\mathbf{r}$ are the spatial coordinates and $\boldsymbol{\nu}$ are frequencies (indicating direction). The Wigner function relates to the spatial coherence function through the transformation

$$W(\mathbf{r}, \boldsymbol{\nu}) = \iint G(\mathbf{r}, \boldsymbol{\rho}) \exp(-i2\pi\boldsymbol{\rho}\boldsymbol{\nu}) d\boldsymbol{\rho}. \tag{6.1}$$

We can think of the Wigner function as a generalization of the light-field which incorporates diffraction and other wave optics effects [36]. For more details on the relation between the Wigner function and the light-field, including assumptions under which they can be considered equivalent, see [130]. We also note that the Wigner function is closely related to the specific intensity defined in Section 4.3.1 – in the paraxial regime we work in here, we will treat them as identical.

The Wigner function and specific intensity were originally introduced in optics as a way of relating partial coherence to radiative transfer [112, 131, 132]. It is for this reason that specific intensity is used in [3, 51] to bridge the gap between the wave model used in free space propagation and the

photon-based scattering model used inside the wall.

Here, we are interested in the Wigner function for a different reason: the simple effect that free space propagation has on the function. Given a Wigner function $W_s(\mathbf{r}', \boldsymbol{\nu}')$ in the source plane, the Wigner function $W_d(\mathbf{r}, \boldsymbol{\nu})$ of the field after propagation by distance d is

$$W_d(\mathbf{r}, \boldsymbol{\nu}) = W(\mathbf{r} - \lambda d\boldsymbol{\nu}, \boldsymbol{\nu}). \tag{6.2}$$

Thus the propagation simply introduces a horizontal shear. From here-on we will look at a 1D scalar field, which renders the Wigner function a 2D function $W(x, \nu)$.

We proceed to illustrate why this propagation characteristic of the Wigner function is useful. In Fig. 6.1(a), we show the spatial coherence function, Wigner function, and intensity profile in the plane of a small object (immediately after interaction with the object).

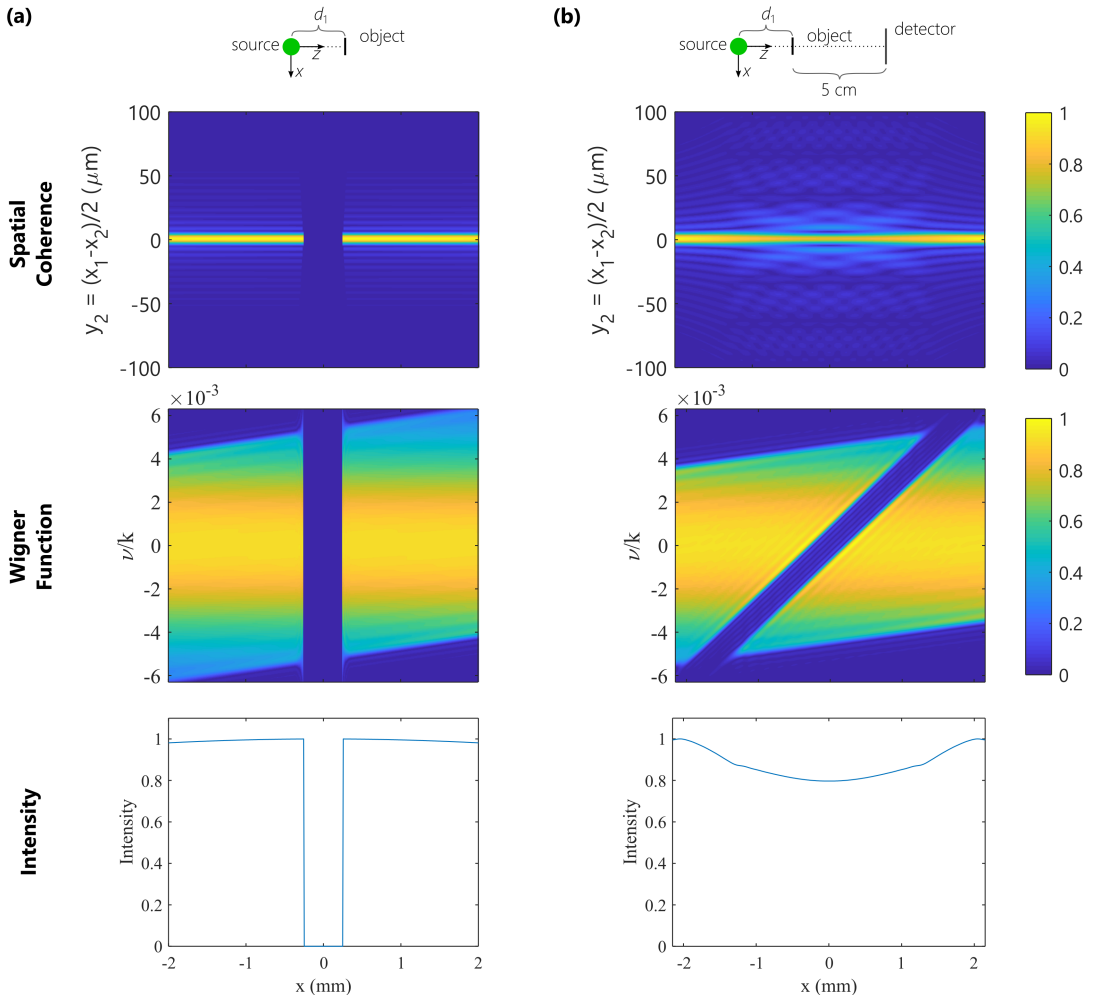

Figure 6.1: (a) Spatial coherence function, Wigner function, and intensity profile of optical wave field immediately after interaction with the object. (b) Corresponding functions/profile after propagation by a distance of 5 cm past the object.

The object forms a distinct vertical "shadow" in both the spatial coherence function and Wigner function (the exact effect of a transmission mask on the Wigner function takes the form of a convolution and is described in [130, Section 3.2]). Fig.6.1(b) shows the effect of propagation by a distance of 5 cm. The intensity profile has blurred and the spatial coherence function does not

provide a clear visual indication of the object. However, a shadow is still clearly visible in the Wigner function, only sheared by the propagation. We could establish the size and distance of the object by applying simple geometric techniques. In [36], it is shown that just such an approach can be used to identify points sources in different planes, since the points sources take the form of a thin line in the Wigner function.

However, in NLOS situations, the scattering of the wall obscures the shadow in the Wigner function. We illustrate this with an example. In Fig.6.2 we show the same setup as in Fig. 6.1, except here we imagine that a wall has been placed 20 cm from the object. At this distance, the intensity profile is almost uniform. We use the wall model described in Section 4.4.1 with a standard deviation of $w_x = 6$ μm (because we are using a 1D model, we only have scattering along the x-axis). Fig.6.2(a) shows the Wigner function before scattering. The shadow is still clearly visible. However, in Fig.6.2(b), which shows the results after scattering, we can no longer identify the object's shadow.

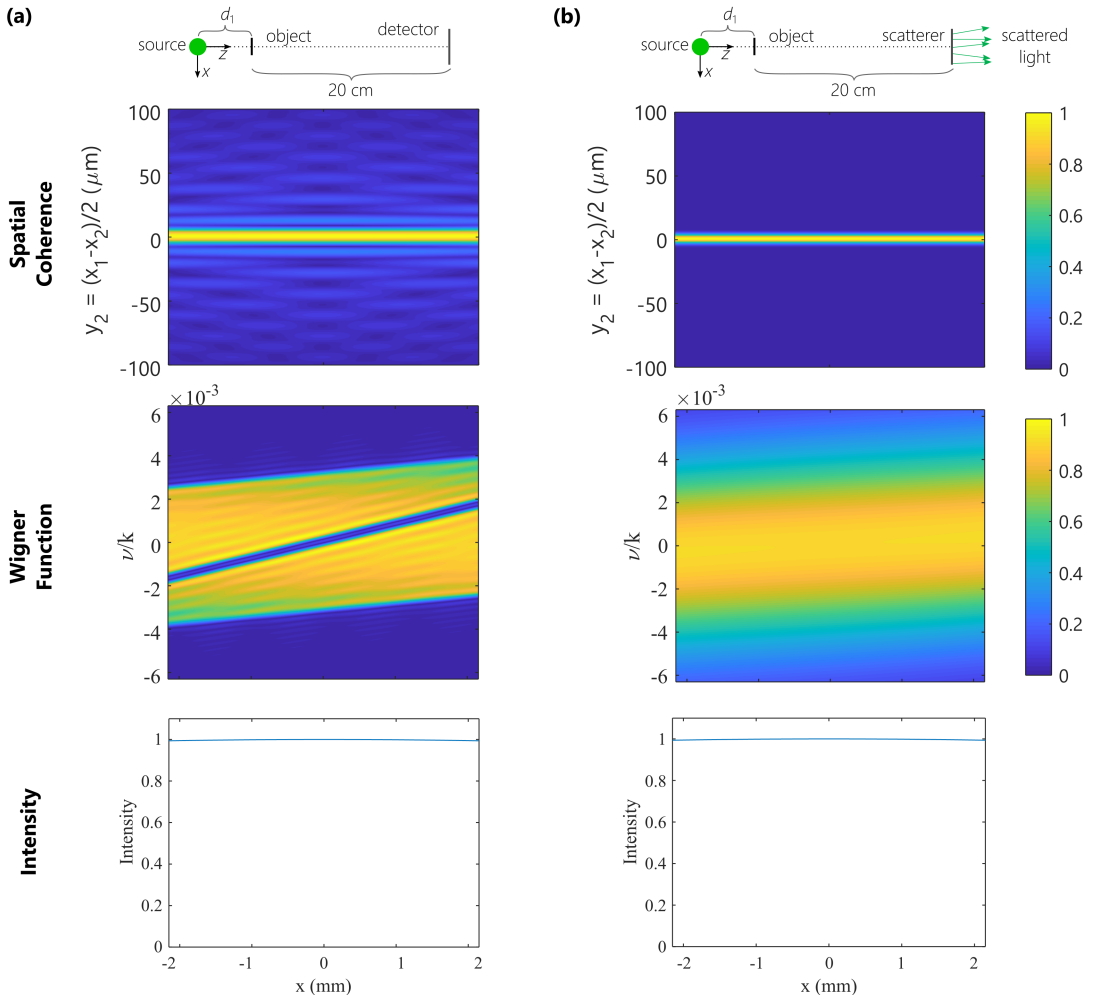

Figure 6.2: (a) Spatial coherence function, Wigner function, and intensity profile of optical wave field after propagation 20 cm past object. (b) Corresponding functions/profile at same distance as in (a), but after being scattered, i.e., by placing a wall 20 cm away from the object.

A future line of work could be to study the Wigner function and other phase-space representations. The question remains: could an approach be formulated to extract information about the object in phase-space, even after scattering?

6.2 Deep Learning

Deep learning has seen a surge in popularity in recent years. Due to increasing computational horsepower, improved techniques, and increasing volumes of available training data, Deep Neural Networks (DNN) have achieved unprecedented levels of success. A natural next step in the passive NLOS problem would be the incorporation of deep learning techniques into our framework. In this section, we first provide recent examples where deep learning has been applied to optics imaging/scene reconstruction problems. We then provide a list of techniques that are often used when applying deep learning to physics problems – these techniques could serve as a toolset for future work in NLOS imaging.

An example of deep learning applied to line-of-sight (LOS) problems can be found in [133]. In this work, a phase object is recovered using intensity measurements obtained after free space propagation. The inversion is accomplished by using a DNN to model the inverse operator. Thus the inverse operator is captured solely through a training process rather than an explicit derivation. The learned model may be able to incorporate prior information if a certain class of images is used (in [133], face images were used).

An example of deep learning in the non-line-of-sight (NLOS) setting can be found in [134]. This active approach uses laser illumination to recover the albedo of a hidden object. It incorporates a Convolutional Neural Network (CNN) to perform the phase retrieval step in NLOS correlography. The authors claim that traditional phase recovery algorithms perform far worse than the CNN in this noisy low-light setting. To generate sufficient training data, the authors synthesize training data using a derived noise model. As with [133], the training image dataset can be chosen to guide the priors the CNN learns.

We now provide a summary of physics-based deep learning techniques which could be applied in

future NLOS works.

- **Learning the inverse operator** A typical approach is to train the DNN to directly model the inverse operator. As described earlier, the DNN of [133] takes intensity measurements as input, and outputs a reconstruction of the source image. Similar approaches can be found for MRI images [135, 136].

- **Unrolled optimization** Rather than using the typical neural network components, we can use application-specific components to build the DNN. The parameters for these components are trained using the standard deep network techniques [137, 138]. This approach is often used to model optimization problems, for example ADMM, by unrolling the individual iterations. In this case, each layer of the DNN consists of an operation (for example a data consistency step or a regularization step) in a single iteration.

- **Regularization** The work [139] solves a regularized least-squares problem to form MRI images. A similar approach can be found in [140]. In both of these works, the optimization problem is solved using an unrolled gradient descent algorithm with the proximal regularization step performed by a DNN. The data consistency step is solved using traditional methods, invoking a known linear operator for the measurement matrix (forward model).

- **Solving Partial Differential Equations (PDEs)** If the problem is formulated as a PDE, then Physics-Informed Neural Networks (PINNs) can be used, for example by using a meshless approach [141, 142].

While not directly physics-related, we comment here on image processing techniques which may be used to post-process the reconstructed image in LOS and NLOS imaging.

- **Superresolution** CNNs can be used to estimate high resolution images based on low resolution inputs [143].

- **Edge detection** See [144].
- **Denoising** DNNs can be used for the purpose of denoising an image, e.g., in place of a classic Gaussian denoiser [144].

To conclude this section, we comment on some drawbacks of deep learning approaches. One issue is the typical requirement for large amounts of training data, which may be difficult to collect. Even with a large amount of training, novel situations may still be missed, leading to poor results. A related issue is that of overfitting. Specifically, if the complexity of the network is too low, or the datasets are too limited, the network may not function correctly in critical situations. Another longstanding issue with deep learning (in general) is a lack of interpretability of results, even when the deep learning approach is functioning properly. This highlights a benefit to the methods developed in this dissertation: the results output by our techniques are easily interpretable since they are based on well-understood physical models and optimization problems.

CHAPTER 7: CONCLUSION

In this dissertation, we considered the problem of *passive* NLOS scene reconstruction. We first studied the LOS scene reconstruction problem, and then proposed a solution to the complete problem with wall scattering. The key contributions are summarized below.

1. **Free space propagation forward model** We developed simulation software based on physical models and showed that numerical calculations of the propagation operator match both 1D and 2D experimental measurements. Furthermore, we showed that the spatial coherence function at a distant detector retains artifacts from interaction with an object, thus enabling the inverse problem to be solved. To further facilitate solution of the inverse problem, we derived closed-form analytic approximations for spatial coherence propagation after interaction with an object.

2. **Free space propagation inverse problem** We considered two techniques for solving the inverse problem in free space propagation. The first is a "brute-force" approach for recreating the evolution of the intensity profile using the inverse Fresnel transform. The second is an efficient and systematic optimization method using the closed-form analytic approximations.

3. **Scattering forward model** We developed an experiment-based forward model for wall scattering. We examined what information is preserved after interaction with the wall in the spatial coherence function.

4. **Scattering inverse problem** We derived a method for characterizing shapes, and for determining the distance to a small, simple object. We then considered a comprehensive imaging problem concerning large hidden objects. We considered how shadow information could be used, and formulated a multi-modal fusion algorithm for solving the inverse problem.

APPENDIX A: PROOF FOR THEOREM FOUND IN CHAPTER 2

The proof of the theorem requires calculation of the Fourier transform of a truncated Gaussian. In this section we derive the required results[1].

For $\sigma > 0$ define the Gaussian function as $N^{\sigma}(x) = \exp\{-x^2/2\sigma^2\}$. For some $\sigma > 0$ and $\omega \in \mathbb{R}$ let us consider the Fourier transform of a truncated Gaussian

$$\Phi^{\sigma}(\omega, u) = \int_{-\infty}^{u} \exp(-i\omega x) N^{\sigma}(x)\, dx \tag{A.1}$$

and the *cumulative distribution function*

$$\Phi_0^{\sigma}(u) := \Phi^{\sigma}(0, u) = \int_{-\infty}^{u} N^{\sigma}(x)\, dx. \tag{A.2}$$

We first provide an exact formula for calculating (A.1). Recall the Hilbert transform defined in (2.19) and the conjugated Hilbert transform defined in (2.20). The following result gives an exact formula for Φ in terms of the conjugated Hilbert transform.

Lemma 1. *We have the following formula*

$$\Phi^{\sigma}(\omega, u) = \sqrt{\frac{\pi}{2}}\sigma \left[(I + iH^u)N^{1/\sigma}\right](\omega), \tag{A.3}$$

where I stands for the identity operator and H^u for the conjugated Hilbert transform in (2.20)*. More explicitly,*

$$\begin{aligned}\Phi^{\sigma}(\omega, u) = \sqrt{\frac{\pi}{2}}\sigma \Big(& N^{1/\sigma}(\omega) \\ & + i \exp(-i\omega u)\frac{1}{\pi} p.v. \int \frac{\exp(isu) N^{1/\sigma}(s)}{\omega - s} ds\Big).\end{aligned} \tag{A.4}$$

[1]In this appendix, we partially use the material published in the Journal of the Optical Society of America A (JOSA A), 2017 [9]

Proof. In the following, $\hat{f}$ denotes the Fourier transform of f.

$$\begin{aligned}
&\Phi^{\sigma}(\omega,u)\\
&\quad=\int \exp(-i\omega x)\mathbb{1}_{(-\infty,u)}(x)N^{\sigma}(x)dx\\
&\quad=\widehat{\mathbb{1}}_{(-\infty,u)}\star\widehat{N}^{\sigma}(\omega)\\
&\quad=\pi\left[\delta+i\exp(-i(\cdot)u)H\right]\star\sqrt{2\pi}\sigma N^{1/\sigma}(\omega)\\
&\quad=\sqrt{\frac{\pi}{2}}\sigma\left(N^{1/\sigma}(\omega)\right.\\
&\qquad\left.+i\exp(-i\omega u)\frac{1}{\pi}\text{p.v.}\int\frac{\exp(isu)N^{1/\sigma}(s)}{\omega-s}ds\right),
\end{aligned}\tag{A.5}$$

where

$$\mathbb{1}_{(-\infty,u)}(x)=\begin{cases}1, & x<u,\\ 0 & x>u.\end{cases}\tag{A.6}$$

In the third equality the Fourier transform is understood in the sense of (temperate) distribution.

□

We remark that from the properties of the Hilbert transform, it can be seen that the conjugated Hilbert transform obeys the inversion law $-(H^u)^2f(x)=f(x)$.

Apart from the exact formula (A.3), we are interested in an approximation with a form easier to handle analytically. We now give an approximation formula together with the estimate in the error.

Lemma 2.

$$\begin{aligned}
&\Phi^{\sigma}(\omega,u)\\
&\quad=N^{1/\sigma}(\omega)\Phi_0^{\sigma}(u)\left[1+(\mathrm{i}\sigma^2\omega)\exp(-iu\omega)\frac{N^{\sigma}(u)}{\Phi_0^{\sigma}(u)}R(\omega,u,\sigma)\right],
\end{aligned}\tag{A.7}$$

where

$$R(\omega, u, \sigma) = \int_0^1 \exp(-iu\omega x) \exp\left(\frac{\sigma^2\omega^2}{2}x^2\right) dx \tag{A.8}$$

In particular, we have

$$\Phi^\sigma(\omega, u) \approx N^{1/\sigma}(\omega)\Phi_0^\sigma(u) \tag{A.9}$$

provided

$$\left|\sigma^2\omega\frac{N^\sigma(u)}{\Phi_0^\sigma(u)}\right| \ll 1. \tag{A.10}$$

Proof. We will show that $\omega \mapsto \Phi^\sigma(\omega, u)$ satisfies the linear differential equation

$$\frac{d\Phi^\sigma(\omega, u)}{d\omega} + \sigma^2\omega\Phi^\sigma(\omega, u) = \mathrm{i}\sigma^2 \exp(-\mathrm{i}u\omega)N^\sigma(u). \tag{A.11}$$

Indeed, by differentiation,

$$\begin{aligned}
\frac{d\Phi^\sigma}{d\omega} &= \mathrm{i}\sigma^2 \int_{-\infty}^{u} \exp(-\mathrm{i}x\omega)\frac{d}{dx}\left[\exp\left(-\frac{x^2}{2\sigma^2}\right)\right]\mathrm{d}x \\
&= \mathrm{i}\sigma^2 \exp(-\mathrm{i}x\omega)\exp\left(-\frac{x^2}{2\sigma^2}\right)\Bigg|_{x\to-\infty}^{x=u} \\
&\qquad - \mathrm{i}\sigma^2(-\mathrm{i}\omega)\int_{-\infty}^{u}\exp(-\mathrm{i}x\omega)\exp\left(-\frac{x^2}{2\sigma^2}\right)\mathrm{d}x \\
&= \mathrm{i}\sigma^2 \exp(-\mathrm{i}u\omega)N^\sigma(u) - \sigma^2\omega\Phi^\sigma(\omega, u)\mathrm{d}x.
\end{aligned} \tag{A.12}$$

Using the integrating factor $\exp(\sigma^2\omega^2/2)$, an integration from 0 to σ, and a scaling by a factor of

σ in the ensuing integral, the formula (A.7) is obtained. We estimate R as follows

$$\begin{aligned} |R(\omega,\sigma,u)| &\leq \int_0^1 \exp\left(\frac{\sigma^2\omega^2}{2}x^2\right)\mathrm{d}x \\ &\leq \int_0^1 \exp\left(\frac{\sigma^2\omega^2}{2}x\right)\mathrm{d}x \\ &= \frac{2}{\sigma^2\omega^2}\left[\exp\left(\frac{\sigma^2\omega^2}{2}\right)-1\right], \end{aligned} \tag{A.13}$$

from which the estimate (A.9) and condition (A.10) follow.

□

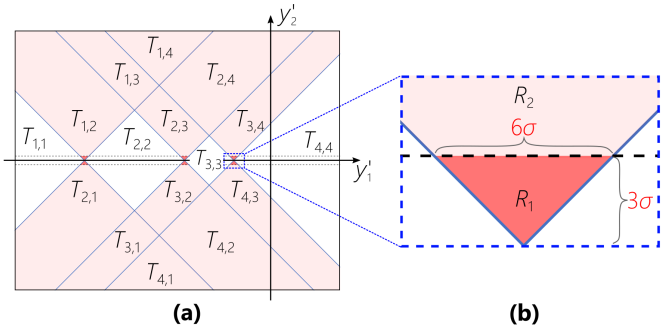

Figure A.1: Regions of approximation for Lemma 3. (a) shows the coefficients associated with each piecewise constant section. The region of approximation R_1 is shaded dark red, while the region R_2 is shaded light red. (b) provides a detailed view of one of the triangle regions making up region R_1.

Next, we provide a proof for the theorem stated in Section 2.6.2. The transmission function in the coherence space is

$$t(x_1')t^*(x_2') = \sum_{j,k=1}^{N} T_{j,k}\ \mathbb{1}_{B_{j,k}}(x_1', x_2') \tag{A.14}$$

where $\mathbb{1}$ denotes the indicator function and $T_{j,k}$ denotes the transmissivity coefficient within region

$$B_{j,k} = [a_{j-1}, a_j) \times [a_{k-1}, a_k), \quad 1 \leq j, k \leq N+1. \tag{A.15}$$

The coefficients are shown in Fig. A.1. As with the examples in Section 2.6.3, without loss of generality we may also use the transmission function $1 - t(x_1')t^*(x_2')$. In terms of the unmasked Gaussian beam $G^-(y_1', y_2') = A \, \exp\{iy_1'y_2'/R^2\} \, N^w(y_1') \, N^\sigma(y_2')$, the propagated coherence function is

$$\begin{aligned} &G_d(y_1, y_2) \\ &\quad = \frac{1}{2\pi\ell^2} \sum_{j,k=1}^{N+1} T_{j,k} \iint_{B_{j,k}} G^-(y_1', y_2') \, \mathcal{L}(y_1, y_1', y_2, y_2') \; dy_1' \; dy_2'. \end{aligned} \tag{A.16}$$

We first apply Lemma 3, which allows the source coherence to be approximated by a series of infinite strips.

Lemma 3. *Assume the hypotheses in the theorem. The propagated coherence function* (A.16) *can be approximated by*

$$\begin{aligned} &G_d(y_1, y_2) \\ &\quad \approx \frac{1}{4\pi\ell^2} \sum_{j=2}^{N} T_{j,j} \left(\iint_{S_j^+} G^-(y_1', y_2') \, \mathcal{L}(y_1, y_1', y_2, y_2') \; dy_1' \, dy_2' \right. \\ &\qquad\qquad \left. + \iint_{S_j^-} G^-(y_1', y_2') \, \mathcal{L}(y_1, y_1', y_2, y_2') \; dy_1' \, dy_2' \right) \end{aligned} \tag{A.17}$$

where we use the two strip regions $S_j^+ = \bigcup_{k=1}^{N+1} B_{j,k}$ *and* $S_j^- = \bigcup_{k=1}^{N+1} B_{k,j}$. *Moreover, the magnitude of the pointwise error in this approximation is bounded from above by* $\left[40\sigma + 4\sqrt{2\pi} w \Phi_0^1(-3)\right] A\sigma$.

Proof. We will assume for our source function G, that $T_{1,1} = T_{1,N+1} = T_{N+1,1} = T_{N+1,N+1} = 0$. Since

the source is Gaussian, an appropriate truncation (at $|y_1'| = 3w$ for example) will result in only a small error.

We start by approximating the source coherence by

$$G'(y_1', y_2') = \sum_{j,k=2}^{N} \frac{T_{j,j} + T_{k,k}}{2} \mathbb{1}_{B_{j,k}}(y_1' + y_2', y_1' - y_2')\, G^-(y_1', y_2') \tag{A.18}$$

Then we have

$$G(y_1', y_2') = G'(y_1', y_2') + R(y_1', y_2') \tag{A.19}$$

where

$$\begin{aligned} R(y_1', y_2') &= \sum_{\substack{j,k=2 \\ j \neq k}}^{N} \left(\frac{T_{j,k} + T_{k,j}}{2} - T_{j,j} \right) G^-(y_1', y_2') \\ &= R_1(y_1', y_2') + R_2(y_1', y_2'). \end{aligned} \tag{A.20}$$

Error terms R_1 and R_2 arise from different regions of the source as illustrated in Fig. A.1.

The term R_1 comes from integration over the region $\bigcup_{j,k=2}^{N} (B_{j,k} \bigcap \{|y_2'| \leq 3\sigma\})$ of small triangles as in Fig. A.1(b). The coherence function at $z = d$ due to this term can be bounded by

$$\begin{aligned} |R_{1,d}(y_1, y_2)| &= \left| \iint R_1(y_1', y_2') \mathcal{L}(y_1, y_1', y_2, y_2')\, dy_1'\, dy_2' \right| \\ &\leq \iint |R_1(y_1', y_2')|\, dy_1'\, dy_2' \\ &\leq A \sum_{j=1}^{N} |T_{j,j+1} + T_{j+1,j} - T_{j,j} - T_{j+1,j+1}| \\ &\quad \times \sum_{k=0}^{11} \int_{\frac{k}{4}\sigma}^{\frac{k+1}{4}\sigma} \int_{a_j - \frac{k+1}{4}\sigma}^{a_j + \frac{(k+1)}{4}\sigma} N^w(y_1') N^\sigma(y_2')\, dy_1'\, dy_2' \end{aligned}$$

$$
\begin{aligned}
&\leq \frac{5}{2} A\sigma^2 \sum_{j=1}^{N} |T_{j,j+1} + T_{j+1,j} - T_{j,j} - T_{j+1,j+1}| \\
&\qquad \times N^w\left(|a_j| - 3\sigma\right) \\
&\leq 40 A\sigma^2, \qquad \text{(A.21)}
\end{aligned}
$$

where the last inequality uses the hypothesis (2.18a).

The term R_2 comes from the region $\bigcup_{j,k=2}^{N} [(B_{j,k} \cup B_{k,j}) \bigcap \{|y_2'| > 3\sigma\}]$. Making use of the inequality $\left|\frac{T_{j,k}+T_{k,j}}{2} - T_{j,j}\right| \leq 2$ for any j, k, we have

$$
\begin{aligned}
|R_{2,d}(y_1, y_2)| &= \left| \iint R_2(y_1', y_2') \mathcal{L}(y_1, y_1', y_2, y_2')\, dy_1'\, dy_2' \right| \\
&\leq \iint |R_2(y_1', y_2')|\, dy_1'\, dy_2' \\
&\leq 4A \int_{3\sigma}^{\infty} \int_{-\infty}^{\infty} N^w\left(y_1'\right) N^\sigma\left(y_2'\right) dy_1'\, dy_2' \\
&= 4\sqrt{2\pi} A w \int_{3\sigma}^{\infty} N^\sigma\left(y_2'\right) dy_2' \\
&= 4\sqrt{2\pi} A w \sigma\, \Phi_0^1(-3) \qquad \text{(A.22)}
\end{aligned}
$$

If w is large and the transmission function t is zero outside the interval $[a_1, a_N)$, then we may instead bound the error R_2 by

$$
\begin{aligned}
|R_{2,d}(y_1, y_2)| &\leq 4A(a_N - a_1) \int_{3\sigma}^{\infty} N^\sigma\left(y_2'\right) dy_2' \\
&= 4\sqrt{2\pi} A(a_N - a_1)\sigma\, \Phi_0^1(-3). \qquad \text{(A.23)}
\end{aligned}
$$

□

Finally, the following lemma can be applied to reduce the propagation integrals over the strips to

a closed-form. Since the Fresnel approximation is assumed, in the following proof we use the fact that $y_1, y_2 \ll d$, and that the source must be concentrated about the origin in the y_1', y_2'-plane.

Lemma 4. *The contribution to the detected coherence due to the j-th strips can be approximated as*

$$\begin{aligned} G_{d,j}^{\pm}(y_1, y_2) &= \frac{1}{2\pi\ell^2} \iint_{S_j^{\pm}} G^{-}(y_1', y_2')\, \mathcal{L}(y_1, y_1', y_2, y_2')\, dy_1'\, dy_2' \\ &\approx \widetilde{G}_d(y_1, y_2)\, \frac{i}{2N^{\eta\widetilde{\sigma}}(y_2)} \\ &\qquad \times \left[\pm \left(H^{\pm b_j(y_1)} - H^{\pm b_{j-1}(y_1)} \right) N^{\widetilde{\sigma}/\eta} \right](y_2), \end{aligned} \tag{A.24}$$

where $\widetilde{G}_d$ is defined in (2.16)*, and the variables $\widetilde{\sigma}$, η, and b_j are as defined in Eqs. (2.15,2.22).*

Proof. We perform the integration over the strip

$$S_j^{+} = \{(y_1', y_2') \in \mathbb{R}^2,\ a_{j-1} \le y_1' - y_2' < a_j\}. \tag{A.25}$$

The calculation over the strip

$$S_j^{-} = \{(y_1', y_2') \in \mathbb{R}^2,\ a_{j-1} \le y_1' + y_2' < a_j\} \tag{A.26}$$

follows similarly and is not detailed.

$$\begin{aligned} &G_{d,j}^{+}(y_1, y_2) \\ &\quad = \frac{1}{2\pi\ell^2} \iint_{S_j^{+}} G^{-}(y_1', y_2')\, \mathcal{L}(y_1, y_1', y_2, y_2')\, \mathrm{d}y_1'\, \mathrm{d}y_2' \\ &\quad = \frac{1}{2\pi\ell^2} A \exp(\mathrm{i}y_1 y_2/\ell^2) \int \exp(-\mathrm{i}y_1' y_2/\ell^2) N^{w}(y_1') \end{aligned}$$

$$
\begin{aligned}
&\quad \times \int_{y_1'-a_j}^{y_1'-a_{j-1}} \exp\left(-\mathrm{i}y_2'\left[y_1-(1+\delta)y_1'\right]/\ell^2\right) N^\sigma\left(y_2'\right) \mathrm{d}y_2' \, \mathrm{d}y_1' \\
&= \frac{1}{2\pi\ell^2} A \exp(\mathrm{i}y_1y_2/\ell^2) \int \exp(-\mathrm{i}y_1'y_2/\ell^2) N^w\left(y_1'\right) \\
&\quad \times \left[\Phi^\sigma\left(\frac{y_1-(1+\delta)\,y_1'}{\ell^2}, y_1'-a_{j-1}\right)\right. \\
&\qquad \left. - \Phi^\sigma\left(\frac{y_1-(1+\delta)\,y_1'}{\ell^2}, y_1'-a_j\right)\right] \mathrm{d}y_1' \\
&\approx \frac{1}{2\pi\ell^2} A \exp(\mathrm{i}y_1y_2/\ell^2) \int \exp(-\mathrm{i}y_1'y_2/\ell^2) \\
&\qquad\qquad \times N^w\left(y_1'\right) N^{\ell^2/\sigma(1+\delta)}\left(y_1'-\frac{y_1}{1+\delta}\right) \\
&\qquad\qquad \times \left[\Phi_0^\sigma(y_1'-a_{j-1}) - \Phi_0^\sigma(y_1'-a_j)\right] \mathrm{d}y_1' \\
&= \frac{1}{2\pi\ell^2} A \exp(\mathrm{i}y_1y_2/\ell^2) N^{\widetilde{w}}\left(y_1\right) \\
&\qquad\qquad \times \int \exp(-\mathrm{i}y_1'y_2/\ell^2) N^{\ell^2/\widetilde{\sigma}}\left(y_1'-c_1\right) \\
&\qquad\qquad \times \left[\Phi_0^\sigma(y_1'-a_{j-1}) - \Phi_0^\sigma(y_1'-a_j)\right] \mathrm{d}y_1', \qquad \text{(A.27)}
\end{aligned}
$$

where

$$
c_1 = \frac{y_1}{(1+\delta)(1+\xi^2)}. \qquad \text{(A.28a)}
$$

Due to the nature of the inner integral of the second equality, the outer integral is effectively truncated such that $-3\sigma < y_1' - a_{j-1} < y_1' - a_j < 3\sigma$. Therefore, with the hypotheses (2.17) and Eqs. (2.18), the approximation formula (A.9) applies since

$$
\frac{\sigma^2}{\ell^2}\left[y_1-(1+\delta)y_1'\right] \frac{N^\sigma\left(y_1'-a_k\right)}{\phi_0^\sigma(y_1'-a_k)} \ll 1 \qquad \text{(A.29)}
$$

for $k=j-1, j$. Substituting $y_1' = y_1'' + c_1$, we continue

$$
\begin{aligned}
G^{+}_{d,j}(y_1, y_2) \approx & \frac{1}{2\pi\ell^2} A \exp(\mathrm{i} y_1 y_2/\ell^2) N^{\widetilde{w}}(y_1) \\
& \times \int \exp\bigl(-\mathrm{i} y_2 (y_1'' + c_1)/\ell^2\bigr)\, N^{\ell^2/\widetilde{\sigma}}(y_1'') \\
& \times [\Phi_0^{\sigma}(y_1'' + (c_1 - a_{j-1})) \\
& \qquad -\Phi_0^{\sigma}(y_1'' + (c_1 - a_j))]\, \mathrm{d}y_1'' \\
= & \widetilde{G}_d(y_1, y_2) \frac{\widetilde{\sigma}}{\sqrt{2\pi}\eta\, N^{\eta\widetilde{\sigma}}(y_2)} \\
& \times \left[\Phi^{\eta/\widetilde{\sigma}}\left(y_2, \frac{a_j - c_1}{\eta^2\ell^2}\right) - \Phi^{\eta/\widetilde{\sigma}}\left(y_2, \frac{a_{j-1} - c_1}{\eta^2\ell^2}\right)\right] \\
= & \widetilde{G}_d(y_1, y_2) \frac{i}{2N^{\eta\widetilde{\sigma}}(y_2)} \\
& \times \left[\left(H^{b_j(y_1)} - H^{b_{j-1}(y_1)}\right) N^{\widetilde{\sigma}/\eta}\right](y_2). \qquad \text{(A.30)}
\end{aligned}
$$

□

APPENDIX B: DERIVATION OF GRADIENTS FOUND IN CHAPTER 3

In this chapter, we derive the gradients used in Chapter 3[1]. From (2.20) and (2.21), assuming $T_{1,1} = T_{N+1,N+1} = 0$,

$$\begin{aligned}\overline{G}_d(y_1, y_2) = \widetilde{G}_d(y_1, y_2) \frac{i}{2N^{\eta\widetilde{\sigma}}(y_2)} \sum_{j=1}^{N} (T_{j,j} - T_{j+1,j+1}) \\ \times \exp\{-iy_2 b_j(y_1)\} \\ \times p.v. \frac{1}{\pi} \int \frac{\exp\{isb_j(y_1)\} N^{\widetilde{\sigma}/\eta}(s)}{y_2 - s} ds. \end{aligned} \tag{B.1}$$

Then,

$$\begin{aligned}\overline{G}_d(y_1, y_2) &= \frac{i\eta^3\ell^2}{\sqrt{2\pi}\widetilde{\sigma}} C(y_1, y_2) \sum_{j=1}^{N} (T_{j,j} - T_{j+1,j+1}) \\ &\quad \times \exp\{-iy_2 b_j(y_1)\} \\ &\quad \times p.v. \frac{1}{\pi} \int \frac{\exp\{isb_j(y_1)\} N^{\widetilde{\sigma}/\eta}(s)}{y_2 - s} ds \\ &= \frac{i\eta^3\ell^2}{\sqrt{2\pi}\widetilde{\sigma}} C(y_1, y_2) \sum_{j=1}^{N} (T_{j,j} - T_{j+1,j+1}) \\ &\quad \times p.v. \int \frac{\exp\left\{i(s - y_2)b_j(y_1) + iy_1 y_2 / \widetilde{R}^2\right\} N^{\widetilde{\sigma}/\eta}(s)}{y_2 - s} ds, \end{aligned} \tag{B.2}$$

where

$$C(y_1, y_2) = \frac{\widetilde{A}\widetilde{\sigma}}{\sqrt{2\pi}\eta^3\ell^2} N^{\widetilde{w}}(y_1) N^{\ell^2\eta/\sigma}(y_2). \tag{B.3}$$

The partial derivative of the real component of $\overline{G}_d$ with respect to breakpoint a_j is

$$\frac{\partial \mathbb{R}\mathrm{e}\left[\overline{G}_d\right]}{\partial a_j} = (T_{j,j} - T_{j+1,j+1}) \frac{1}{\sqrt{2\pi}\widetilde{\sigma}} C(y_1, y_2)$$

[1]In this appendix, we partially use the material published in the Journal of the Optical Society of America A (JOSA A), 2018 [10].

$$\times \cos\left(y_2 b_j(y_1) - y_1 y_2/\widetilde{R}^2\right)$$
$$\times \int \cos\left(s b_j(y_1)\right) N^{\widetilde{\sigma}/\eta}(s) ds. \tag{B.4}$$

Using the definition

$$\begin{aligned} D(y_1, y_2) =& (T_{j,j} - T_{j+1,j+1}) C(y_1, y_2) \\ & \times \exp\left(i y_2 b_j(y_1) - i y_1 y_2/\widetilde{R}^2\right) N^{\eta/\widetilde{\sigma}}\left(b_j(y_1)\right), \end{aligned} \tag{B.5}$$

we can express (B.4) as

$$\begin{aligned} \frac{\partial \mathbb{R}\mathrm{e}\left[\overline{G}_d\right]}{\partial a_j} =& (T_{j,j} - T_{j+1,j+1}) C(y_1, y_2) \\ & \times \cos\left(y_2 b_j(y_1) - y_1 y_2/\widetilde{R}^2\right) N^{\eta/\widetilde{\sigma}}\left(b_j(y_1)\right) \\ =& \mathbb{R}\mathrm{e}[D(y_1, y_2)] \end{aligned} \tag{B.6}$$

Similarly, for the imaginary part,

$$\frac{\partial \mathbb{I}\mathrm{m}\left[\overline{G}_d\right]}{\partial a_j} = -\mathbb{I}\mathrm{m}[D(y_1, y_2)] \tag{B.7}$$

We now introduce an arbitrary normalization function $P(y_1, y_2)$, and consider the residual function

$$f(y_1, y_2; \mathbf{a}, d) = \frac{\overline{G}_d(y_1, y_2; \mathbf{a}, d)}{\overline{P}(y_1, y_2)} - \frac{G_d(y_1, y_2)}{P(y_1, y_2)} \tag{B.8}$$

For the remainder of this section, to facilitate readability, the function parameters (y_1, y_2) will be omitted. The partial derivative of the squared modulus of f is

$$\frac{\partial}{\partial a_j}|f|^2 = 2\mathbb{R}\mathrm{e}[f]\frac{\partial \mathbb{R}\mathrm{e}[f]}{\partial a_j} + 2\mathbb{I}\mathrm{m}[f]\frac{\partial \mathbb{I}\mathrm{m}[f]}{\partial a_j}$$

$$
\begin{aligned}
=&2\mathbb{R}\mathrm{e}[f]\frac{\frac{\partial \mathbb{R}\mathrm{e}\left[\overline{G}_d\right]}{\partial a_j}\overline{P}-\frac{\partial \overline{P}}{\partial a_j}\mathbb{R}\mathrm{e}\left[\overline{G}_d\right]}{\overline{P}^2}\\
&+2\mathbb{I}\mathrm{m}[f]\frac{\frac{\partial \mathbb{I}\mathrm{m}\left[\overline{G}_d\right]}{\partial a_j}\overline{P}-\frac{\partial \overline{P}}{\partial a_j}\mathbb{I}\mathrm{m}\left[\overline{G}_d\right]}{\overline{P}^2}\\
=&\frac{2}{\overline{P}}\left\{\mathbb{R}\mathrm{e}[f]\left(\mathbb{R}\mathrm{e}[D]-\frac{\partial \overline{P}}{\partial a_j}\mathbb{R}\mathrm{e}\left[\frac{\overline{G}_d}{\overline{P}}\right]\right)\right.\\
&\left.-\mathbb{I}\mathrm{m}[f]\left(\mathbb{I}\mathrm{m}[D]-\frac{\partial \overline{P}}{\partial a_j}\mathbb{I}\mathrm{m}\left[\frac{\overline{G}_d^*}{\overline{P}}\right]\right)\right\}.
\end{aligned}
\tag{B.9}
$$

For unnormalized coherence, substituting $\overline{P}=1$ yields

$$
\begin{aligned}
\frac{\partial}{\partial a_j}|f|^2 =&2\left\{\mathbb{R}\mathrm{e}[f]\mathbb{R}\mathrm{e}[D]-\mathbb{I}\mathrm{m}[f]\mathbb{I}\mathrm{m}[D]\right\}\\
=&\sqrt{\frac{2}{\pi}}\frac{\widetilde{A}\widetilde{\sigma}}{\eta^3\ell^2}\left(T_{j,j}-T_{j+1,j+1}\right)\\
&\times\left\{\mathbb{R}\mathrm{e}[f]\,\mathbb{R}\mathrm{e}[\Psi_j]-\mathbb{I}\mathrm{m}[f]\,\mathbb{I}\mathrm{m}[\Psi_j]\right\}
\end{aligned}
\tag{B.10}
$$

with Ψ_j as defined in (3.11a). The summation (3.10) follows immediately.

For the degree of coherence, substituting the normalization $\overline{P}=\sqrt{\overline{I}_1\overline{I}_2}$ gives the residual $\widetilde{f}$ defined in (3.12a). Note that the normalized coherence is defined to be zero if either of the intensities is zero. The partial derivative of the normalization term is

$$
\begin{aligned}
&\frac{\partial\sqrt{\overline{I}_1\overline{I}_2}}{\partial a_j}\\
&=\frac{1}{2}\left(\overline{I}_1\overline{I}_2\right)^{-1/2}\left[\overline{I}_1\frac{\partial\overline{G}_d(y_1-y_2,0)}{\partial a_j}+\overline{I}_2\frac{\partial\overline{G}_d(y_1+y_2,0)}{\partial a_j}\right]\\
&=\frac{T_{j,j}-T_{j+1,j+1}}{2\sqrt{\overline{I}_1\overline{I}_2}}\left\{\overline{I}_1C(y_1-y_2,0)N^{\eta/\widetilde{\sigma}}\left(b_j(y_1-y_2)\right)\right.\\
&\left.+\overline{I}_2C(y_1+y_2,0)N^{\eta/\widetilde{\sigma}}\left(b_j(y_1+y_2)\right)\right\}
\end{aligned}
\tag{B.11}
$$

Substituting (B.11) into (B.9) and continuing,

$$\begin{aligned}\frac{\partial}{\partial a_j}|\widetilde{f}|^2 =& \frac{2}{\sqrt{\overline{I}_1\overline{I}_2}}\left\{\mathbb{R}\mathrm{e}\Big[\widetilde{f}\Big]\left(\mathbb{R}\mathrm{e}[D]-\frac{\partial\sqrt{\overline{I}_1\overline{I}_2}}{\partial a_j}\mathbb{R}\mathrm{e}[\overline{g}_d]\right)\right.\\ &\left.-\mathbb{I}\mathrm{m}\Big[\widetilde{f}\Big]\left(\mathbb{I}\mathrm{m}[D]-\frac{\partial\sqrt{\overline{I}_1\overline{I}_2}}{\partial a_j}\mathbb{I}\mathrm{m}[\overline{g}_d^*]\right)\right\}\\ =&\sqrt{\frac{2}{\pi}}\frac{\widetilde{A}\widetilde{\sigma}}{\eta^3\ell^2}\left(T_{j,j}-T_{j+1,j+1}\right)\\ &\times\left\{\mathbb{R}\mathrm{e}\Big[\widetilde{f}\Big]\,\mathbb{R}\mathrm{e}\Big[\widetilde{\Psi}_j\Big]-\mathbb{I}\mathrm{m}\Big[\widetilde{f}\Big]\,\mathbb{I}\mathrm{m}\Big[\widetilde{\Psi}_j\Big]\right\}\end{aligned} \tag{B.12}$$

with $\widetilde{\Psi}_j$ as defined in (3.12b).

APPENDIX C: OPTIMIZATION ALGORITHM DETAILS FOR IMAGE RECONSTRUCTION DESCRIBED IN SECTION 5.3

We define $\mathbf{U}_i := \mathbf{\Phi}_i\mathbf{\Psi}$, and let $\mathbf{V}_i = \operatorname{diag}\mathbf{v}_i$ be the weight matrix associated with the weighted norms (if sample weighting is not used, then $\mathbf{V}_i$ should be an identity matrix)[1].

The minimization step (5.7) takes the analytic form [115]

$$\mathbf{z}^{k+1} = \overline{S}_{\kappa/\beta}\left(\mathbf{z}^k + \mathbf{y}^k/\beta\right), \tag{C.1}$$

where the component-wise shrinkage operator is

$$\overline{S}_a(x_i) = \max\left\{1 - a/|\, x_i\,|, 0\right\} x_i. \tag{C.2}$$

For simplicity, in the following equations we use a single summation over all samples, rather than separating the intensity sample from the coherence samples as was done in (5.5). Additionally, the weight coefficient has been indexed and moved inside the summation. For coherence samples, i.e. where $i \in \mathcal{C}$, the ambient vector is set to $\mathbf{a}_i = \mathbf{0}$.

We solve step (5.6) using a gradient descent algorithm. The gradients are

$$\begin{aligned}\nabla_{\mathbf{x}} L_\beta = 2 \sum_{i\in(\mathcal{I}\cup\mathcal{C})} \mu_i \mathbb{R}\mathrm{e}[\mathbf{U}_i^*\mathbf{V}_i\mathbf{U}_i\mathbf{x} - \mathbf{U}_i^*\mathbf{V}_i(\mathbf{y}_i - \alpha\mathbf{a}_i)] \\ + \beta\mathbb{R}\mathrm{e}[\mathbf{x} - (\mathbf{z} - \mathbf{y}/\beta)], \\ \nabla_{\alpha} L_\beta = 2 \sum_{i\in(\mathcal{I}\cup\mathcal{C})} \mu_i \mathbb{R}\mathrm{e}[\alpha\mathbf{a}_i^*\mathbf{V}_i\mathbf{a}_i - \mathbf{a}_i^*\mathbf{V}_i(\mathbf{y}_i - \mathbf{U}_i\mathbf{x})].\end{aligned}$$

The initial conditions for the gradient descent at step $k+1$ are the values calculated at the previous step, i.e., $\mathbf{x}^k$ and α^k. The j^{th} step of the gradient descent inner loop is chosen to minimize the quadratic interpolation at points $\mathbf{x}^j - q\left(\nabla_{\mathbf{x}} L_\beta\right)$ and $\alpha^j - q\left(\nabla_\alpha L_\beta\right)$, where $q \in \{0.1, 0.5, 1\}$. Let

[1] In this appendix, we partially use the material published in the IEEE Transactions on Image Processing, 2019 [6].

$f^j = L_\beta(\mathbf{x}^j, \alpha^j, \mathbf{z}^k, \mathbf{y}^k)$. The descent algorithm stops when $\| f^{j+1} - f^j \| / f^j < \epsilon^{\text{grad}}$.

For the $\mathbf{x}$-update, we use the early termination technique described in [115, §4.3.2]. This is accomplished by splitting the ADMM algorithm into two parts: first the algorithm is run with $\epsilon^{\text{pri}} = 1$, $\epsilon^{\text{dual}} = 10^{-4}$, $\epsilon^{\text{grad}} = 10^{-3}$. Then, the thresholds are set to the final values of $\epsilon^{\text{pri}} = 0.5$, $\epsilon^{\text{dual}} = 10^{-6}$, $\epsilon^{\text{grad}} = 10^{-8}$.

While we used gradient descent for its simplicity and robustness, a possible enhancement would be to use an optimization algorithm with faster convergence.

APPENDIX D: SIGNAL PROCESSING IN DOUBLE-SLIT DMD EXPERIMENTAL SETUP

We now describe the method for extracting the coherence function magnitude and phase for the double-slit DMD device [2, 8] (see Fig. 1.4). The interference patterns recorded by the CCD take the form

$$I(x) \propto \mathrm{sinc}^2\left(\frac{kx\ell}{2\pi Mf}\right)\left\{I_1 + I_2 + 2|G(x_1-x_2)|\cos\left(\frac{kx}{Mf}(x_1-x_2) - \varphi\right)\right\}, \tag{D.1}$$

where $\varphi = \mathrm{Arg}\{G(x_1-x_2)\}$, $\ell \approx 22.7$ μm is the slit width, and I_1 and I_2 are the peak values of the diffraction patterns from each slit, which can be obtained by activating one slit at a time, $\mathrm{sinc}(x) = \frac{\sin(\pi x)}{\pi x}$, and $M = 2$ is the magnification of the optical relay preceding the $2f$ Fourier transform system comprising a lens of focal length $f = 20$ cm[1]. We obtain $|g(x_1-x_2)|$ from the visibility V of the recorded interferograms [Fig. 1.4(d)] along with intensity measurements from individual slits, whereas the phase $\mathrm{Arg}\{g(x_1-x_2)\}$ is obtained from the displacement of the interference pattern with respect to a reference [Fig. 1.4(e)].

The visibility $V = (I_{\max} - I_{\min})/(I_{\max} + I_{\min})$ is obtained from the measured interferogram, where $I_{\max}$ and $I_{\min}$ are the maximum and minimum values of $I(x)$, respectively, from which we obtain $|g(x_1-x_2)| = \frac{I_1+I_2}{2\sqrt{I_1 I_2}}V$ [Figs. 1.4(b)–1.4(d)]. To extract the phase $\mathrm{Arg}\{g(x_1-x_2)\}$, we estimate the displacement of the interference patterns at different separations $x_1 - x_2$ with respect to a fixed fringe location.

[1] In this appendix, we partially use the material published in Optics Express, 2017 [2].

APPENDIX E: PERMISSION LETTERS TO REPRINT ARTICLES IN THIS DISSERTATION

Reprint permission emails are shown in Fig. E.1 and Fig. E.2.

Dear Andre Beckus,
The IEEE does not require individuals working on a dissertation/thesis to obtain a formal reuse license however, you must follow the requirements listed below:

Textual Material

Using short quotes or referring to the work within these papers) users must give full credit to the original source (author, paper, publication) followed by the IEEE copyright line © [Year of publication] IEEE.

In the case of illustrations or tabular material, we require that the copyright line © [Year of original publication] IEEE appear prominently with each reprinted figure and/or table.

If a substantial portion of the original paper is to be used, and if you are not the senior author, also obtain the senior author's approval.

Full-Text Article

If you are using the entire IEEE copyright owned article, the following IEEE copyright/ credit notice should be placed prominently in the references: © [year of original publication] IEEE. Reprinted, with permission, from [author names, paper title, IEEE publication title, and month/year of publication]

Only the **accepted** version of an IEEE copyrighted paper can be used when posting the paper or your thesis on-line. You may not use the **final published** version

In placing the thesis on the author's university website, please display the following message in a prominent place on the website: In reference to IEEE copyrighted material which is used with permission in this thesis, the IEEE does not endorse any of [university/educational entity's name goes here]'s products or services. Internal or personal use of this material is permitted. If interested in
reprinting/republishing IEEE copyrighted material for advertising or promotional purposes or for creating new collective works for resale or redistribution, please go to

http://www.ieee.org/publications_standards/publications/rights/rights_link.html

to learn how to obtain a License from RightsLink.

If applicable, University Microfilms and/or ProQuest Library, or the Archives of Canada may supply single copies of the dissertation.

Kind regards,

M.E. Brennan

Figure E.1: IEEE reprint permission letter for [6, 7].

Dear Andre Beckus,

Thank you for contacting The Optical Society.

For the use of material from **[1]** H. E. Kondakci, A. Beckus, A. E. Halawany, N. Mohammadian, G. K. Atia, and A. F. Abouraddy, "Coherence measurements of scattered incoherent light for lensless identification of an object's location and size," Opt. Express, vol. 25, no. 12, pp. 13 087–13 100, Jun. 2017, **[2]** A. El-Halawany, A. Beckus, H. E. Kondakci, M. Monroe, N. Mohammadian, G. K. Atia, and A. F. Abouraddy, "Incoherent lensless imaging via coherency back-propagation," Opt. Lett., vol. 42, no. 16, pp. 3089–3092, Aug. 2017, **[3]** R. R. Naraghi, H. Gemar, M. Batarseh, A. Beckus, G. Atia, S. Sukhov, and A. Dogariu, "Wide-field interferometric measurement of a nonstationary complex coherence function," Opt. Lett., vol. 42, no. 23, 2017, **[4]** A. Beckus, A. Tamasan, A. Dogariu, A. F. Abouraddy, and G. K. Atia, "Spatial coherence of fields from generalized sources in the fresnel regime," J. Opt. Soc. Am. A, vol. 34, no. 12, pp. 2213–2221, Dec. 2017 and **[5]** A. Beckus, A. Tamasan, A. Dogariu, A. F. Abouraddy, and G. K. Atia, "On the inverse problem of source reconstruction from coherence measurements," J. Opt. Soc. Am. A, vol. 35, no. 6, pp. 959–968, 2018:

> Because you are the author of the source paper from which you wish to reproduce material, OSA considers your requested use of its copyrighted materials to be permissible within the author rights granted in the Copyright Transfer Agreement submitted by the requester on acceptance for publication of his/her manuscript. It is requested that a complete citation of the original material be included in any publication. This permission assumes that the material was not reproduced from another source when published in the original publication.

For the use of material from **[6]** H. Gemar, R. R. Naraghi, M. Batarseh, A. Beckus, G. Atia, S. Sukhov, and A. Dogariu, "Efficient measurement of nonstationary complex coherence functions," in Frontiers in Optics, Oct. 2017, p. FTh3D.2, **[7]** A. El-Halawany, A. Beckus, H. E. Kondakci, M. Monroe, N. Mohammadian, G. K. Atia, and A. F. Abouraddy, "Scene reconstruction via two-dimensional complex coherency imaging," in Frontiers in Optics, Sep. 2017, p. FM4C.6, **[8]** H. E. Kondakci, A. Beckus, A. El-Halawany, N. Mohammadian, G. K. Atia, and A. F. Abouraddy, "Lensless object detection and positioning via coherence measurement," in Frontiers in Optics, Sep. 2017, p. FM4C.5, **[9]** A. Beckus, A. Tamasan, Z. Shen, S. Sukhov, A. Dogariu, and G. K. Atia, "Passive non-line-of-sight source classification from coherence measurements," in Imaging and Applied Optics, Jun. 2018, p. CM2E.5, **[10]** A. Beckus, A. Tamasan, A. Dogariu, A. F. Abouraddy, and G. K. Atia, "On scene reconstruction from spatial coherence measurements," in Imaging and Applied Optics, Jun. 2018, p. MTu2D.3 and **[11]** H. E. Kondakci, A. El-Halawany, A. Beckus, N. Mohammadian, G. K. Atia, and A. F. Abouraddy, "Complex-coherence measurements for lensless object positioning," in Imaging and Applied Optics, Jun. 2017, p. CTu1B.5:

> OSA only has copyright for the compilation of the conference proceedings, not the individual papers themselves. As the authors retain copyright to the individual paper, an OSA credit statement is not needed, although we do request a complete citation be included in any publication or adjacent to any posting.

While your publisher should be able to provide additional guidance, OSA prefers the below citation formats:

> For citations in figure captions:
>
> [Reprinted/Adapted] with permission from [ref #] © The Optical Society. (Please include the full citation in your reference list)
>
> For images without captions:
>
> Journal Vol. #, first page (year published) An example: J. Opt. Soc. Am. A 35, 959 (2018)

Please let me know if you have any questions.

Kind Regards,

Rebecca Robinson

Rebecca Robinson
April 16, 2020
Authorized Agent, The Optical Society

The Optical Society (OSA)

Figure E.2: OSA reprint permission letter for [1, 2, 8–16].

LIST OF REFERENCES

[1] R. R. Naraghi, H. Gemar, M. Batarseh, A. Beckus, G. Atia, S. Sukhov, and A. Dogariu, "Wide-field interferometric measurement of a nonstationary complex coherence function," Opt. Lett. **42** (2017).

[2] H. E. Kondakci, A. Beckus, A. E. Halawany, N. Mohammadian, G. K. Atia, and A. F. Abouraddy, "Coherence measurements of scattered incoherent light for lensless identification of an object's location and size," Opt. Express **25**, 13087–13100 (2017).

[3] Z. Shen, S. Sukhov, and A. Dogariu, "Monte Carlo method to model optical coherence propagation in random media," J. Opt. Soc. Am. A **34**, 2189–2193 (2017).

[4] S. Zhang, H. Sheng, D. Yang, J. Zhang, and Z. Xiong, "Micro-lens-based matching for scene recovery in lenslet cameras," IEEE Trans. Image Process. **27**, 1060–1075 (2018).

[5] M. Levoy, R. Ng, A. Adams, M. Footer, and M. Horowitz, "Light field microscopy," ACM Trans. Graph. **25**, 924–934 (2006).

[6] A. Beckus, A. Tamasan, and G. K. Atia, "Multi-modal non-line-of-sight passive imaging," IEEE Trans. Image Process. **28**, 3372–3382 (2019).

[7] A. El-Halawany, A. Beckus, H. E. Kondakci, M. Monroe, N. Mohammadian, G. K. Atia, and A. F. Abouraddy, "Scene reconstruction via coherency imaging," in "2017 IEEE Photonics Conference (IPC)," (2017), pp. 605–606.

[8] A. El-Halawany, A. Beckus, H. E. Kondakci, M. Monroe, N. Mohammadian, G. K. Atia, and A. F. Abouraddy, "Incoherent lensless imaging via coherency back-propagation," Opt. Lett. **42**, 3089–3092 (2017).

[9] A. Beckus, A. Tamasan, A. Dogariu, A. F. Abouraddy, and G. K. Atia, "Spatial coherence of fields from generalized sources in the fresnel regime," J. Opt. Soc. Am. A **34**, 2213–2221 (2017).

[10] A. Beckus, A. Tamasan, A. Dogariu, A. F. Abouraddy, and G. K. Atia, "On the inverse problem of source reconstruction from coherence measurements," J. Opt. Soc. Am. A **35**, 959–968 (2018).

[11] H. Gemar, R. R. Naraghi, M. Batarseh, A. Beckus, G. Atia, S. Sukhov, and A. Dogariu, "Efficient measurement of nonstationary complex coherence functions," in "Frontiers in Optics," (2017), p. FTh3D.2.

[12] A. El-Halawany, A. Beckus, H. E. Kondakci, M. Monroe, N. Mohammadian, G. K. Atia, and A. F. Abouraddy, "Scene reconstruction via two-dimensional complex coherency imaging," in "Frontiers in Optics," (2017), p. FM4C.6.

[13] H. E. Kondakci, A. Beckus, A. El-Halawany, N. Mohammadian, G. K. Atia, and A. F. Abouraddy, "Lensless object detection and positioning via coherence measurement," in "Frontiers in Optics," (2017), p. FM4C.5.

[14] A. Beckus, A. Tamasan, Z. Shen, S. Sukhov, A. Dogariu, and G. K. Atia, "Passive non-line-of-sight source classification from coherence measurements," in "Imaging and Applied Optics," (2018), p. CM2E.5.

[15] A. Beckus, A. Tamasan, A. Dogariu, A. F. Abouraddy, and G. K. Atia, "On scene reconstruction from spatial coherence measurements," in "Imaging and Applied Optics," (2018), p. MTu2D.3.

[16] H. E. Kondakci, A. El-Halawany, A. Beckus, N. Mohammadian, G. K. Atia, and A. F. Abouraddy, "Complex-coherence measurements for lensless object positioning," in "Imaging and Applied Optics," (2017), p. CTu1B.5.

[17] K. M. Yoo, F. Liu, and R. R. Alfano, "Imaging through a scattering wall using absorption," Opt. Lett. **16**, 1068–1070 (1991).

[18] A. K. Singh, D. N. Naik, G. Pedrini, M. Takeda, and W. Osten, "Looking through a diffuser and around an opaque surface: A holographic approach," Opt. Express **22**, 7694–7701 (2014).

[19] O. Katz, P. Heidmann, M. Fink, and S. Gigan, "Non-invasive single-shot imaging through scattering layers and around corners via speckle correlations," Nature Photon. **8**, 784–790 (2014).

[20] E. Edrei and G. Scarcelli, "Optical imaging through dynamic turbid media using the fourier-domain shower-curtain effect," Optica **3**, 71–74 (2016).

[21] A. Velten, T. Willwacher, O. Gupta, A. Veeraraghavan, M. G. Bawendi, and R. Raskar, "Recovering three-dimensional shape around a corner using ultrafast time-of-flight imaging," Nat. Commun. **3** (2012). Art. no. 745.

[22] M. O'Toole, D. B. Lindell, and G. Wetzstein, "Confocal non-line-of-sight imaging based on the light-cone transform," Nature **555**, 338–341 (2018).

[23] A. Bhandari and R. Raskar, "Signal processing for time-of-flight imaging sensors: An introduction to inverse problems in computational 3-d imaging," IEEE Signal Process. Mag. **33**, 45–58 (2016).

[24] M. Buttafava, J. Zeman, A. Tosi, K. Eliceiri, and A. Velten, "Non-line-of-sight imaging using a time-gated single photon avalanche diode," Opt. Express **23**, 20997–21011 (2015).

[25] G. Gariepy, F. Tonolini, R. Henderson, J. Leach, and D. Faccio, "Detection and tracking of moving objects hidden from view," Nature Photonics **10**, 23–26 (2016).

[26] J. Klein, C. Peters, J. Mart´in, M. Laurenzis, and M. B. Hullin, "Tracking objects outside the line of sight using 2d intensity images," Sci. Rep. **6** (2016). Art. no. 32491.

[27] X. Xu, X. Xie, H. He, H. Zhuang, J. Zhou, A. Thendiyammal, and A. P. Mosk, "Imaging objects through scattering layers and around corners by retrieval of the scattered point spread function," Opt. Express **25**, 32829–32840 (2017).

[28] O. Katz, E. Small, and Y. Silberberg, "Looking around corners and through thin turbid layers in real time with scattered incoherent light," Nature Photon. **6**, 549–553 (2012).

[29] A. Torralba and W. T. Freeman, "Accidental pinhole and pinspeck cameras: Revealing the scene outside the picture," in "Proc. IEEE CVPR," (2012), pp. 374–381.

[30] K. L. Bouman, V. Ye, A. B. Yedidia, F. Durand, G. W. Wornell, A. Torralba, and W. T. Freeman, "Turning corners into cameras: Principles and methods," in "Proc. IEEE ICCV," (2017), pp. 2289–2297.

[31] E. Wolf, *Introduction to the Theory of Coherence and Polarization of Light* (Cambridge Univ. Press, Cambridge, U.K., 2007).

[32] E. Baleine and A. Dogariu, "Variable coherence tomography," Opt. Lett. **29**, 1233–1235 (2004).

[33] E. Baleine and A. Dogariu, "Variable-coherence tomography for inverse scattering problems," J. Opt. Soc. Am. A **21**, 1917–1923 (2004).

[34] M. E. Testorf, B. M. Hennelly, and J. Ojeda-Castañeda, *Phase-space optics: Fundamentals and applications* (McGraw-Hill, New York, 2010).

[35] M. Bastiaans, "The wigner distribution function applied to optical signals and systems," Optics Communications **25**, 26 – 30 (1978).

[36] H.-Y. Liu, E. Jonas, L. Tian, J. Zhong, B. Recht, and L. Waller, "3D imaging in volumetric scattering media using phase-space measurements," Opt. Express **23**, 14461–14471 (2015).

[37] B. J. Thompson and E. Wolf, "Two-beam interference with partially coherent light," J. Opt. Soc. Am. **47**, 895–902 (1957).

[38] S. Divitt, Z. J. Lapin, and L. Novotny, "Measuring coherence functions using non-parallel double slits," Opt. Express **22**, 8277–8290 (2014).

[39] S. Divitt and L. Novotny, "Spatial coherence of sunlight and its implications for light management in photovoltaics," Optica **2**, 95–103 (2015).

[40] H. Partanen, J. Turunen, and J. Tervo, "Coherence measurement with digital micromirror device," Opt. Lett. **39**, 1034–1037 (2014).

[41] Y. Mej´ia and A. I. Gonzáles, "Measuring spatial coherence by using a mask with multiple apertures," Opt. Commun. **273**, 428–434 (2007).

[42] A. I. Gonzáles and Y. Mej´ia, "Nonredundant array of apertures to measure the spatial coherence in two dimensions with only one interferogram," J. Opt. Soc. Am. A **28**, 1107–1113 (2011).

[43] C. Iaconis and I. A. Walmsley, "Direct measurement of the two-point correlation function," Opt. Lett. **21**, 1783–1785 (1996).

[44] C.-C. Cheng, M. G. Raymer, and H. Heier, "A variable lateral-shearing Sagnac interferometer with high numerical aperture for measuring the complex spatial coherence function of light," J. Mod. Opt. **47**, 1237–1246 (2000).

[45] M. Santarsiero and R. Borghi, "Measuring spatial coherence by using a reversed-wavefront young interferometer," Opt. Lett. **31**, 861–863 (2006).

[46] B. Stoklasa, L. Motka, J. Rehacek, Z. Hradil, and L. L. Sáchez-Soto, "Wavefront sensing reveals optical coherence," Nat. Commun. **5** (2014). Art. no. 3275.

[47] S. Cho, M. A. Alonso, and T. G. Brown, "Measurement of spatial coherence through diffraction from a transparent mask with a phase discontinuity," Opt. Lett. **37**, 2724 (2012).

[48] J. K. Wood, K. A. Sharma, S. Cho, T. G. Brown, and M. A. Alonso, "Using shadows to measure spatial coherence," Opt. Lett. **39**, 4927–4930 (2014).

[49] K. A. Sharma, T. G. Brown, and M. A. Alonso, "Phase-space approach to lensless measurements of optical field correlations," Opt. Express **24**, 16099–16110 (2016).

[50] J. N. Mait, G. W. Euliss, and R. A. Athale, "Computational imaging," Adv. Opt. Photon. **10**, 409–483 (2018).

[51] M. Batarseh, S. Sukhov, Z. Shen, H. Gemar, R. Rezvani, and A. Dogariu, "Passive sensing around the corner using spatial coherence," Nat. Commun. **9** (2018). Art. no. 3629.

[52] T. S. Huang, ed., *Picture Processing and Digital Filtering* (Springer, Berlin, 1979).

[53] A. K. Jain, *Fundamentals of Digital Image Processing* (Prentice Hall, Englewood Cliffs, 1989).

[54] B. Jähne, *Digital Image Processing: Concepts, Algorithms, and Scientific Applications* (Springer, 1997).

[55] N. George, "Lensless electronic imaging," Opt. Commun. **133**, 22–26 (1997).

[56] J. R. Fienup, "Phase retrieval algorithms: A comparison," Appl. Opt. **21**, 2758–2769 (1982).

[57] R. W. Gerchberg and W. O. Saxton, "A practical algorithm for the determination of phase from image and diffraction plane pictures," Optik **35**, 237–246 (1972).

[58] J. R. Fienup, "Reconstruction of an object from the modulus of its Fourier transform," Opt. Lett. **3**, 27–29 (1978).

[59] H. M. Hayes, J. S. Lim, and A. V. Oppenheim, "Signal reconstruction from phase or magnitude," IEEE Trans. Acoust. Speech Signal Process. **28**, 672–680 (1980).

[60] H. M. Hayes, J. S. Lim, and A. V. Oppenheim, "Iterative procedure for signal reconstruction from Fourier transform phase," Opt. Eng. **21**, 122–127 (1982).

[61] D. Kermisch, "Image reconstruction from phase information only," J. Opt. Soc. Am. **60**, 15–17 (1970).

[62] T. S. Huang, J. W. Burnett, and A. G. Jeczky, "The importance of phase in image processing filters," IEEE Trans. Acoust. Speech Signal Process. **23**, 529–542 (1975).

[63] A. V. Oppenheim and J. S. Lim, "The importance of phase in signals," Proc. IEEE **69**, 529–541 (1981).

[64] Y. Zhang, G. Pedrini, W. Osten, and H. J. Tiziani, "Whole optical wave field reconstruction from double or multi in-line holograms by phase retrieval algorithm," Opt. Express **11**, 3234–3241 (2003).

[65] G. Pedrini, W. Osten, and Y. Zhang, "Wave-front reconstruction from a sequence of interferograms recorded at different planes," Opt. Lett. **30**, 833–835 (2005).

[66] A. F. Abouraddy, O. Shapira, M. Bayindir, J. Arnold, F. Sorin, D. S. Hinczewski, J. D. Joannopoulos, and Y. Fink, "Large-scale optical-field measurements with geometric fibre constructs," Nat. Mater. **5**, 532–536 (2006).

[67] F. Sorin, O. Shapira, A. F. Abouraddy, M. Spencer, N. D. Orf, J. D. Joannopoulos, and Y. Fink, "Exploiting collective effects of multiple optoelectronic devices integrated in a single fiber," Nano Lett. **9**, 2630–2635 (2009).

[68] L. Mandel and E. Wolf, *Optical Coherence and Quantum Optics* (Cambridge University Press, 1995).

[69] J. W. Goodman, *Statistical Optics* (Wiley, 2000).

[70] E. Collett and E. Wolf, "Beams generated by gaussian quasi-homogeneous sources," Optics Communications **32**, 27 – 31 (1980).

[71] A. T. Friberg and R. J. Sudol, "Propagation parameters of gaussian schell-model beams," Optics Communications **41**, 383 – 387 (1982).

[72] F. Gori, "Mode propagation of the field generated by collett-wolf schell-model sources," Optics Communications **46**, 149 – 154 (1983).

[73] M. Salem, T. Shirai, A. Dogariu, and E. Wolf, "Long-distance propagation of partially coherent beams through atmospheric turbulence," Optics Communications **216**, 261 – 265 (2003).

[74] E. Baleine and A. Dogariu, "Propagation of partially coherent beams through particulate media," J. Opt. Soc. Am. A **20**, 2041–2045 (2003).

[75] J. A. Davis and D. M. Cottrell, "Ray matrix analysis of the fast fresnel transform with applications towards liquid crystal displays," Appl. Opt. **51**, 644–650 (2012).

[76] G. Gbur and T. Visser, "Chapter 5 - the structure of partially coherent fields," in "Progress in Optics," , vol. 55 of *Progress in Optics* E. Wolf, ed. (Elsevier, 2010), pp. 285 – 341.

[77] P. Martinsson, H. Lajunen, and A. T. Friberg, "Communication modes with partially coherent fields," J. Opt. Soc. Am. A **24**, 3336–3342 (2007).

[78] T. Shirai, A. Dogariu, and E. Wolf, "Mode analysis of spreading of partially coherent beams propagating through atmospheric turbulence," J. Opt. Soc. Am. A **20**, 1094–1102 (2003).

[79] E. Wolf, "New spectral representation of random sources and of the partially coherent fields that they generate," Optics Communications **38**, 3 – 6 (1981).

[80] F. Gori, M. Santarsiero, and R. Borghi, "Modal expansion for j0-correlated electromagnetic sources," Opt. Lett. **33**, 1857–1859 (2008).

[81] R. Borghi and M. Santarsiero, "Modal decomposition of partially coherent flat-topped beams produced by multimode lasers," Opt. Lett. **23**, 313–315 (1998).

[82] P. Vahimaa and J. Turunen, "Finite-elementary-source model for partially coherent radiation," Opt. Express **14**, 1376–1381 (2006).

[83] L. E. Vicent and M. A. Alonso, "Generalized radiometry as a tool for the propagation of partially coherent fields," Optics Communications **207**, 101 – 112 (2002).

[84] J. C. Petruccelli and M. A. Alonso, "Ray-based propagation of the cross-spectral density," J. Opt. Soc. Am. A **25**, 1395–1405 (2008).

[85] F. W. King, *Hilbert Transforms* (Cambridge University Press, 2009).

[86] C. L. Epstein, *Mathematics of Medical Imaging* (Prentice Hall, 2003).

[87] W. H. Carter and E. Wolf, "Coherence and radiometry with quasihomogeneous planar sources," J. Opt. Soc. Am. **67** (1977).

[88] M. Born and E. Wolf, *Principles of Optics* (Cambridge University Press, 1999), 7th ed.

[89] A. C. Schell, "A technique for the determination of the radiation pattern of a partially coherent aperture," IEEE Trans. Antennas Propag. **15**, 187–188 (1967).

[90] D. L. Marks, R. A. Stack, and D. J. Brady, "Three-dimensional coherence imaging in the Fresnel domain," Appl. Opt. **38**, 1332–1342 (1999).

[91] B. E. Saleh and M. C. Teich, *Fundamentals of Photonics* (Wiley-Interscience, 2007), 2nd ed.

[92] J. Deschamps, D. Courjon, and J. Bulabois, "Gaussian Schell-model sources: an example and some perspectives," J. Opt. Soc. Am. **73**, 256–261 (1983).

[93] Q. He, J. Turunen, and A. T. Friberg, "Propagation and imaging experiments with Gaussian Schell-model beams," Opt. Commun. **15**, 695–705 (1998).

[94] I. J. LaHaie, "Uniqueness of the inverse source problem for quasi-homogeneous, partially coherent sources," J. Opt. Soc. Am. A **3**, 1073–1079 (1986).

[95] G. Gbur, "Uniqueness of the solution to the inverse source problem for quasi-homogeneous sources," Optics Communications **187**, 301 – 309 (2001).

[96] W. H. Garter and E. Wolf, "Inverse problem with quasi-homogeneous sources," J. Opt. Soc. Am. A **2**, 1994–2000 (1985).

[97] A. J. Devaney, "The inverse problem for random sources," Journal of Mathematical Physics **20**, 1687–1691 (1979).

[98] I. J. LaHaie, "Inverse source problem for three-dimensional partially coherent sources and fields," J. Opt. Soc. Am. A **2**, 35–45 (1985).

[99] D. Kohler and L. Mandel, "Source reconstruction from the modulus of the correlation function: a practical approach to the phase problem of optical coherence theory∗," J. Opt. Soc. Am. **63**, 126–134 (1973).

[100] J. R. Fienup, "Reconstruction of a complex-valued object from the modulus of its fourier transform using a support constraint," J. Opt. Soc. Am. A **4**, 118–123 (1987).

[101] J. R. Fienup, "Lensless coherent imaging by phase retrieval with an illumination pattern constraint," Opt. Express **14**, 498–508 (2006).

[102] T. Habashy, A. T. Friberg, and E. Wolf, "Application of the coherent-mode representation to a class of inverse source problems," Inverse Problems **13**, 47 (1997).

[103] M. Liebling, T. Blu, and M. Unser, "Fresnelets: new multiresolution wavelet bases for digital holography," IEEE Transactions on Image Processing **12**, 29–43 (2003).

[104] S. Sukhov, M. Batarseh, R. R. Naraghi, H. Gemar, A. C. Tamasan, and A. Dogariu, "Babinet's principle for mutual intensity," Opt. Lett. **42**, 3980–3983 (2017).

[105] A. Stern, "Why is the linear canonical transform so little known?" AIP Conf. Proc. **860**, 225–234 (2006).

[106] E. K. P. Chong and S. H. Zak, *An Introduction to Optimization* (John Wiley & Sons, 2013), 4th ed.

[107] T. Kohlgraf-Owens and A. Dogariu, "Finding the field transfer matrix of scattering media," Opt. Express **16**, 13225–13232 (2008).

[108] I. M. Vellekoop and A. P. Mosk, "Focusing coherent light through opaque strongly scattering media," Opt. Lett. **32**, 2309–2311 (2007).

[109] S. Popoff, G. Lerosey, M. Fink, A. C. Boccara, and S. Gigan, "Image transmission through an opaque material," Nature Communications **1**, 81 (2010).

[110] H. He, Y. Guan, and J. Zhou, "Image restoration through thin turbid layers by correlation with a known object," Opt. Express **21**, 12539–12545 (2013).

[111] J. Lu and H. Zhou, "Numerical reproduction and explanation of road surface mirages under grazing-angle scattering," Appl. Opt. **56**, 5550–5558 (2017).

[112] R. Pierrat, J.-J. Greffet, R. Carminati, and R. Elaloufi, "Spatial coherence in strongly scattering media," J. Opt. Soc. Am. A **22**, 2329–2337 (2005).

[113] F. E. Nicodemus, "Directional reflectance and emissivity of an opaque surface," Appl. Opt. **4**, 767–775 (1965).

[114] M. Tavassoly, A. Nahal, and Z. Ebadi, "Image formation in rough surfaces," Opt. Commun. **238**, 252 – 260 (2004).

[115] S. Boyd, N. Parikh, E. Chu, B. Peleato, and J. Eckstein, "Distributed optimization and statistical learning via the alternating direction method of multipliers," Found. Trends Mach. Learn. **3**, 1–122 (2011).

[116] F. Sadjadi, "Comparative image fusion analysis," in "Proc. IEEE CVPR," (2005), pp. 8–15.

[117] C. O. Ancuti, C. Ancuti, C. D. Vleeschouwer, and A. C. Bovik, "Single-scale fusion: An effective approach to merging images," IEEE Trans. Image Process. **26**, 65–78 (2017).

[118] A. Kubota, K. Aizawa, and T. Chen, "Reconstructing dense light field from array of multifocus images for novel view synthesis," IEEE Trans. Image Process. **16**, 269–279 (2007).

[119] N. Dwork, E. M. Lasry, J. M. Pauly, and J. Balbás, "Formulation of image fusion as a constrained least squares optimization problem," J. Med. Imag. **4**, 4 – 10 (2017). Art. no. 014003.

[120] M. Batarseh, Z. Shen, R. R. Naraghi, H. E. Gemar, S. Sukhov, and A. Dogariu, "Transformation of complex spatial coherence function in reflection from random media," in "Front. in Opt.", (2017).

[121] Z. Shen, S. Sukhov, and A. Dogariu, "Monte Carlo simulation of coherence propagation through scattering media," in "Front. in Opt.", (2017). Art. no. FM3C.7.

[122] D. S. Taubman, *JPEG2000: image compression fundamentals, standards, and practice* (Kluwer Academic Publishers, 2002).

[123] S. Boyd and L. Vandenberghe, *Convex Optimization* (Cambridge Univ. Press, Cambridge, U.K., 2004).

[124] M. R. Hestenes, "Multiplier and gradient methods," J. Optim. Theory Appl. **4**, 303–320 (1969).

[125] L. Michael, D. David, and P. J. M., "Sparse MRI: The application of compressed sensing for rapid MR imaging," Magn. Reson. Med. **58**, 1182–1195 (2007).

[126] S. Ji, Y. Xue, and L. Carin, "Bayesian compressive sensing," IEEE Trans. Signal Process. **56**, 2346–2356 (2008).

[127] J. Tian, Z. Murez, T. Cui, Z. Zhang, D. Kriegman, and R. Ramamoorthi, "Depth and image restoration from light field in a scattering medium," in "Proc. IEEE ICCV," (2017), pp. 2420–2429.

[128] C. Verleysen, T. Maugey, P. Frossard, and C. D. Vleeschouwer, "Wide-baseline foreground object interpolation using silhouette shape prior," IEEE Trans. Image Process. **26**, 5477–5490 (2017).

[129] A. M. Bruckstein, R. J. Holt, Y. D. Jean, and A. N. Netravali, "On the use of shadows in stance recovery," Int. J. Imaging Syst. Technol. **11**, 315–330 (2000).

[130] Z. Zhang and M. Levoy, "Wigner distributions and how they relate to the light field," in "Proc. ICCP," (2009), pp. 1–10.

[131] M. J. Bastiaans, "Application of the wigner distribution function to partially coherent light," J. Opt. Soc. Am. A **3**, 1227–1238 (1986).

[132] A. Walther, "Radiometry and coherence," J. Opt. Soc. Am. **58**, 1256–1259 (1968).

[133] A. Sinha, J. Lee, S. Li, and G. Barbastathis, "Lensless computational imaging through deep learning," Optica **4**, 1117–1125 (2017).

[134] C. A. Metzler, F. Heide, P. Rangarajan, M. M. Balaji, A. Viswanath, A. Veeraraghavan, and R. G. Baraniuk, "Deep-inverse correlography: towards real-time high-resolution non-line-of-sight imaging," Optica **7**, 63–71 (2020).

[135] S. Wang, Z. Su, L. Ying, X. Peng, S. Zhu, F. Liang, D. Feng, and D. Liang, "Accelerating magnetic resonance imaging via deep learning," in "2016 IEEE 13th International Symposium on Biomedical Imaging (ISBI)," (2016), pp. 514–517.

[136] G. Wang, J. C. Ye, K. Mueller, and J. A. Fessler, "Image reconstruction is a new frontier of machine learning," IEEE Transactions on Medical Imaging **37**, 1289–1296 (2018).

[137] y. yang, J. Sun, H. Li, and Z. Xu, "Deep admm-net for compressive sensing mri," in "Advances in Neural Information Processing Systems 29," D. D. Lee, M. Sugiyama, U. V. Luxburg, I. Guyon, and R. Garnett, eds. (Curran Associates, Inc., 2016), pp. 10–18.

[138] K. Monakhova, J. Yurtsever, G. Kuo, N. Antipa, K. Yanny, and L. Waller, "Unrolled, model-based networks for lensless imaging," NeurIPS 2019 Workshop Deep Inverse (2019).

[139] S. A. H. Hosseini, B. Yaman, S. Moeller, M. Hong, and M. Akçakaya, "Dense Recurrent Neural Networks for Inverse Problems: History-Cognizant Unrolling of Optimization Algorithms," arXiv e-prints arXiv:1912.07197 (2019).

[140] C. Qin, J. Schlemper, J. Caballero, A. N. Price, J. V. Hajnal, and D. Rueckert, "Convolutional recurrent neural networks for dynamic mr image reconstruction," IEEE Transactions on Medical Imaging **38**, 280–290 (2019).

[141] J. Sirignano and K. Spiliopoulos, "Dgm: A deep learning algorithm for solving partial differential equations," Journal of Computational Physics **375**, 1339 – 1364 (2018).

[142] Y. Chen, L. Lu, G. E. Karniadakis, and L. Dal Negro, "Physics-informed neural networks for inverse problems in nano-optics and metamaterials," Optics Express **28**, 11618 (2020).

[143] C. Dong, C. C. Loy, K. He, and X. Tang, "Learning a deep convolutional network for image super-resolution," in "Computer Vision – ECCV 2014," D. Fleet, T. Pajdla, B. Schiele, and T. Tuytelaars, eds. (Springer International Publishing, Cham, 2014), pp. 184–199.

[144] K. Zhang, W. Zuo, Y. Chen, D. Meng, and L. Zhang, "Beyond a gaussian denoiser: Residual learning of deep cnn for image denoising," IEEE Transactions on Image Processing **26**, 3142–3155 (2017).